Basics of process physics and joint formation in resistance projection welding processes

Von der Fakultät Chemie der Universität Stuttgart
zur Erlangung der Würde eines Doktors der
Naturwissenschaft (Dr. rer. nat.) genehmigte Abhandlung

Vorgelegt von
Michael Wehle (M.Sc.)
aus Sindelfingen

Hauptberichter:	Prof. Dr. Dr. h.c. Guido Schmitz (IMW)
Mitberichter:	Prof. Dr.– Ing. Martin Greitmann (Hochschule Esslingen)
2. Mitberichter:	Prof. Dr. rer. nat. Siegfried Schmauder (IMWF)
Prüfungsvorsitzender:	Prof. Dr. rer. nat. Thomas Schleid (IAC)

Tag der mündlichen Prüfung: 27.05.2020

Institut für Materialwissenschaft der Universität Stuttgart
2020

Erklärung über die Eigenständigkeit der Dissertation

Ich versichere, dass ich die vorliegende Arbeit mit dem Titel
“*Basics of process physics and joint formation* in resistance projection welding processes”
Selbstständig verfasst und keine anderen als die angegebenen Quellen und Hilfsmittel benutzt habe. Aus fremden Quellen entnommene Passagen und Gedanken sind als solche kenntlich gemacht.

Declaration of authorship

I hereby certify that the dissertation entitled
“*Basics of process physics and joint formation* in resistance projection welding processes”
is entirely my own work except where otherwise indicated. Passages and ideas from other sources have been clearly indicated.

_____

Michael Wehle, Stuttgart, 27.05.2020

To my mother Sabine,
in remembrance of my father Herbert,
to my wife Julia and my son Felix

Acknowledgement

First, I would like to gratefully thank my academic supervisor Prof. Dr. Dr. h. c. Guido Schmitz for his support and his guidance. I was always welcome at the chair for materials physics and enjoyed the pleasant cooperation. Special thanks also goes to Prof. Dr.- Ing. Martin Greitmann for the deep interest in my work, the many technical discussions and not last being the second reviewer of this thesis. I would also like to thank Prof. Dr. rer. nat. Dr. h. c. Siegfried Schmauder for the support in numerical questions and his interest in my work.

My deepest gratitude is directed to Dr. rer. nat. Florian Schmid, as my mentor, for the uncountable discussions on the topic and methodology as well for all the critical questions and the mental support that has substantially contributed to the success of this work. My thankfulness also goes to Dr.- Ing. Friedhelm Günter for the opportunity to join the doctoral programme of the Robert Bosch GmbH and the support of my personal development, as well as professional and methodological discussions.

I would like to thank Dipl.- Ing. Christoph Lehmeier and Dipl.- Ing. Frank Moszner for the fruitful discussions on the example process and the backing with the welding trials as well as the insight into relevant applications of projection welding and numerical simulation. Special thanks also go to my colleagues Helmut Mannal, Helmut Braun, Dipl.- Ing. Paul Hund and Franz Wetzl for the technical support, the many expert advices and the solace in times when things went worse than expected.

Special appreciation goes to Dr.- Ing Tim Pychynski for the backing in the process simulation, the many discussions on that topic as well as the proof reading of this thesis. For the support in numerical simulation issues I further would like to thank Dr.- Ing. Udo Hartel, Dominic Woitun (M.Sc.) and Fu Xing Long (B.Sc.). I am grateful to Tobias Menold (M.Sc.) for discussions on physical effects in the field of electro-magnetism and structural mechanics.

I would also like to thank the al the PhD students of the Bosch doctoral program who accompanied me on my way. In particular, I would like to thank Michael Schänzel (M.Sc.), Dipl.- Ing. Damir Shakirov and Dr. rer. nat. Mathias Widmaier for their expertise and mental support.

Further, I would like to thank my internship students Tiago Queiroga Gazaniga de Assis (B.Sc.), Alexander Schif (M.Sc.) and Julian Hasselmann (B.Sc.) for their help in planning, designing, conducting and evaluating the experiments and numerical simulations. Thanks also go to Dr. rer. nat. Lars Epple for the help and advice in sample analytics and Steffen Eberhardt for mechanical testing of the samples.
For the final independent proof reading of this work, I would also like to thank Dr. rer. nat. Markus Westerhausen.
I would like to thank all my colleagues at the Robert Bosch GmbH in Renningen as well as all the employees of the chair for materials physics at the University of Stuttgart for the support in technical and organizational issues and the pleasant time.

On a final note I would like to gratefully thank my parents, my family and my friends for the mental support and my wife Julia for her unconditional backing all the time.

Zusammenfassung

Diese Arbeit leistet einen Beitrag zur Verbesserung des Prozessverständnisses von Widerstands-Buckelschweißverfahren. Es werden die bekannten grundlegenden physikalischen Prozessgrößen von Widerstandsschweißprozessen auf diese Verfahren übertragen und deren Relevanz für den Prozess mittels analytischer und numerischer Methoden an Hand eines Prozessbeispiels abgeschätzt.

Die Arbeit liefert somit ein physikalisches Prozessmodell, welches zum einen das Prozessverständnis vertieft zum anderen auch eine Grundlage für die Verbesserung der numerischen Finite Elemente Simulation bildet.

Einen weiteren Fortschritt bringt die vorgelegte Arbeit durch die Untersuchungen zur Verbindungsbildung von Metallen (in diesem Fall rostfreie Stähle) im semi- festen Zustand mit sich. Durch die systematische Untersuchung der Einflussgrößen Temperatur, Druck und Scherung in der Grenzfläche zwischen zwei Probekörpern wird ein Kriterium erarbeitet, welches eine Abschätzung des Schweißergebnisses ermöglicht. Somit wird einerseits ein vertieftes allgemeines Verständnis des Festkörperschweißens sowie ein spezifisch für das Buckelschweißen gültige Verständnis aufgebaut.

Eine Kombination des Verbindungsbildungskriteriums mit einem numerischen Modell zur Simulation des Gesamtprozesses ermöglicht eine Vorbewertung von Fügeaufgaben. Hierzu werden erste Ansätze präsentiert, um die Anwendbarkeit der Vorarbeiten in der numerischen Simulation aufzuzeigen.

Durch die Ergebnisse dieser Arbeit wird somit eine Reduktion des experimentellen Aufwandes bei der Prozessentwicklung des untersuchten Verfahrens erreicht und die Vorbewertung künftiger Fügeaufgaben erleichtert. Des Weiteren lassen sich, durch die Gestaltung der durchgeführten Versuche, allgemeingültige Schlüsse ziehen, welche auch für artverwandte Widerstandsschweißverfahren einen Mehrwert darstellen.

Abstract

This work contributes to an enhancement of the physical process understanding of resistance welding- and projection welding processes. The known basic physical process variables of resistance welding processes are transferred to these techniques and their relevance for the process is estimated by means of analytical and numerical methods, using a process example.
In this work a physical process model is derived, which on the one hand deepens the process understanding and on the other hand also forms a basis for the improvement of the numerical process simulation of projection welding processes.

This work progress the understanding of the joint formation between metals (stainless steel in the examined case) in solid state welding. Through systematic examination of the influence of temperature, contact pressure and interfacial shearing on the joint formation, a criterion for solid state welding is derived. These results contribute to the deeper understanding of general solid state welding and furthermore the understanding of projection welding processes.

An implementation of the derived physical process model into commercially available finite element software and the application of the derived joint formation criterion enables a pre-assessment of the welding results. First attempts are presented for showing the applicability and potentials of this approach.

The results of this work thus reduce the experimental effort involved in the process development of projection welding processes and facilitate the pre-evaluation of future joining tasks. Furthermore, through the experimental design, generally valid conclusions can be drawn which are also applicable to related resistance welding processes.

Table of content

Index of abbreviations

Symbols

a	Constriction radius in mm
$A(r)$	Cross section area in mm² as a function of the radius r
A_{app}	Apparent contact area in mm²
A_{cont}	Contact area in mm²
$A_{cont,a}$	Angular contact area in mm²
A_{real}	Real contact area in mm²
B	Magnetic flux density in T
B_{peak}	Peak magnetic flux density in T
C	Capacitance in mF
c_p	Specific heat in $J \cdot kg^{-1} \cdot K^{-1}$
D	Diffusion coefficient in $cm^2 \cdot s^{-1}$
d_{weld}	Welding depth in mm
e_{diss}	Dissipated plastic energy per unit volume in $J \cdot mm^{-3}$
E_{diss}	Dissipated plastic energy in J
$E_{diss,tot}$	Total dissipated plastic energy in J
E_{fric}	Frictional energy in J
E_{Joule}	Energy due to Joule Heating in J
E_{mag}	Magnetic energy in J
ε_m	Thermal emissivity coefficient
f	Frequency in Hz
F_a	Angular force in kN
$F(\lambda)$	Dimensionless geometrical resistance form factor
F_m	Magnetic attraction force in N
F_{mag}	Magnetic virtual force in N
F_N	Normal force in kN
H	Materials hardness in HV
H_{mag}	Magnetic field strength in $A \cdot m^{-1}$
I	Electrical current in A
j_{cont}	Local electrical contact current density in $A \cdot mm^{-2}$
J	Electric current density in $A \cdot m^{-2}$
k_{SB}	Stefan-Boltzmann constant $W \cdot m^{-2} \cdot K^{-4}$
L	Lorenz Number in $W \cdot \Omega \cdot K^{-2}$
l	Sample length in mm

λ	Radius ratio for geometrical resistance form factor
λ_{th}	Thermal conductivity in $W \cdot m^{-1} \cdot K^{-1}$
λ_{temp}	Temperature conductivity in $m^2\ s^{-1}$
μ	Magnetic permeability in $H \cdot m^{-1}$
$p_{c,a}$	Angular contact pressure in MPa
p_{cont}	Local contact pressure in MPa
P_{conv}	Power transferred by convection in W
P_{el}	Electrical energy in J
P_{rad}	Thermal heat transfer power in W
p_{nom}	Nominal contact pressure in MPa
R_c	Electrical constriction resistance in Ω
$R_{c,ring}$	Electrical constriction resistance of a ring shaped constriction in Ω
$R_{cont,el}$	Electrical contact resistance in Ω
$R_{heat,\alpha}$	Thermal contact resistance via α- spots in
$R_{heat,gap}$	Thermal resistance of the gap medium
$R_{heat,rad}$	Thermal radiation resistance
$R_{heat,total}$	Total thermal contact resistance of the interface in $m \cdot K \cdot W^{-1}$
r_i	Inner radius of an angular constriction in mm
R_{mat}	Electrical materials resistance in Ω
r_o	Outer radius of an angular constriction in mm
R_q	Root mean square roughness in µm
R_z	Maximum height of roughness in µm
$\rho_{cont,el}$	Specific electrical contact resistance in $\Omega \cdot mm^2$
$\rho_{cont}(x)$	Local specific electrical contact resistance in $\Omega \cdot mm^2$
ρ_{el}	Specific electrical resistivity in $\Omega \cdot mm^2 \cdot m^{-1}$
ρ_{mat}	Specific materials resistivity in $\Omega \cdot mm^2 \cdot m^{-1}$
ρ_{FZ}	Electrical resistivity of the fusion zone in $\Omega \cdot mm^2 \cdot m^{-1}$
p_{nom}	Nominal pressure in MPa
ρ_{vol}	Volumetric mass density in $kg \cdot m^3$
ρ^*	Effective specific materials resistivity of two materials in $\Omega \cdot mm^2 \cdot m^{-1}$
σ_{el}	Electrical conductivity $S \cdot mm^{-1}$
σ	Mechanical stress in MPa
σ_y	Yield strength at 0.2% Plastic Yield in MPa
σ_t	Ultimate tensile strength in MPa
t	Time in s
τ	Time shift of temperature conductance in s
T	Temperature in K or °C

T_{amb}	Ambient temperature in K or °C
T_{curie}	Curie-Temperature in K or °C
T_m	Melting temperature in °C
T_{surf}	Surface temperature in °C
U	Electric potential in V
χ	Heat transfer coefficient in $W \cdot m^{-2} \cdot K^{-1}$
W_c	Welding energy in J
w_{diff}	Diffusion width in µm
W_{loss}	Eddy current energy loss per unit volume in $J \cdot mm^{-3}$
W_q	Root mean square height of waviness in µm
W_z	Maximum height of waviness in µm

Acronyms

CPRESS	Contact pressure output of the FEM Simulation
DW	Diffusion Welding
DB	Diffusion Bonding
ECD	Electric current density output of the FEM simulation
EDX	Energy Dispersive X-Ray Spectroscopy
EP	Example process discussed in this work
FEM	Finite Element Method
FW	Friction Welding
FSW	Friction Stir Welding
FZ	Fusion zone
HAZ	Heat-affected zone
HR	Hot Rolling
LM	Light Microscope
NT11	Nodal Temperature output of the FEM simulation
PW	Projection Welding
RW	Resistance Welding
RSW	Resistance Spot Welding
SEM	Scanning Electron Microscope
SSW	Solid State Welding
TC	Thermocouple

1. Introduction

This chapter describes the motivation for a deeper understanding of resitance projection welding processes as well as the derived objectives, which this work focusses on. The chapter ends with an overview over this work's structure.

1.1 Motivation and objectives

Resistance welding is a joining technique that is widely used in industry in the fields of electronic interconnections, automotive manufacturing, ship building or civil engineering [1, 2]. It is an energy efficient process that enables a low cycle time and feasibility of automation. Due to these advantages, resistance welding processes have been continuously developed further over the last 30 years. This work focusses on resistance projection welding. Exemplarily a process with cut projection and a capacitor as energy source is used to discuss the physics and the joint formation of projection welding.

In capacitor discharge, welding electrical energy is provided by a capacitor bank. The discharge of those capacitors generates a short time current pulse of 10 to 30 ms pulse length. Due to the short time scale, the heat at the interface between the work pieces is generated faster than it dissipates into the surrounding material. Thus, in capacitor discharge welding only a small heat-affected zone develops in the vicinity of the fusion zone.

In general, projection welding features low sensitivity to work piece tolerances, surface impurities and also the surface quality of the work pieces. These positive features arise from the high contact forces in the process that lead to a self-adjustment of the geometries. In addition, these forces flatten roughness asperities, which reduces the requirements with respect to the surface quality of the work pieces. Further, projection welding can be accounted to the solid state welding processes through which a strong and media tight metallurgical joint is formed.

Process physics for resistance welding was studied intensively in the past for various applications. The results of these studies satisfy the demand of each special task but are not valid for a general description of the joining mechanisms. Further, the joint formation is not completely understood yet. Unfortunately this knowledge is the key for deeper process understanding and the early prediction of the welding result e.g. on analytical basis or via finite element process simulation. Since thermal, electrical and mechanical processes are coupled or superimposed upon each other in resistance welding, the process understanding on a physical level is quite complex. The identification of the governing physical quantities is therefore challenging. Furthermore, the simultaneous interaction between the individual physical effects also complicates the description of the joint formation.

The objective of this work is a fundamental understanding of the dominant physical aspects in projection welding. The metallurgy is examined on basis of experimental work and the results are discussed in context of solid state welding theory. The outcome of both, process physics and joint formation, serves as the basis for future numerical process simulation.

1.2 Structure of this thesis

After the introduction, an overview of the state of the art is given in chapter 2. Besides an introduction to resistance welding from a technological point of view, the chapter concludes the current understanding of joint formation in these processes. Further, the advances in numerical process simulation and the critical issues of this field of research are presented.
Due to their different focal points, not all aspects can be discussed in detail in the first overview. Therefore, each chapter, the physical process understanding (chapter 3), the joint formation (chapter 4) and the numerical process simulation (chapter 6) is further subdivided. A detailed information on the respective background is given to enhance the general information in chapter 2. In addition, an overview of the degree of novelty of this work is given at the end of each theoretical part. In the application

part, the experimental approaches are described and the outcome is concluded in a short summary of each chapter. A final conclusion of all chapters can be found at the end of this work.

In the process physics chapter the general physical quantities involved in a resistance welding process are introduced, estimated and judged in terms of their relevance for the process example used in this work (see ch. 3). This chapter is structured after mechanical effects (ch. 3.1), thermo-electrical effects (ch. 3.2) and electro-magnetic effects which are fundamentally influencing the physics of the whole process. Special attention is paid to a general description of electrical contact resistance, which is known as an important influencing parameter for resistance welding. Since there is no process independent data available for this quantity, an experimental setup was designed to fix this issue. The results are presented and discussed in context of common contact resistance theory and earlier literature in chapter 3.2. Based on the knowledge of these chapters a physical model for numerical process simulation is derived (see ch. 3.4).

A hypothesis for joint formation is presented in chapter 4 based on the current understanding of solid state welding processes and the synergies with resistance welding (see ch. 4.1). A series of experiments reveals the solid-state joint formation tendency of two stainless steels considered in this work. The chapter concludes with a discussion of the experimental findings.

In chapter 5 an explanatory approach for the observations of chapter 4 is presented, as well as a general criterion for the joint formation. Finally, the fundamentally derived criterion is transferred to the considered example process.

To show the potential of deeper understanding of the process and joint formation the outcome of chapter 3, 4 and 5 is applied to the numerical simulation of the process (see ch. 6). Here a sensitivity study of the measured results of chapter 3 and a basic concept validation of the joint formation hypothesis presented in chapter 4 is performed.

2. State of the art

The following chapter presents an overview of state of the art resistance welding techniques in context of projection welding and introduces the example process, which is used for all discussions (see ch 2.1). Joint formation in resistance welding is addressed in chapter 2.2. Process features regarding joint formation are discussed in context of previous work on resistance- and solid-state welding metallurgy. The chapter concludes with an insight in numerical process simulation of resistance welding processes (see ch. 2.3) within the last three decades.

2.1 Resistance welding techniques

The resistance welding (RW) process is based on the use of electrical energy which is converted into thermal energy by *Joule Heating* [3] at the interface of the parts to be joined. A classification of resistive welding processes follows the type of geometry of the weld (see fig 2-1) [4]. For instance, the RW process used for car body manufacturing generates spots as weld geometry and is therefore classified as resistance spot welding. Especially rotational symmetric work pieces such as bolts and connects of gear parts are welded using projection welding [5]. Further, for connections between massive work pieces and sheet metals or sheet metals with each other projection welding can be utilized, too [6, 7].

There are different types of energy sources available for the processes shown in figure 2-1 such as inverters or capacitors. This work uses an example for a projection welding process, which utilizes capacitors as an energy source.

According to the classification shown below, the example process (further abbreviated as “EP”) can be accounted to the indirect projection welding techniques.

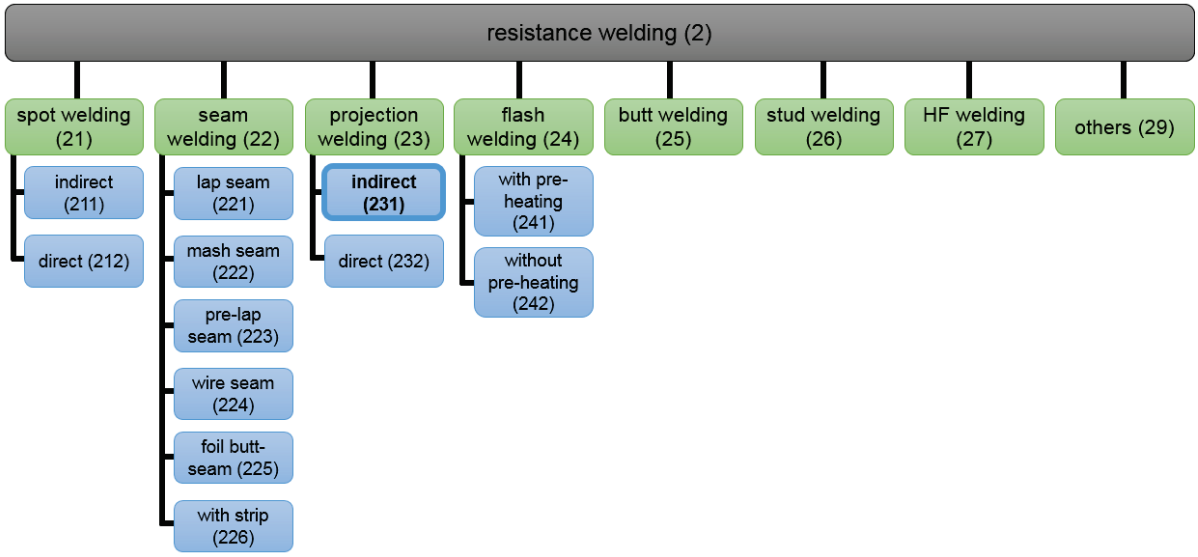

Figure 2-1: Classification of resistance welding processes with reference numbers according to DIN EN ISO 4063 [4]. The example process can be accounted to indirect projection welding.

Figure 2-2 a shows the basic principle of projection welding using the example of stamped sheet metals. A modification is the annular projection (see fig. 2-2 b). Here welding with capacitors is preferably used to achieve a fast and local energy input at the fusion zone which ensures a homogeneous sound weld [8].

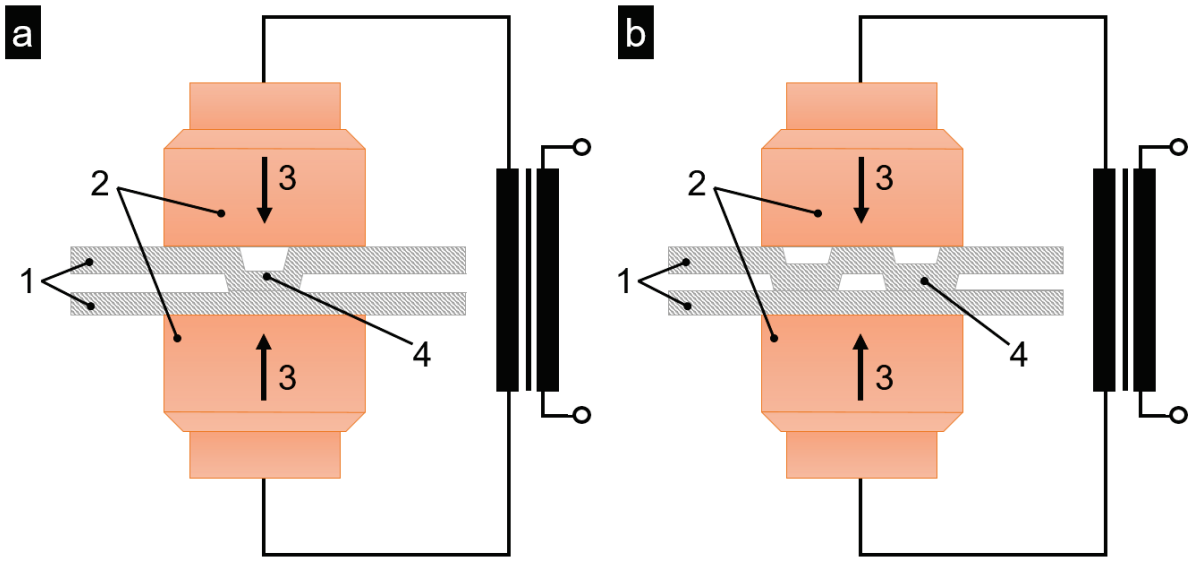

Figure 2-2: Illustration of the basic principle of projection welding for the example of stamped sheet metals (a) according to DVS 2905 [6] and modification of the process using an annular projection (b) according to DVS 2950 [8] with work pieces (1), electrodes (2), electrode forces (3) and projection (4).

In addition, the local energy input has the advantage that the surrounding material's microstructure remains unchanged and no melting occurs. The heat- and deformation affected zone is therefore small. Besides the annular projection welding of sheet metals the process can also be applied to solid rotational symmetric parts which enables sealing of a cavity in between the work pieces e.g. sealing of housings [8]. The annular projection fulfils two tasks. First, it generates the constriction for the electrical current and second it provides the necessary connection area to weld one work piece onto the other one. In the used example, considerable relative movement at the interface appears during joining. Further, the final overlap of the work pieces (described as welding depth d_w) is much larger than for sheet metals projection welding. For this application, the energy is provided by a capacitor bank. A mechanical press (c- frame or portal) provides the welding force. Figure 2-3 shows the principle setup of a welding device. After the capacitor bank has been charged, the welding force is applied (see fig. 2-3, b 1) causing high contact pressures between the joining partners due to an outsize overlap in the contact area. When the specified force level is reached, the discharge is initiated releasing the whole energy stored in the capacitor bank (see fig. 2-3, b 2).

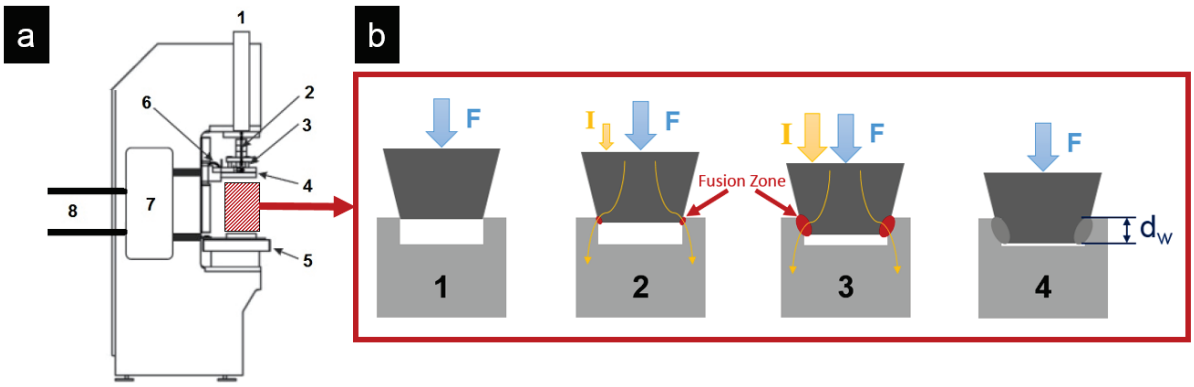

Figure 2-3: Principle sketch of a c-frame welding device for the example process (a) consisting of mechanical press (1), distance sensor (2), follow-up unit (3), upper electrode pick up (4), lower electrode pick up (5), conductor line (6), transformer (7), electrical wiring to capacitor bank (8) and space for work pieces (red). Process scheme of the example process performed within the welding device (b). 1: Pre-pressing, 2: capacitor discharge and heating of the fusion zone (red), 3: sink in under constant mechanical load, 4: cooling and joint formation. Figure a is taken from [5].

The resulting current pulse, which passes the fusion zone, is mainly influenced by the characteristics of the welding device (e.g. transformer ratio or resistances of the welding tool and wiring). The *Joule Heating* caused by the electrical current leads to softening of the material and deformation of the contact zone. The welding depth d_w is increasing with process time (see fig. 2-3, b 3) which is associated by a force drop due to inertia of the mechanical press.

When the electrical energy is consumed, the process stops due to cooling of the fusion zone (see fig. 2-3, b 4). As the illustration shows, the main influencing parameters of the process are the welding force and current. The latter one is a function of the energy, which can be varied by the charging voltage. A schematic process curve for current, force and distance is given in figure 2-4.

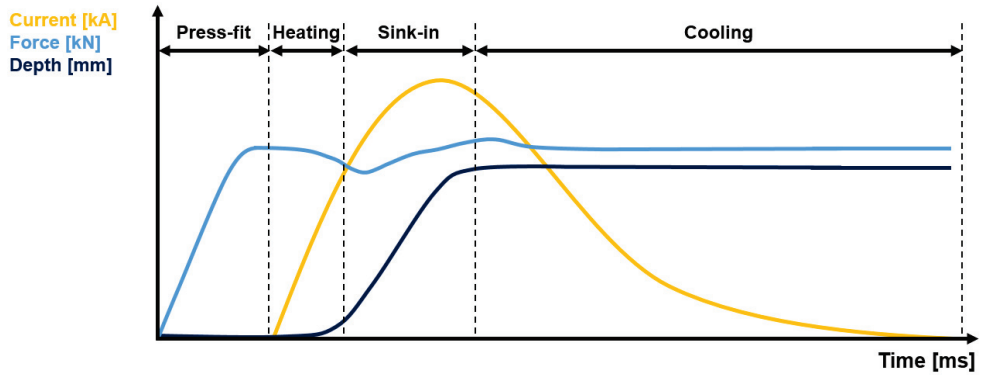

Figure 2-4: Schematic sketch of current, force and distance as a function of welding time for the example process and the corresponding steps of the welding cycle.

The applications of capacitor powered projection welding reaches from micro welding of wires [9–12] to welding of gear and drive train parts which are subjected to high mechanical loads [5]. Especially the considered example process can be used for the latter applications where strong joints are required.

The governing process parameters were examined and optimized in the past on basis of empirical data. Nevertheless, there is still a lack of a basic physical process understanding and no publications exist on this topic up to now. To enhance this understanding the physical process is investigated in detail as part of this work.

2.2 Joint formation in resistance welding processes

Joint formation in resistance welding has intensively been studied for different metals like aluminium [13], copper [14], stainless steels [2, 11, 12, 14, 15] or dissimilar materials combinations [9]. The focus of these publications was mainly on the prediction of weld nugget development in spot welding or the identification of (intermetallic) phase formation during the process [12, 15]. Additionally, the mentioned work of *Khan et al.* [14] includes discussions on the joint strength with respect to life time evaluation of the joints.

Nevertheless, projection welding, as a RW process where no melting of the work piece interfaces occurs, cannot directly be compared to the studies mentioned above. Up to now there are only a few studies on joint formation in welding processes where capacitors are used as energy sources. They mainly document the influence of device parameter on the welding result (e.g. force, current or welding time [16–18] or the used projection geometry [19]).

Further, the weldability of different materials combinations using projection welding was examined (e.g. copper on brass by *Tušek et al.* [20]). A criterion for the estimation of weldability of contact materials based on fusion temperature and electrical conductivity as well as thermal conductivity was reported already in 1982 by *Tslaf* [21]. Still, there is no literature on the basic physical mechanisms affecting joint formation in projection welding processes.

The characteristics of the process suggests a comparison with solid-state welding (SSW) processes, which are understood better. The basic mechanisms of SSW were already discussed at the beginning of the 20th century. In general a joint formation is achieved under high pressure at temperatures between 33% [22] and around 86 % (e.g. in friction stir welding or diffusion press welding) of the material's melting temperature T_m but in absence of a liquid phase [1, 23–25]. An interfacial shearing promotes the cleaning of the interface from oxides and impurities. Furthermore, a deformation of the material in vicinity of the surface supports a close atom to atom contact and the rearrangement of the interface [26–29]. Projection welding features

- High pressure near flow stress of the used materials
- High temperatures in absence of melting
- Relative movement of the interfaces
- Short time current pulse

and thus combines some characteristics of SSW processes. Nevertheless, it is not clear which conditions need to be fulfilled in this exemplary case. As part of this work this issue is investigated in detail to derive a criterion for joint formation in projection welding with respect to physical quantities (e.g. temperature or pressure). Chapter 4 presents the theoretical background for a hypothesis, the experimental approach and the results on this issue.

2.3 Numerical process simulation of resistance welding processes

Numerical simulation of resistance welding has been intensively studied since the 1970's. *Mackerle* [30, 31] concluded the literature on this topic in a bibliography. The algorithms and methods developed for different platforms were steadily improved. A general method for numerical simulation of resistance welding processes was designed by *Zhang* [32, 33]. Further, process dependent simulation models are also available e.g. for resistance projection welding [34–37], resistance spot welding [38–44] or Hot Staking [45]. Parameter studies on the influence of the projection geometry [37, 46–49], electrical contact resistance [45, 50, 51], specific applications [52] or specific materials [36, 39–41, 53–55] are also reported. Since the contact between the work pieces is a key issue in process understanding and numerical simulation, it has also been studied by various researchers [56–60]. Since it is not possible to judge the welding result based on only the physically description of the process the incorporation of metallurgical effects was also studied [59, 61].

As shown in [30–61] the numerical process simulation of resistance welding is a challenging task due to the following aspects:

- The strong thermal, electrical and mechanical interactions present in the process demand for a model that can simultaneously calculate each field variable and, hence, the interactions between each field

- Severe plastic deformation within the contact zone of the work pieces that lead to element- and mesh distortion and finally convergence issues
- Large gradients in temperature, electrical current and mechanical forces within a short time scale which can significantly enlarge the simulation time
- The implementation of a metallurgical model to judge the welding result with respect to the joint formation in the process

The issues also hold for the projection welding process. Since the plastic deformation is much larger than in common resistance welding, especially the massive mesh distortion needs to be handled by the simulation algorithm. The latest publication on the simulation of welding with capacitor as energy source by *Cavaliere et al.* [62]shows the potential of the numerical simulation for capacitor discharge butt welds. They successfully modelled the butt welding of AISI 304 steel via thermo-electrical-mechanical simulation in *ANSYS* [62] enabling a possible repair technique for turbine blades.

Commercially available software cannot handle large plastic deformation in fully coupled thermo-electrical-mechanical models since there is no remeshing method available. Recently *Long* [63] developed a numerical coupling method, for a thermo-electrical-mechanical FEM simulation for the process that is used as an example and further developed in this work. The simulation uses sequentially coupled thermal-electrical and thermo-mechanical models. Remeshing is performed between the sequences and ensures good mesh quality. After remeshing, a mesh-to-mesh solution mapping is used for the transfer of stresses, strains and temperature between the two models. The concept of *Long* is based on a generic self-defined materials data. A plausibility check was performed via metallographic cross sections gained in the extend of this doctoral thesis (see chapter 4).

As a part of this work, the method of *Long* is refined by implementation of the physical process model of chapter 3. The FEM simulation is used to proof the validity of the achieved physical process understanding. Further, the numerical results are used for a first attempt to judge the joint formation based on the criterion presented in chapter 4. A description of the numerical simulation model and its results are presented in chapter 6.

3. Process physics

The interacting physical fields that occur in the example process are subdivided in mechanical effects (ch. 3.1), thermal- electrical effects (ch. 3.2) and electro- magnetic effects (ch. 3.3). Since the local heat generation via *Joule Heating* is the key to resistance welding, special focus lies on the resistances on work piece level. The role of the electrical contact resistance in projection welding is yet unclear and is thus examined in an experimental series, which is described in chapter 3.2.3. An overview of all considered physical effects and their relevance for the process is given in the conclusion (ch. 3.4).

Figure 3-1 shows a process scheme of the example process and the fields that are involved in each process step. It is well known that in RW the local physical quantities at the work piece interface predetermine the evolution of the process. They define the heating behaviour, the deformation of the materials contact zone and finally the formation of the joint.

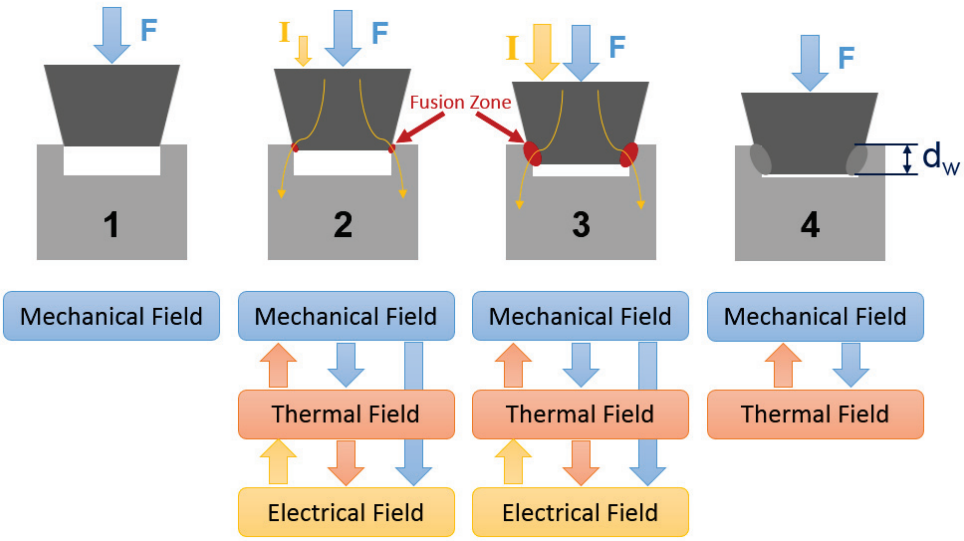

Figure 3-1: Process scheme to visualize the interaction of relevant field variables involved in projection welding depending on each process step. Note that the figure shows a cross section cut of two cylindrical parts.

The physical processes that influence these local quantities in the fusion zone need to be identified. Obviously, temperatures, stresses and plastic deformations in the vicinity of the work piece interface predefine the process and hence the final welding result [64]. Further physical processes that influence the temperature are cooling by the thermal conductivity of the materials in contact or by radiation [64]. Heating can be caused by the *Joule Effect* or electro-magnetic *Eddy Currents* [5]. Further, the heating of the fusion zone is affected by contact properties such as thermal- and electrical contact resistances. The contact pressure and interfacial stresses can be influenced by the welding force or the electro-magnetic *Lorentz Forces* arising from strong magnetic fields that are caused by the electrical current pulse [5]. The same holds for the plastic deformation of the fusion zone.

3.1 Mechanical effects

The forces present in the fusion zone in the cold pre-pressed state are significant for the initial state of contact and later evolution of the process. Especially the heating of the fusion zone is linked to the initial contact area (macroscopic electrical constriction resistance) and the contact pressure (electrical contact resistance). Further, the final deformation and stress distribution inside the fusion zone is directly linked to the applied force. For estimation of the contact pressure and the initial contact area after the cold pre-pressing, a numerical FEM simulation was performed using the commercially available software *ABAQUS*. For this, a thermo-mechanical model was built up using a typical welding geometry (see fig 3-2). For the contact situation a frictional contact with friction coefficient $\mu_r = 0.15$ was assumed. The two parts were loaded up to a force of 18 kN within one second. Then the force was kept constant. This value represents the typical welding force range for small geometries. The temperature dependent materials data of the stainless steels used in the model were calculated using the software JMatPro and adjusted based on experimental data. For details, see appendix (app. A).

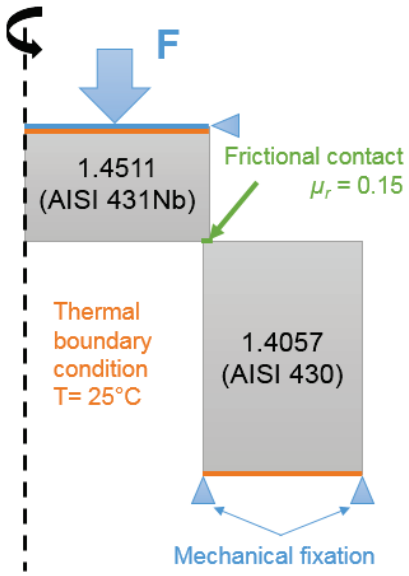

Figure 3-2: Schematic sketch of the rotational symmetric model used for the mechanical simulation of the pre-pressing process. The top parts material was assumed as 1.4511 (AISI 431 Nb) stainless steel and the bottom part 1.4057 (AISI 430) stainless steel. The force *F* was applied as surface load. Environment temperature was set to 25 °C. Details of the contact region are depicted in figure 3-3 a. A validation of the model is described in chapter 6.

To handle the large plastic deformations at the interface of the parts, a re-meshing method, presented by *Long*, was used [63]. This method reduces element distortion by subsequent re-meshing at pre-defined small time steps of miliseconds to a few hundred microseconds. For small increments in simulation time, the displacements are small and thus, deformation of the interface is kept low. After each cycle (predefined number of time increments that is adapted to the expected distortion of elements) the deformed mesh is transformed into a new part and then re-meshed to reduce element distortion. The stresses, strains and temperatures are mapped upon the new geometry and the model is being restarted for further calculation until the simulation is finished. For a detailed description of the method see the original publication of *Long* [63].

Figure 3-3 shows the initial state (a) and the resulting deformed state (b) as well as the contact pressure distribution established between the contacting parts. The contact pressure reaches values between 950 MPa and 1093 MPa (see fig 3-3 b) when a typical welding force of e.g. 18 kN is applied. A contact area of 24.39 mm² results after the loading. Hence, in vicinity of the contact surface severe plastic deformation occurs under the mechanical load. These results serve as basis for the discussion of pressure dependent electrical- and thermal contact resistances presented later (see chapter 3.3). They also show that the contact pressures to be expected in projection welding exceed the yield strength σ_y of the involved materials (AISI 430: σ_y = 719 MPa, AISI

431 Nb: σ_y = 517 MPa), which is a unique feature of the process. A contact pressure of this order of magnitude would result in severe plastic deformation of the work pieces (e.g. in projection welding), already in the cold state. Hence, these values are only possible due to the press-fitting.

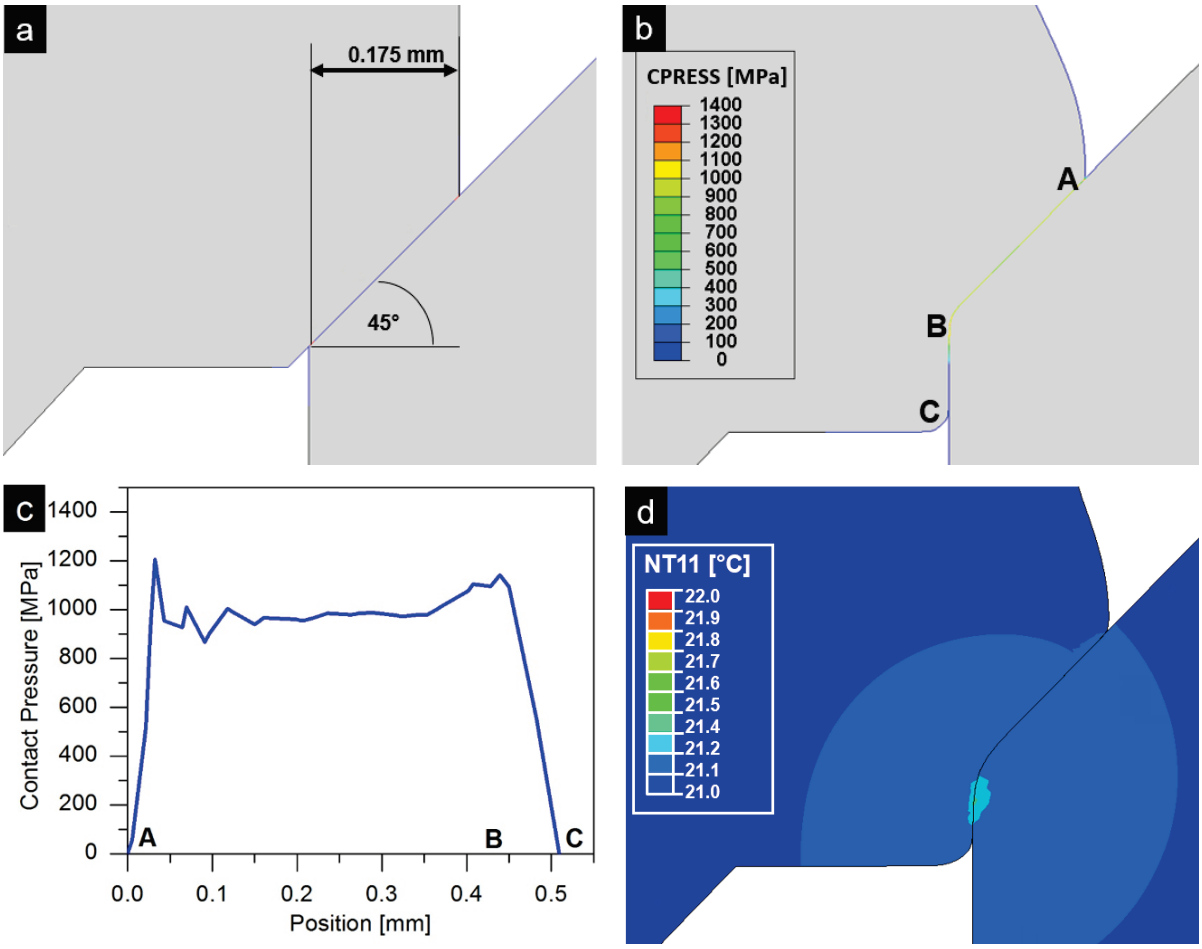

Figure 3-3: Numerical simulation with initial state before pre-loading (a), plastically deformed pre-loaded state of a typical welding geometry with contact pressure (CPRESS) at the contact interface (b), Detailed graph of the contact pressure along the path A-B-C (c) and increase of nodal temperature (NT11) due to dissipation of plastic deformation energy (d).

In addition, the temperature rise due to dissipation of plastic deformation energy was calculated. The additional energy input via dissipation of plastic deformation energy is negligible in the energy balance of the process since a maximum temperature increase of 0.33 °C results at the lower edge of the top part (see fig. 3-3 c). A validation of the

model was done by a comparison with metallographic cross sections. For detailed information, see chapter 6.

3.2 Thermal-electrical effects

3.2.1 Energy analysis based on the example process

The conversion of electrical energy under transient conditions dominates the second and third step of the example process (compare fig. 3-1). Due to imperfections of the welding device, not the whole electrical energy provided by the capacitor bank can be transferred to the fusion zone of the work pieces. There are losses due to transformation of high voltage to high current circuit and also losses in the wiring and tools of the whole assembly (see fig. 3-4).

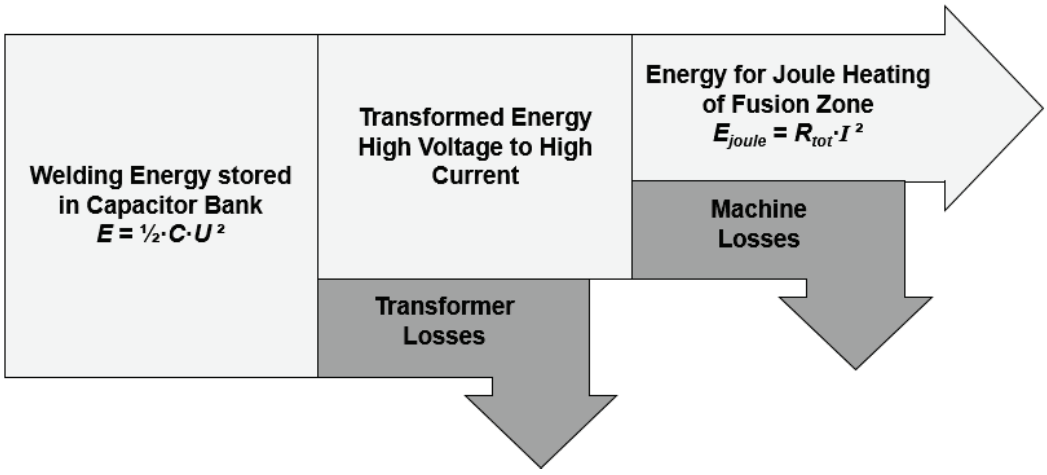

Figure 3-4: Energy Flux Diagram of the example process with capacitor as energy source. Losses due to transformation and machine parts such as wiring and tools lower the welding energy.

The energy transferred to the fusion zone is around 20% to 35 % of the offered energy [5] and can be transferred into heat by the mechanism of *Joule Heating*. This heat generation is a consequence of a local increase in current density at the fusion zone which increases resistivity [3, 65]. The energy released for a given electrical current I and total resistivity on work piece level R_{tot} is given as

$$E_{Joule} = R_{tot} \cdot I^2(x,t) = (R_{mat} + R_c + R_{cont,el}) \cdot I^2(x,t) \qquad (3\text{-}1)$$

The latter one consists of the materials resistivity R_{mat}, the constriction resistivity R_c and the contact resistivity $R_{cont,el}$. These partial resistivities are discussed in detail in the next chapter.

Further, the heating of the fusion zone is also influenced by the loss of heat through thermal conduction within the materials, which removes heat from the interface between the two parts. Furthermore, the specific heat capacity of the material plays a decisive role since it determines the transient materials heating behaviour.

The complete energy balance on fusion zone level can be expressed in terms of these three properties, first the thermal energy pick-up, second the electric energy conversion by *Joule Heating* and third the thermal losses.

$$\rho_{vol} \cdot c_p \cdot \frac{dT}{dt} = \rho_{FZ} \cdot J^2 + \lambda_{th} \cdot \frac{d^2T}{dx^2} \qquad (3\text{-}2)$$

Here, ρ_{vol} is the materials density, c_p is the specific heat, ρ_{FZ} is the electrical resistivity of the fusion zone, J is the local electrical current density, λ_{th} is the thermal conductivity, T the temperature in K and t the time. The first term describes the transient materials heating, the second term stands for the volumetric *Joule Heating* and the last term corresponds to the heat loss within the fusion zone by thermal conduction. Hence to achieve transient heating the ratio between volumetric *Joule Heating* and heat loss must be larger than 1. For complex geometries as used in technical applications, equation 3-2 can only be solved by FEM analysis.

3.2.2 Electrical resistivities

The subdivision of the mentioned electrical fusion zone resistance (volumetric *Joule Heating* term of eq. 3-2) into materials resistance of the base material R_{mat}, geometric constriction resistance R_c and electrical contact resistance R_{cont} is explained in more detail in the following, based on an idealized case.

R_c is related to the sudden geometric change of the parts cross section at the interface whereas $R_{cont,el}$ arises from the microscopic properties of the surfaces in contact, such

as roughness and waviness. An illustration of all three occurring resistances is given in figure 3-5. For a rod shaped conductor (see fig. 3-5) R_{mat} is defined as

$$R_{mat} = \rho_{mat} \cdot \frac{l}{A(r)} \tag{3-3}$$

where ρ_{mat} is the specific electrical materials resistivity, l is the length of the conductor and $A(r)$ is the cross section. Hence, it can be determined directly from the known geometry and materials property.

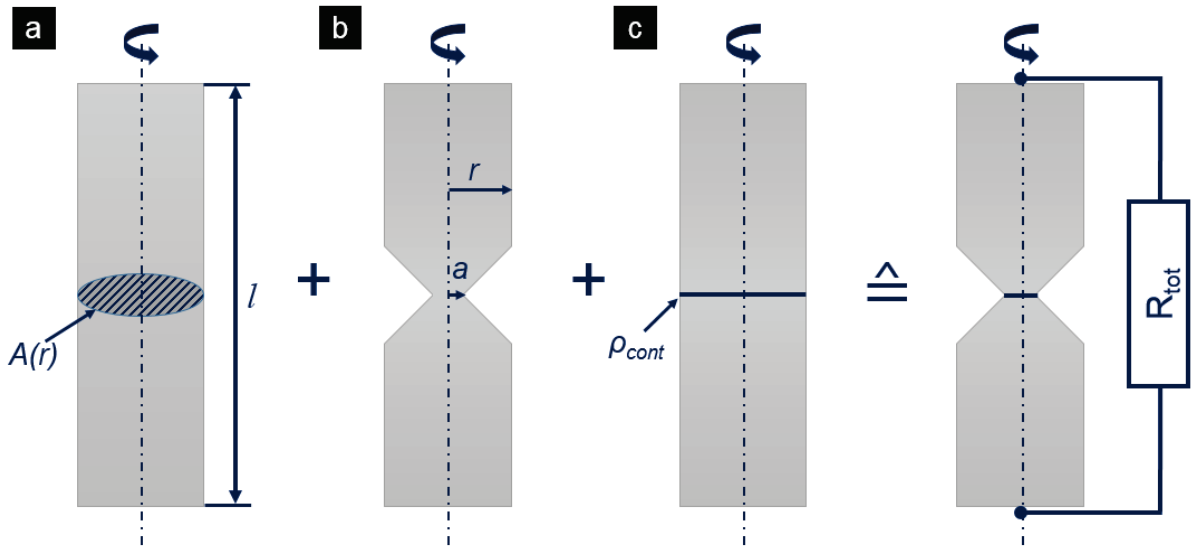

Figure 3-5: Illustration of materials resistance R_{mat} (a), constriction resistance R_c (b) and contact resistance $R_{cont,el}$ (c) for the example of a rod shaped conductor with cross section area $A(r)$ and length l. The superposition of all three resistivities results in R_{tot}.

R_c depends on the ratio between the radius of the constriction a and the outer radius of, in this example, a rod shaped conductor r (see fig 3-5 (b)). *Timsit* [65] derived an approximate solution as follows

$$R_c = \frac{\rho_{mat}}{2 \cdot a} \cdot \left(1 - 1.416 \cdot \frac{a}{r} + 0.063 \cdot \left(\frac{a}{r}\right)^2 + 0.153 \cdot \left(\frac{a}{r}\right)^3 + 0.2 \cdot \left(\frac{a}{r}\right)^4\right). \tag{3-4}$$

Further, a general analytical formula (eq. 3-5) for the constriction resistance of a ring shaped geometry (see fig. 3-6) based on FEM analysis was determined by *Timsit and Nakamura* [67, 68].

$$R_{c,ring} = \frac{\rho_{mat}}{2 \cdot r_0} \cdot F(\lambda) \tag{3-5}$$

Here r_o is the outer radius of the ring and $F(\lambda)$ is a geometrical resistance form factor where λ is the ratio of inner radius r_i and r_o. The geometrical resistance form factor was described by *Yovanovich* [69] in context of thermal contact resistances as follows

$$F(\lambda) = 2 \cdot \pi \cdot \frac{\sqrt{\lambda}}{\ln(8 \cdot \lambda)} \tag{3-6}$$

where λ is defined as

$$\lambda = \frac{\pi}{4} \cdot \frac{\left(1+\left[\frac{r_i}{r_o}\right]\right)}{\left(1-\left[\frac{r_i}{r_o}\right]\right)}, \frac{r_i}{r_o} > 0.1 \cdot \lambda. \tag{3-7}$$

Since a ring shaped contact geometry is often present in projection welding, equation 3-5 is suitable for the estimation of the constriction resistance in annular projection welding.

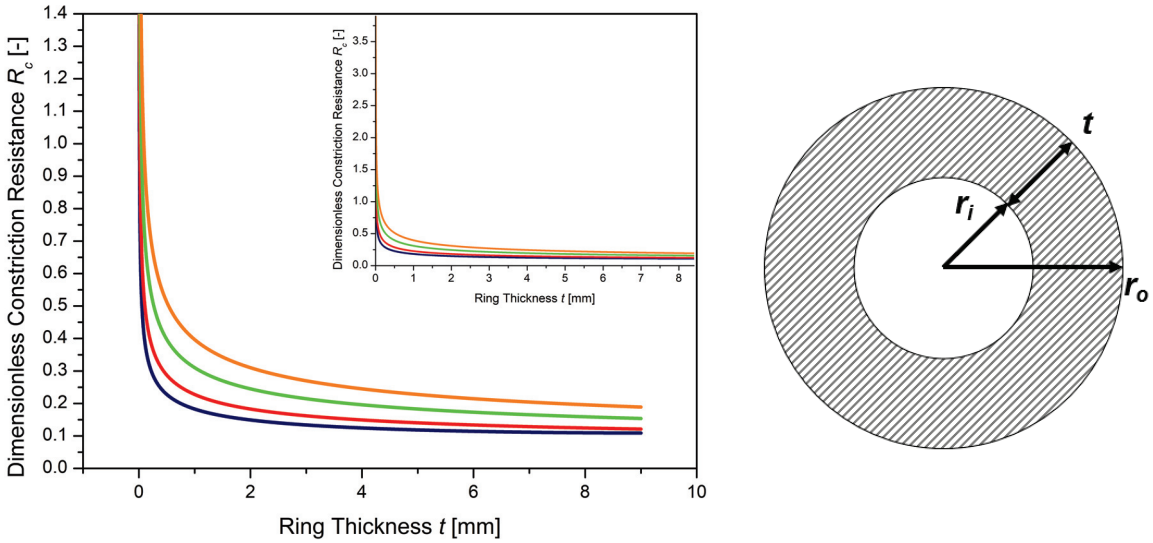

Figure 3-6: Dimensionless constriction resistance for a ring shaped geometry with different outer diameters d_o = 10 mm (blue), 20 mm (red), 50 mm (green), 100 mm (orange) as a function of the ring thickness $t = r_o - r_i$ based on the calculation using equation 3-5 to 3-7.

Figure 3-6 shows the dimensionless constriction resistance as a function of the ring thickness t for an annular geometry with outer diameter d_o = 10 mm in the valid range of equation (3-5). It is obvious that only for a t in the range between near 0 mm and

1 mm R_c is changing significantly by a factor of 3 before reaching a plateau above t = 2 mm. Again, the above equations (3-3, 3-4 and 3-5) can only be solved analytically for simple geometries. For technical geometries, thermal- electrical FEM simulations are the method of choice.

A more complex resistance is the electrical contact resistance $R_{cont,el}$ since it is mainly influenced by the microscopic nature of the contact surface. The basic understanding of electric contacts was essentially influenced by the research of *Holm* [70–72]. Many of his theoretical considerations are still valid and were proved by other researchers later [73]. According to *Holm*, two surfaces brought together only touch in a small fraction (so called α-spots) of the apparent contact area, even if macroscopically flat [70]. This is the result of microscopical roughness where contact is only established between surface asperities (see fig. 3-7).

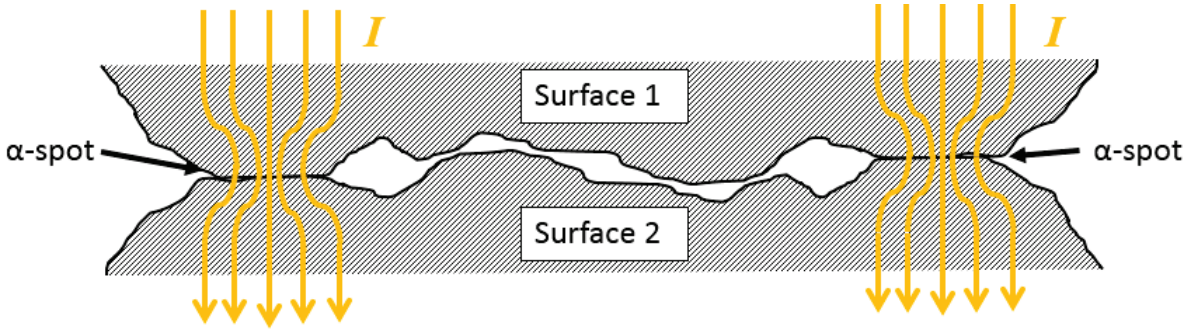

Figure 3-7: Two rough surfaces in contact with current paths across the interface. The real contact area as the sum of α-spots is significantly smaller than the apparent contact area [65].

Since electrical current can only flow through contacting surfaces the area of all α-spots is the real conducting area of the contact. Each single α-spot generates a microscopic constriction for the passing current where equation (3-5) can be applied to calculate the individual asperity constriction resistance.
In general $R_{cont,el}$ is related to the contact area A_{cont} as follows

$$R_{cont,el} = \frac{\rho_{cont,el}}{A_{cont}} \quad . \tag{3-8}$$

In a contact between two rough surfaces an applied normal force F_N leads to an enlargement of the real contact area. The same holds for the number of α-spots which is increasing with increasing F_N [70].

One of the first theories on the mechanical behaviour of rough surfaces in contact was developed by *Greenwood and Williamson (GW model)* [74]. It was extended by *Greenwood* [75] and the following assumptions were made to apply the theory on electrical contacts

- Single asperities can be treated as electrically and mechanically independent and undergo only elastic deformation
- The surface profile was modelled by circles with same curvature but located at different heights of the surface
- Hertzian contact behaviour

Ben Jemaa et al. [76] developed an elasto- plastic model for the description of $R_{cont,el}$. *Popov* derived an expression that states the dependence of $R_{cont,el}$ to F_N via a power law [76] which is also described by *Zhai et al.* [78]. Thus the theories conclude in an analytical expression for $R_{cont,el}$ like

$$R_{cont,el} = K \cdot \rho^* \cdot F_N^{-\alpha} \tag{3-9}$$

where K is a constant depending on the material's mechanical properties, ρ^* is the effective specific electrical resistivity of the materials in contact and α is an exponent depending on the elastic or plastic stress [76]. In variation to the above relation (eq. 3-9), also a pressure dependency of R_{cont} of the same form is also mentioned in [79–82]. Since the definition of $R_{cont,el}$ depends on the application, the force dependent formulation is often found in literature on contact switches and connectors (especially in the elastic regime), whereas the pressure dependent formulation is common in resistance welding applications and numerical simulation (also plastic interaction). Further, the literature study on $R_{cont,el}$ reveals that there is no data for the high mechanical contact loads found in projection welding. An estimation using extrapolated data from measurements in the low mechanical load regime is not satisfying since the extrapolated function strictly depends on the fit parameters. Additionally it is not

obvious that the proposed power law functions up to the yield strength σ_y of the materials.

In context of resistance welding simulation, the relevance of $R_{cont,el}$ as a pressure and temperature dependent interface parameter was already mentioned by *Nied* [38] in 1984, who focussed on the simulation of sheet metals spot welding. This issue was addressed in several publications in the following years [44, 45, 50, 83]. Concluding the facts mentioned above the role of $R_{cont,\ el}$ in projection welding can only be clarified by the determination in the relevant load regime up to σ_y.

In literature two general approaches for the determination of $R_{cont,el}$ can be found. First, the determination from a combination of experiments and simulation for a specific welding process, and second the direct process independent measurement of $R_{cont,el}$ for a simple geometry.

In the first approach R_{tot} is measured in the example process (combination of R_{mat}, R_c and $R_{cont,el}$; see fig. 3-5). In a second step the deformation, contact pressures, contact areas and R_{tot} are calculated using numerical simulation tools. From the comparison of simulation results and experimental data, $R_{cont,\mathrm{el}}$ can then be identified. Examples for this approach are described by *Kußmaul*, *Greitmann* and *Roos* or *Lanier* [44, 45, 50, 83] and also defined in DIN EN ISO 18594 [84] and DVS 2929-1 to 4 [85]. The benefit of this method is mainly the applicability for complex geometries and specific welding tasks (directly from the process). Nevertheless, the challenge is the development of a thermo-electro-mechanical numerical method as well as precise temperature dependent materials data is required.

In the second approach, R_{tot} is measured for a simple geometry. In such a case, R_{mat} can be calculated analytically (see eq. 3-3). If an additional geometric influence on the measurement (R_c) is avoided, $R_{cont,el}$ can directly be determined out of the measured data. Examples for this approach are given by *Holm* [70], *Monnier et al.* [86], *Rogeon et al.* [87] or *Pradille et al.* [88]. The benefit of this method is the easy application of the measurement and a sample design that can quickly be manufactured. The challenge is to ensure a homogeneous contact situation for pressure, temperature and measurement current.

As mentioned above there are several publications on this method using different geometries that can be summarized as follows

- *Holm* used the crossed wire method (see fig. 3-8, a) [70] where the voltage drop across the interface between two crossed wires under normal load is measured.
- *Monnier et al.* [86] used the contact between a ball and a flat plate for the determination of $R_{cont,\,el}$ with OFHC Cu samples (see fig. 3-8, b). The setup can be compared to *Brinell Hardness Testing* and the voltage drop is measured between the ball and the plate.
- *Rogeon et al.* [87] and *Pradille et al.* [88] used a stack of pill-like samples (see fig. 3-8, c). The voltage drop is measured between the first and the last sample and the force is applied in normal direction.

Note that with the experimental setups depicted in figure 3-8, one only measures global parameters like the force F, the current I and the voltage U. The local properties of interest like contact pressure p_{cont} or the local ratio of voltage drop versus current density j_{cont}, hence the local $R_{cont,el}$, are not observed. A priori it needs to be assured that the local contact pressure does not vary along the contact surface and coincides on mesoscopic scale with the average global contact pressure P, i.e. $p_{cont}(x) = P = F/A$ for every position x on the contact surface. The same holds for the electrical current density $J = I/A$.

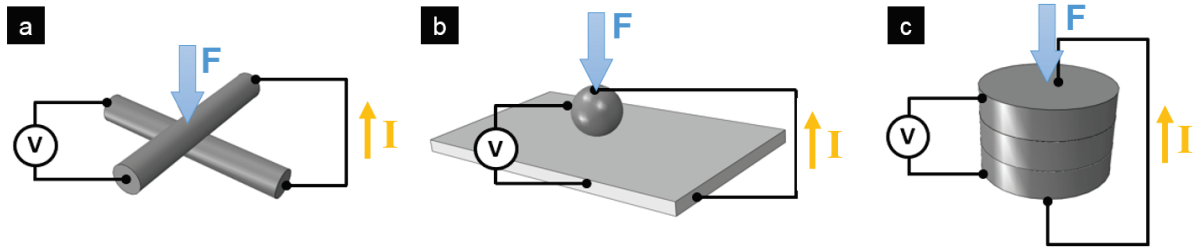

Figure 3-8: Comparison of different sample geometries for R_{cont} measurements: Crossed wire geometry introduced by *Holm* [70], ball- plate geometry for experiments of *Monnier et al.* [86], stack of pill like samples like used by *Pradille et al.* and *Rogeon et al.* [87, 88].

The introduced setups were only tested for way lower mechanical loads than expected in projection welding applications. A use for high contact loads may not be successful in these cases due to the following reasons

- *Holms* experimental setup seems not feasible because massive deformation of the wires will lead to changes in the apparent contact area. The real area of contact is not clearly defined and pressure is likely to be distributed inhomogeneous due to the shape of the resulting apparent contact area.
- Considering the setup of *Greitmann and Roos* as well as the one of *Lanier* a strong dependency on the spot welding process is obvious. Hence, it is not clear if the measured results are independent and transferable to projection welding. Further the effort of numerical simulation, as well as the derivation of a detailed materials model, to determine the electrical contact resistance out of the measurements is high.
- The Setup of *Monnier* et al. may also exhibit the issue of *Holms* setup. Under high loads the ball will indent the plate or vice versa, depending on the hardness of the material. This would also lead to changes in the apparent contact area. Further, the Hertzian Contact between ball and plate exhibits an inhomogeneous pressure distribution. The same holds for the current density distribution because of the sudden geometric change between the spherical ball and the flat plate.

For this thesis the second method and the setup of *Rogeon et al.* [87] and *Pradille et al.* [88] was chosen due to the mentioned benefits. Since the aim of this work is to determine $R_{cont,el}$ in general for projection welding applications (not only for a specified application) this approach seems to be more suitable, especially at high mechanical loads. The cylindrical sample shape enables a homogeneous electrical current density distribution because of no sudden geometrical changes opposed to other experimental setups. Further the $R_{cont,el}$ is measured as the sum of several interfaces which benefits a precise measurement. Nevertheless, the contact pressure distribution cannot be judged a priori.

In order to assess the applicability of the cylindrical test setup for high mechanical loads, the current density distribution and contact pressure distribution must be estimated. For this purpose thermal- electrical and structural FEM simulations were performed using the software tool *ABAQUS*. The model considers three samples with perfectly flat surfaces, stacked between two punches. The structure was subjected to

mechanical loads up to σ_y as well as an electrical current of 1 mA representing the measurement current. A detailed model description with the assumed boundary conditions is shown in Figure 3-9.

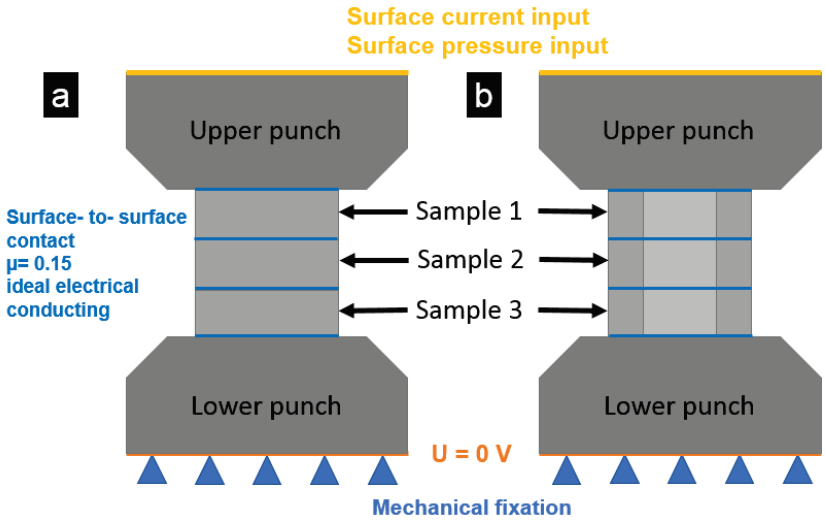

Figure 3-9: Thermal-electrical- mechanical model for estimation of the geometric influence on electrical current density and potential, as well as contact pressure distribution. The initial geometry (solid cylinder) is shown in (a) whereas the optimized geometry (hollow cylinder) is shown in (b).

The results show that for a circular contact area the current density distribution (ECD) (see fig. 3-10 a, right) is not homogeneous. The same holds in principle for the hollow cylinder geometry, but a way better homogenization can be achieved. See the two cases for smaller and larger ring thickness (fig. 3-10, left and mid). Since this observation is a direct consequence of the sudden geometric change between the punches and the samples, the current density can only be further homogenized by keeping this change as small as possible. For this, spacers (height of 10 mm each), having the same geometry as the samples, were inserted. The simulation was then performed again with the new geometric features. Now a homogeneous current density distribution at the spacer- sample- interface, as well as the sample- sample- interface can be found (see fig. 3-10 b). With this optimized geometry, no electrical influence on the resistance measurement is expected. For the contact pressure, the analogous behaviour is shown by the simulation results. The distribution of contact pressure (CPRESS) is not homogeneous for each geometry, neither in the elastic regime (see fig. 3-11, a), nor when σ_y is reached (see fig. 3-11, b). Taking a closer look at the values

of CPRESS it is obvious that the variation ranges from 5 to 15 MPa. Such values can be neglected in comparison to the yield strength of a few hundred MPa.

Concluding the described geometric study, the electrical current density distribution can be optimized using hollow cylinders as samples and spacers for further homogenization. The contact pressure varies within the range of up to 12 MPa and cannot be further homogenized by the geometric optimizations made for electrical current density.

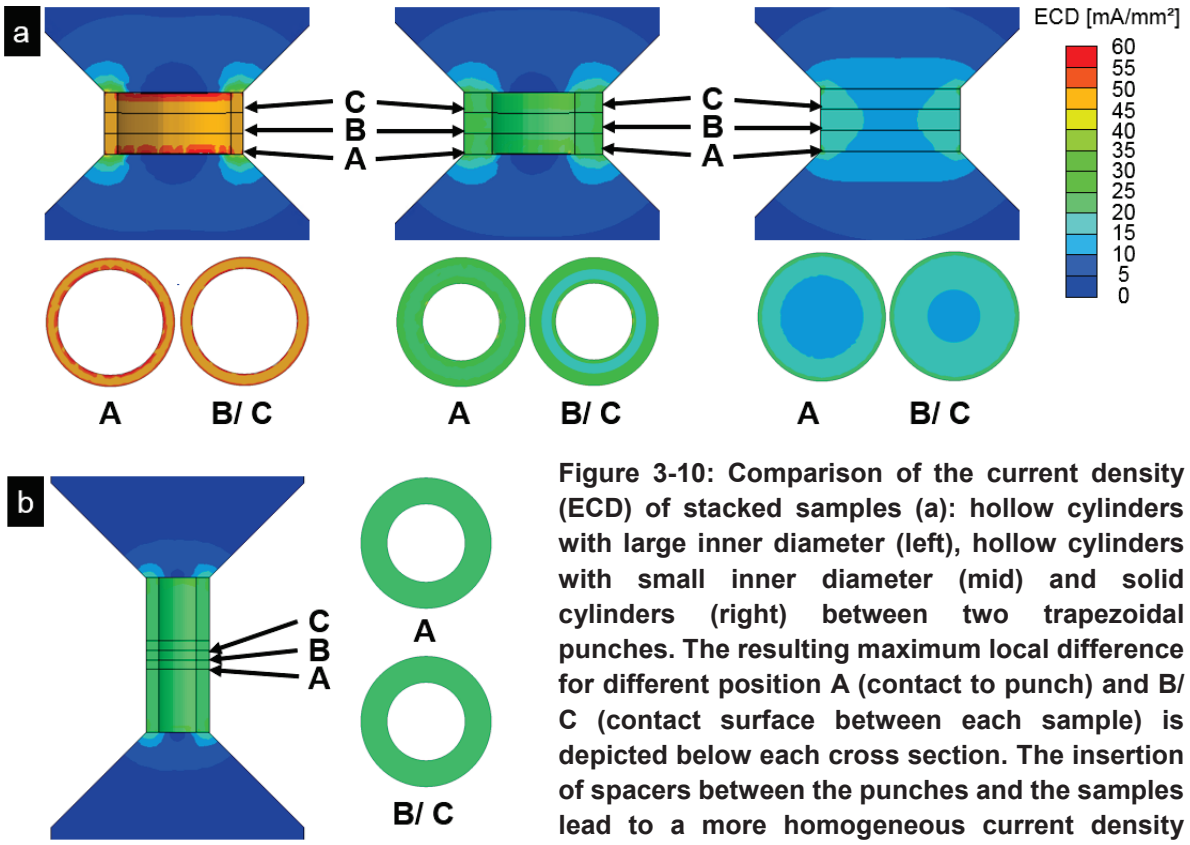

Figure 3-10: Comparison of the current density (ECD) of stacked samples (a): hollow cylinders with large inner diameter (left), hollow cylinders with small inner diameter (mid) and solid cylinders (right) between two trapezoidal punches. The resulting maximum local difference for different position A (contact to punch) and B/ C (contact surface between each sample) is depicted below each cross section. The insertion of spacers between the punches and the samples lead to a more homogeneous current density distribution (b).

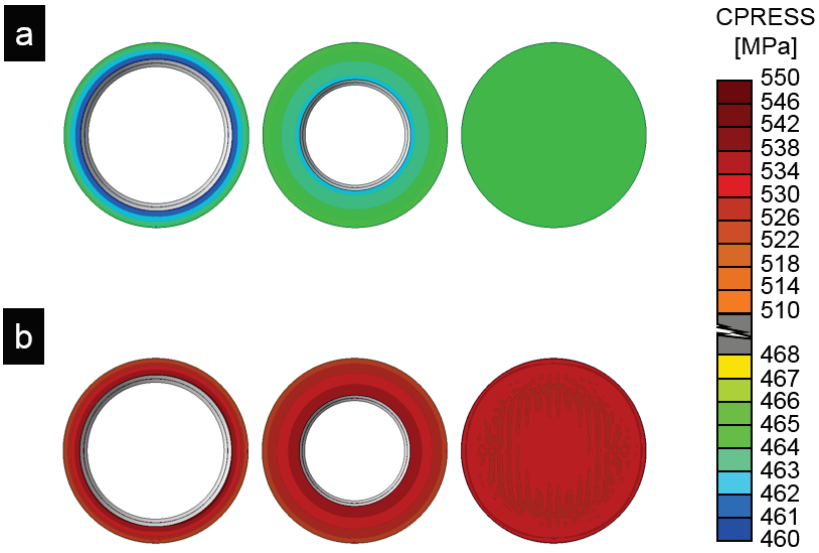

Figure 3-11: Comparison of the different sample geo-metries cross sections at the interface (B, fig. 4) with respect to con-tact pressure distri-bution (CPRESS): In the elastic regime at 460 MPa (a) and at σ_y = 517 MPa of 1.4511 (AISI 430 Nb) stainless steel (b). Note the break and the different step width in the legend for visua-lisation reasons.

3.2.3 Experiments on electrical contact resistances

Based on the preliminary simulation study an experimental setup for the $R_{cont,el}$ measurements was designed from the following points of view

- Geometrical independent measurement of electrical contact resistance at room temperature
- Determination of electrical contact resistances for the high mechanical load regime up to σ_y of the examined materials
- Clarification of the influence of electrical contact resistances for projection welding processes

For examination of the geometric influence, samples with two different contact areas, 25.730 mm² (subsequently “small area”) and 50.265 mm² (subsequently “large area”) were used (see tab. 3-1). The sample height was 1.5 mm for all samples. Electrical and mechanical properties of the materials were taken from the manufacturers’ data sheets (see table 3-2) [89, 90]. The sample material machined to the specified dimensions and contact surfaces were then ground by the aid of a corundum grinding discs. After machining, the samples were ultrasonically cleaned using demineralized water and acetone to remove surface impurities and lubricant leftovers.

Table 3-1: Overview of the sample dimensions used for the experimental determination of $R_{cont,el}$. Inner and outer sample diameters as well as total contact area with errors estimated in appendix B.

	Inner diameter [mm]	Outer diameter [mm]	Contact area [mm²]
Small area	8.20 +/- 0.01	10.00 +/– 0.01	25.7 +/- 0.03
Large area	6.00 +/- 0.02	10.00 +/– 0.05	50.3 +/- 0.31

Table 3-2: Materials properties of the stainless steels used for R_{cont} testing (T = 21 °C) [86, 87].

Material	Specific electrical resistivity ρ [Ω·m]	Elastic Modulus E [GPa]	Yield Strength σ_y [MPa]	Tensile Strength σ_t [MPa]
1.4057 (AISI 431)	0.700	217	719	937
1.4511 (AISI 430 Nb)	0.600	218	517	554

To characterize the surface roughness and waviness according to DIN EN ISO 4287 [91] measurements for each sample type were conducted using a laser confocal microscope (Olympus LEXT OS 4000).

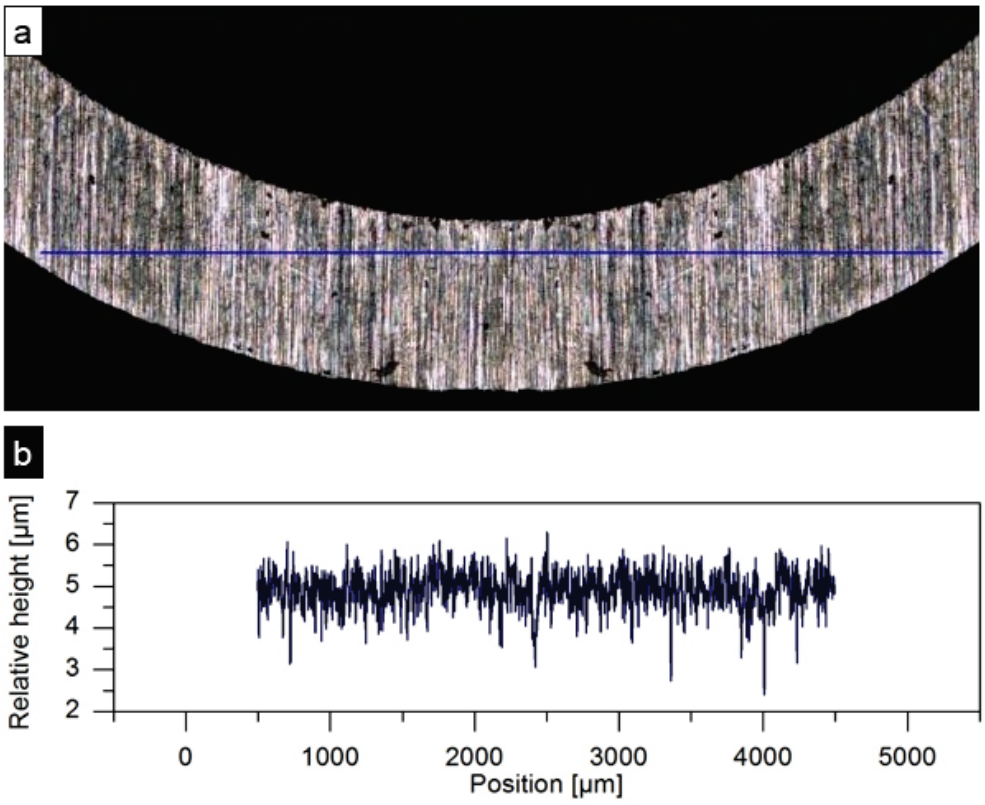

Figure 3-12: Exemplarily microscope image of the sample surface showing grinding groves from machining of the surfaces (a). The measured path perpendicular to the grinding grooves is depicted in blue. The resulting roughness profile is shown in (b).

For evaluation, the data of 10 samples, each for the small and large contact area of both steels, were root mean square averaged. Table 3-3 shows the measurement results. For details on the roughness and waviness, Appendix C gives a definition of each parameter.

Table 3-3: Root mean square surface roughness R_q and maximum height of roughness R_z as well as root mean square waviness W_q and maximum height waviness W_z along (a) and perpendicular (p) to the grinding grooves for the different sample geometries and observed materials. The measurement error is +/- 2% of the measured value. Details can be found in appendix C.

	1.4057 (AISI 431)					1.4511 (AISI 430 Nb)			
	Small area		Large area			Small area		Large area	
	p [µm]	a [µm]	p [µm]	a [µm]		p [µm]	a [µm]	p [µm]	a [µm]
R_z	3.110	1.363	2.926	1.270	R_z	3.058	1.205	3.608	1.462
R_q	0.394	0.212	0.398	0.206	R_q	0.404	0.193	0.478	0.208
W_z	0.427	0.856	0.411	1.271	W_z	0.418	0.647	0.424	1.073
W_q	0.108	0.234	0.102	0.324	W_q	0.097	0.164	0.104	0.254

The setup design prevents tilting of the punches to achieve a homogeneous pressure distribution at the contact surface. By using a guide element frame (see fig. 3-13) a uniaxial state of stress is achieved and tilting of the punches is compensated. An electro-mechanical compression-testing device (Zwick 1476) was used to apply the load to the guide element frame.

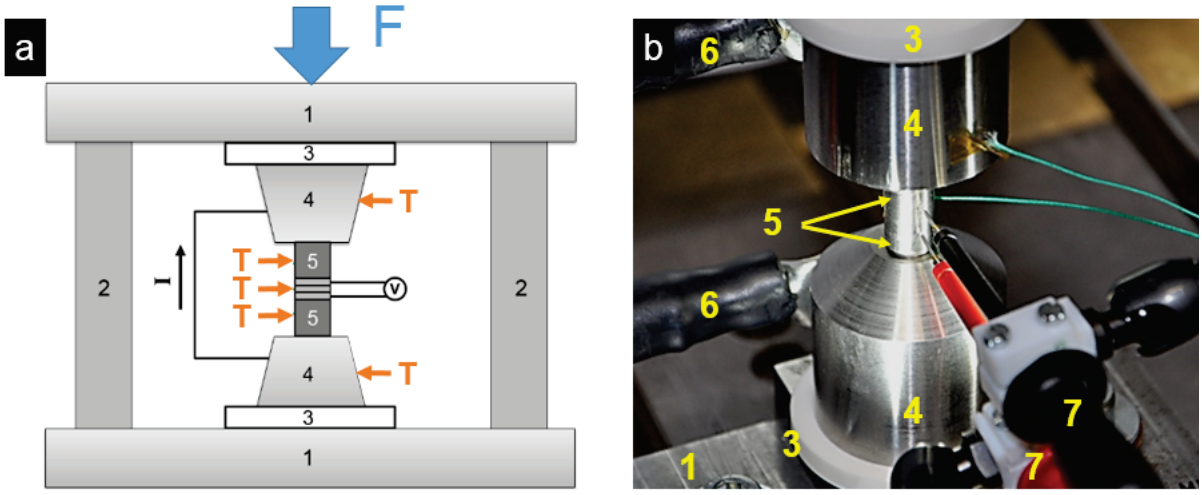

Figure 3-13: Sketch (a) and detail image (b) of the experimental setup consisting of covering/ base plate (1), guide elements (2), electrical insulators (3), upper and lower punch (4), spacers (5), current connectors (6) and voltage drop measurement tips (7). The three samples (light grey) are placed in between the spacers. Thermocouples (T) for tracking of the heat up due to electrical current are placed at five positions of the setup.

For each measurement, three samples were stacked upon each other to double the number of measured interfaces and thus increase the accuracy of the measurement. Between the punches and the samples, spacers with a height of 10 mm, but similar to the shape of the samples, were introduced to ensure the homogenisation of the current flux.

Further, a digital low resistance Ohm Meter (Megger DLRO 200) was used (measurement current 20 A). The voltage drop was measured between the outer samples resulting in a measurement length of 3 mm and two interfaces in between the measurement distance. F_N was increased stepwise until σ_y of the observed materials and/ or combinations was reached. The force was kept constant for a duration of 180 seconds at each step. The first 90 seconds were used to give the system time for dynamical relaxation and thus to establish a constant resistance level. For instance, *Greitmann et al.* and *Lanier* reported a time between 15 s and 70 s needed to reach constant values [45, 50]. After relaxation, the resistance was then subsequently measured 10 times within the following 90 seconds. In such experiments the sum of R_{mat} and $R_{cont,\,el}$ is measured. In order to determine $R_{cont,\,el}$ the subtracted R_{mat} needs to be measured precisely. For this purpose, measurements with the same setup were performed using samples without an interface.

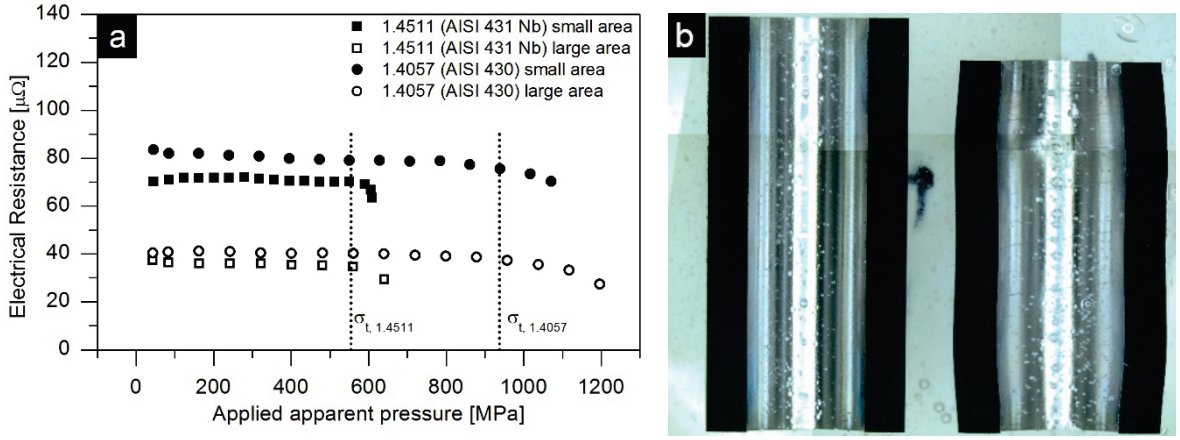

Figure 3-14: Experimental results on the pressure dependent materials resistance R_{mat} (a) and geometries of the samples before (left) and after (right) loading (b). A figure including error bars is given in appendix B.

The height of these samples was chosen to be the same as the height of the stacked samples, including the spacers, for comparison. For each geometry the samples were loaded up to σ_y of the examined material and $R_{cont,\,el}$ was measured at each load step (see fig. 3-14, a). The effect of geometric changes of the samples is included in the measurements and was observed by cross sections before and after loading (see fig. 3-14 b).

Electrical contact resistances R_{cont} were measured according to the experimental procedure described above. The contacts between the combination of both materials as well as the homomaterials were measured for each geometry mentioned in table 3-1. For each measurement the results are plotted versus the apparent contact pressure (see fig. 3-15).

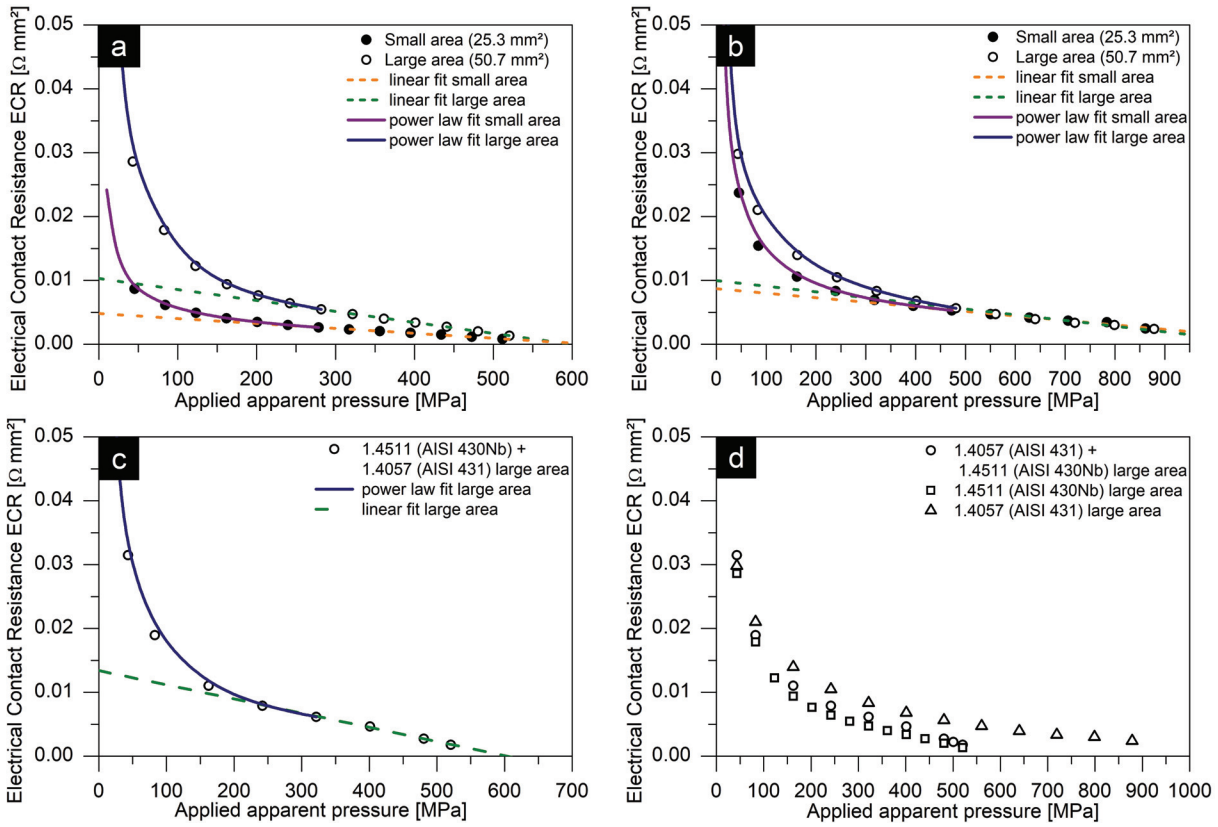

Figure 3-15: Dependency of $R_{cont,el}$ for 1.4511 (AISI 431 Nb) on pressure (a), for 1.4057 (AISI 430) on pressure (b) and for the combination of both materials on pressure (c). For comparison the measurement results for each material and combination are plotted against pressure (d) (A detailed graph including error bars is given in appendix B).

The plotted curves show the same principle behaviour for all measurements. A characteristic decrease in terms of a power law can be observed for the low load regime, independent of the material and the geometry (see fig. 3-15). These observations coincide with the theory and the experimental work introduced before [70, 81, 82, 87].

A difference for the small and large contact area's resistance can be observed for the 1.4511 (AISI 431 Nb) curves. This discrepancy can be explained by the difference in surface properties. The waviness and the roughness of the small contact area samples is smaller than for the large contact area. A smoother initial surface results in a larger contact area with lower electrical contact resistance than for a rougher surface. However, a smoother surface is deformed less due to the larger contact area and hence the electrical contact resistance decrease is smaller within the same pressure range. It is therefore a matter of surface treatment after the machining of the samples. Nevertheless, for both sample sizes $R_{cont,el}$ obviously vanishes when σ_y is approached. The results of the combined contact resistance (see fig. 3-15 d) show the strong impact of the weaker 1.4511 (AISI 431 Nb) stainless steel on the contact resistance evolution. The properties of this material seem to dominate the behaviour with increasing pressure. For the regime around σ_y the curve of the hetero-contact for the material combination adapts to the curve of the homo-contact of the less strong 1.4511 (AISI 431 Nb). As already mentioned, a universal shape of the curves for electrical contact resistance versus mechanical load can be determined. For apparent pressures up to $\sigma_y/\ 2$ the curve shows a power law dependency. For higher pressures, the $R_{cont,el}$ depends linearly on the apparent pressure and vanishes when σ_y is approached (see figs. 3-15 b, d, e). For quantification of the curves fit functions were defined for each regime. The power law regime fit function is defined as

$$R_{cont,el,pwr} = \beta \cdot x^{\alpha} \tag{3-10}$$

whereas the linear regime is represented by

$$R_{cont,el,lin} = \gamma \cdot x + b \tag{3-11}$$

Table 3-4 shows an overview of the fit parameters. The power law exponents α determined after eq. 3-10 do not fit to the prediction of the mentioned theories. These values lie in the range from -0.3 up to -0.66 for the elastic theory [70, 78, 92]. As already mentioned in the introduction (see chapter 3.2.2), these theories only consider elastic effects and *Hertzian Contact*. A force dependent elastic description of the phenomenon by *Popov* [77] determines a value for α = 0.75. Hence, the exponent may differ significantly due to plastic effects or the elastic model assumed to be valid, as the height profile and α-spot distribution is important. This was also reported recently by *Zhai et al.* [78]. They found values for α in the range between -0.5 and 1. Their analytical model is also based on elastic materials behaviour but includes contact stiffness of fractal rough surfaces. In an experimental series, values in between -0.816 and -1.494 for contacts with different surface treatments were found that proved the analytical model [93] for the obviously low pressure range up to around 9 MPa.
The zeroes x_0 of the linear fit are in general larger than σ_y and also σ_t of the examined material (see tab. 3-4). For 1.4511 (AISI 430 Nb) the values are around 50 MPa to 60 MPa above σ_t which is about 11% of the nominal value for σ_t. The discrepancy between x_0 and σ_t is even larger for 1.4057 (AISI 431) where a difference of 260 MPa and thus, 28% of σ_t was found.

Table 3-4: Resulting coefficients of power law fit functions for mechanical loads up to σ_y/ 2 and linear fit functions mechanical loads between σ_y/ 2 and σ_y.

	Power law up to σ_y/ 2			
Material	**Contact area**	***β* [Ω·mm²]**	***α* [-]**	
1.4511 (AISI 430 Nb)	Large	0.859	-0.89	
	Small	0.108	-0.65	
1.4057 (AISI 431)	Large	0.419	-0.68	
	Small	0.258	-0.63	
Combination	Large	0.680	-0.81	
	Linear relation between σ_y/ 2 and σ_y			
Material	**Contact area**	***γ* [Ω·mm²/ MPa]**	***b* [Ω·mm²]**	***x₀* [MPa]**
1.4511 (AISI 430 Nb)	Large	-1.71 x 10-5	1.03 x 10-2	602
	Small	-7.72 x 10-6	4.80 x 10-3	621
1.4057 (AISI 431)	Large	-7.89 x 10-6	9.30 x 10-3	1178
	Small	-7.23 x 10-6	8.72 x 10-3	1206
Combination	Large	-2.22 x 10-5	1.34 x 10-2	603

As for the whole curve of the combined $R_{cont,el}$, again the dominance of the weaker material can be found in x_0. The zero equals the one obtained by the linear fit for the weaker 1.4511 (AISI 430 Nb) material. These observations can be accounted to strain hardening of the materials and thus $R_{cont,el}$, does not vanish immediately as expected when reaching the base materials σ_t.

Quantitatively, this work's results fit well to the ones of *Vogler et al.* (1.0330, AISI 1008 steel) [81] and *Rogeon et al.* (mild steel XES) [87] who performed electrical contact resistance measurements on different steels. The values are in the same order of magnitude for 1.0330 (AISI 1008) steel (see fig. 3-16) whose specific electrical resistivity is comparable to the stainless steels studied here, but the mechanical strength is even lower as that one of 1.4511 (AISI 431 Nb) (see tab. 3-5). *Vogler and Sheppard* performed their experiments only up to 220 MPa, which is significantly lower than σ_y.

Table 3-5: Electrical and mechanical properties of 1.0330 (AISI 1008) steel used for the experiments of *Vogler et al.* [81] and *Rogeon et al.* [87]. All values are valid for room temperature. Data for steel XES is taken from *Aperam Stainless Steel Europe* [94].

Property	1.0330 (AISI 1008)	Steel XES
Specific electrical resistivity ρ_{el}	0.9 Ω·mm²/ m	-
Young's Modulus E	210 GPa	-
Yield Strength σ_y	296.5 MPa	210 MPa
Tensile Strength σ_t	337.9 MPa	240 MPa

Although less clear and not discussed by them, the transition from a power law behaviour to a linear relation between electrical contact resistance and pressure can also be observed in their measurements (see fig. 3-16).
The 1.0330 (AISI 1008) steel exhibits a σ_y of 296.5 MPa. Hence, the transition from a power-law to a linear behaviour should occur at ½ σ_y of 148 MPa. In contradiction, the transition is already observed for a lower pressure at around 110 MPa. Further, the slope of the curve is not as high as for both of the stainless steels. This could indicate a different surface preparation of the samples, since the measurements of the 1.4511 (AISI 430 Nb) stainless steel showed a significant influence of surface properties on the $R_{cont,el}$ evolution.

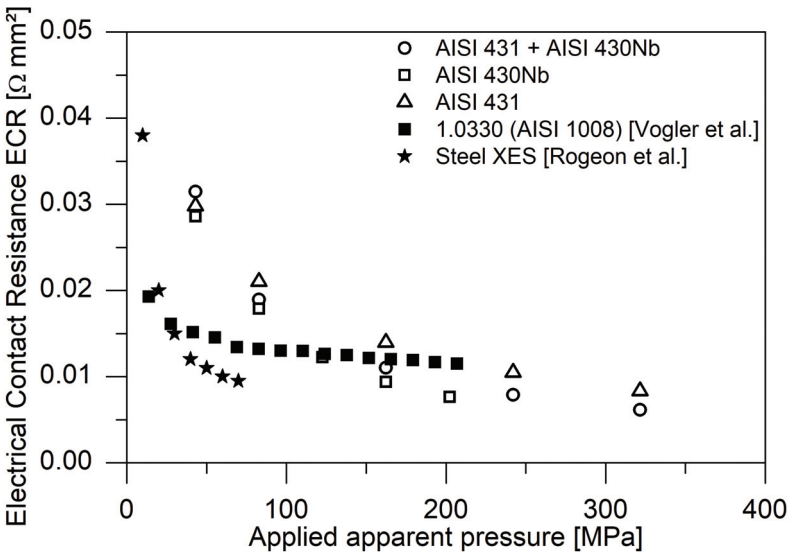

Figure 3-16: Comparison of the electrical contact resistance measured in this work and the work of *Vogler et al.* [81] and *Rogeon et al.* [87].

The results of *Vogler and Sheppard* furthermore show no tendency of the electrical contact resistance to vanish for higher pressures. The slope of the linear regime is too low to approach “0” when reaching the σ_y. This deviation may be accounted to the large overall scattering of the measured values [81] and thus the accuracy in subtraction of the volume resistivity.

Rogeon et al. show a drop of contact resistance for the first 50 MPa in their rsults. Since their measurements were only performed up to 80 MPa neither the σ_y nor the $\sigma_y/2$ was reached but the evolution of the curve fits better to the shape of this work’s results than the one of *Vogler et al.* (see fig. 3-16). The stronger decrease of the electrical contact resistance is related to the weaker mechanical properties of the XES steel. The resulting power law exponent equals to α = -0.749 which is in between the results of this work. Since there are no electrical properties available for the XES steel their influence cannot be discussed.

For the evaluation of the impact of $R_{cont,el}$ on projection welding two further effects need to be considered. According to *Crinon et al.* [95], already a small relative movement of the contact surfaces of two bodies leads to a significant decrease of the electrical contact resistance. This is explained by the shearing of the asperities, which facilitates

the surfaces to adapt to each other. Since such a relative movement also takes place in the pre-pressing step of projection welding, it can be assumed that the contact resistance will already collapse at relatively lower pressures. Thus the values of the electrical contact resistance derived from the measured total electrical resistance would be overestimated.

Further, the steep increase in temperature when *Joule Heating* takes place in the fusion zone can also lower the contact resistance. *Vogler and Sheppard* [81] reported that the electrical contact resistance drops by about a factor of 6 when temperature is changed from ambient to 330 °C. These observations were confirmed by *Galler et al.*, *Rogeon et al.* and *Song et al.* [80, 87, 96]. In the case of a remaining contact resistance in projection welding, it would therefore vanish within the first microseconds of the heating step.

A possible explanation for the linear relation between contact resistance and contact pressure for $p_{cont} > ½\ \sigma_y$ can be given as follows. Considering the two surfaces in contact that were deformed plastically in a way that asperities are already flattened, only small (nanoscopic) pores would remain at the interface, for which the following assumptions are made:

1. Remaining pores are assumed as spherical
2. Remaining pores are distributed homogeneously at the interface
3. Further compression of the interface leads to collaps of the pores by dislocation movement and finally an entirely closed interface

For the derivation of a mathematical expression, a spherical pore at the interface between two cylindrical bodies in contact is considered (see fig. 3-17). Each body has a height of L and a radius of R, the radius of the spherical inclusion is r_i.

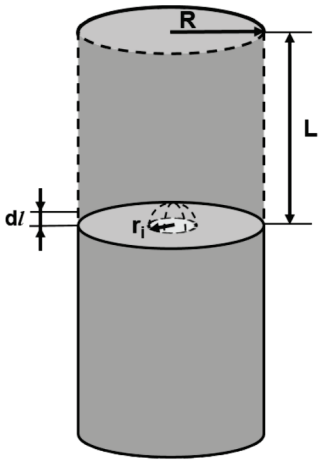

Figure 3-17: Considered model geometry with pore at the interface between two solid cylindrical bodies.

The pore at the interface disturbs the current flux since it deflects the flux lines, as already described by Holm [70–72]. Straightforward integration over the volume of the two bodies in contact gives the additional resistance caused by the pore (a detailled derivation of the equation can be found in appendix D). A final approximate expression for the electrical contact resistance, which gives the correct dependence on the pore radius, is then given by

$$R_{cont,el} = \frac{2 \cdot \rho_{el}}{\pi} \cdot \frac{r_i^3}{R^4} \tag{3-12}$$

or for a parallel circuit of multiple equally sized and homogeneously distributed spherical inclusion at the interface

$$R_{cont,el} = \frac{2 \cdot \rho_{el} \cdot r_i^3}{A \cdot R^2} \tag{3-13}$$

where *A* is the total cross section area at the interface.

Recently, *Kamm* [97] determined the relation between the pore radius and the critical stress needed to let the pore collaps until it is completely vanished. For this, a molecular dynamic simulation model was used to evaluate the stress distribution and dislocation movement at the edge of a spherical pore as a consequence of an externally applied stress. As model material, copper was used. Figure 3-18 shows the temporal progress of the collapsing pore with an increase of the applied stress. The different colours indicate atoms in environment of different crystal structures (green = fcc, red = hcp, white = no structure) [97].

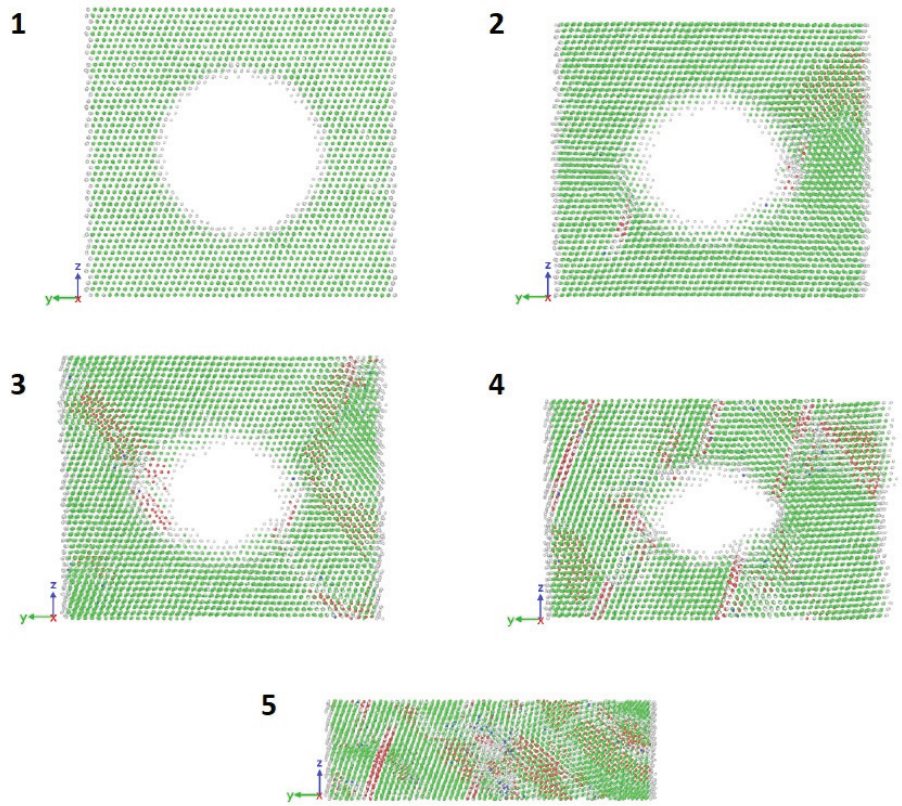

Figure 3-18: Molecular dynamics simulation of a collapsing pore in Cu material under unidirectional stress in z- direction which was increased at constant rate and elevated temperature of 600 K. "1: After initial relaxation (t = 0 s, p = 0GPa); 2: Start of plastic deformation (t = 2:864 ns, p = 3:93GPa); 3: Next recording of coordinates after begin of plastic deformation (t = 2:896 ns, p = 3:935GPa); 4: After passing of another 100 000 time-steps (t = 3:216 ns, p = 3:985GPa); 5: Recording towards the end of the simulation (t = 5:360 ns, p = 4:320GPa), the pore has completely collapsed.", taken from *Kamm* [97].

The relation between pore radius and critical stress found by the analysis of the simulation results is described as

$$\sigma_{crit} = \sigma_0 - \alpha \cdot r^n \tag{3-14}$$

where α is a constant, the exponent n is 2.91 ≈ 3 and σ_0 is the yield strength of the bulk material. Conversion of the equation (3-14) to r^3 and inserting in equation 3-13 leads to the expression

$$R_{cont,el} = \frac{2 \cdot \rho_{el} \cdot \frac{\sigma_0 - \sigma_c}{\alpha}}{A \cdot R^2} = \frac{2 \cdot \rho_{el}}{\alpha \cdot A \cdot R^2} \cdot (\sigma_c - \sigma_0) \tag{3-15}$$

This agrees well to the measured linear relation between applied stress and electrical contact resistance, where the variables b and γ of equation 3-11 can be identified as

$$b = \frac{2 \cdot \rho_{el}}{\alpha \cdot A \cdot R^2} \cdot \sigma_0 \qquad [b] = \frac{\Omega \cdot \mathrm{m} \cdot \mathrm{m}^5}{\mathrm{N} \cdot \mathrm{m}^2 \cdot \mathrm{m}^2} \cdot \frac{\mathrm{N}}{\mathrm{m}^2} = \Omega \tag{3-16}$$

$$\gamma = \frac{2 \cdot \rho_{el}}{\alpha \cdot A \cdot R^2} \qquad [\gamma] = \frac{\Omega \cdot \mathrm{m} \cdot \mathrm{m}^5}{\mathrm{N} \cdot \mathrm{m}^2 \cdot \mathrm{m}^2} = \frac{\Omega}{\mathrm{GPa}} \tag{3-17}$$

Based on the above discussion, it can be concluded that the electrical contact resistance is not significant for projection welding. The results clearly indicate that it vanishes for the high contact pressure occurring in the process.

The developed experimental design is applicable for geometry independent measurements of the electrical contact resistance in the high mechanical load regime. Measurements at elevated temperature would enable a better understanding of the temperature dependency. Further, a theoretical consideration for the experimentally determined linear relation between $R_{cont,el}$ and the contact pressure for $p_{cont} > ½\ \sigma_y$, supports the measurement results. It contributes to a better understanding of electrical contact resistances at high contact pressures.

Additionally, it can be concluded that if a process is focussed at lower contact pressure (e.g. resistance spot welding), the temperature dependency needs to be considered because of a remaining contact resistance at room temperature. Such measurements may therefore also contribute to an improved process simulation model.

3.2.3 Thermal resistivities and transfer of heat

Unlike the electrical current, heat cannot only be transferred across the interface via direct contact over α- spots. In addition, radiation and conduction through the gap medium may take place. The total resistance $R_{heat,tot}$ for heat to pass the interface [98] is given as the reciprocal sum of the thermal resistance arising from the contact between the α- spots $R_{heat,\alpha}$, the thermal resistance due to radiation $R_{heat,rad}$ and the thermal resistance of the gap medium $R_{heat,gap}$ (see eq. 3-18).

$$\frac{1}{R_{heat,tot}} = \frac{1}{R_{heat,\alpha}} + \frac{1}{R_{heat,rad}} + \frac{1}{R_{heat,gap}} \tag{3-18}$$

Figure 3-19 illustrates the three different mechanisms.

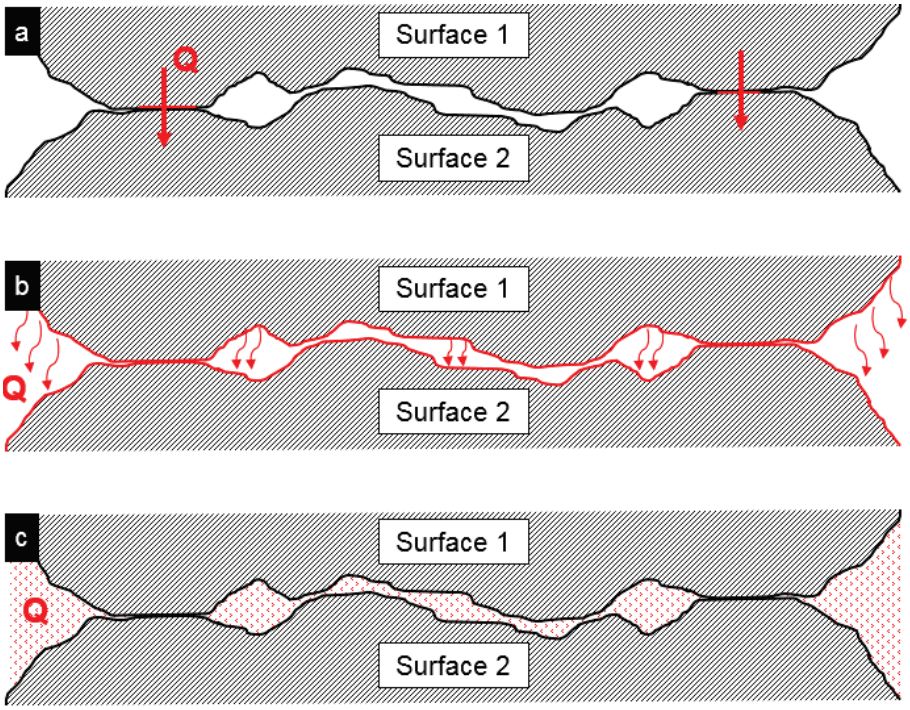

Figure 3-19: Illustration of the heat transport mechanisms in contacts between rough surfaces. Heat transfer is possible via direct asperity contact (a), radiation (b) and gap medium conduction (c).

As valid for the electrical contact resistance the thermal contact resistance of a rough interface is the sum of single resistivities rising from micro constrictions. An analytical description for $R_{heat,\alpha}$ has been given by different researchers like *Mikic*, *Cooper et al.* or *Yovanovich* [99–102]. All the mentioned theories coincide that in general, thermal conductivity depends on pressure via a power law function like

$$R_{heat,\alpha} = 1.25 \cdot \frac{m}{R_q} \cdot \lambda_{therm} \cdot \left(\frac{p_{nom}}{H}\right)^{\gamma} = C \cdot \lambda_{therm} \cdot \left(\frac{p_{nom}}{H}\right)^{\gamma} \qquad (3\text{-}19)$$

where C is a constant characterizing the surface morphology (e.g. roughness), λ_{therm} is the average thermal conductivity of the materials in contact, p_{nom} is the applied nominal pressure, H is the materials hardness in MPa and γ is a power law exponent. The latter one is given for specific materials combinations. m is defined as the mean absolute slope of the roughness profile. The determination of this constant is effortful, since it is only possible with precise roughness analysis. For the bulk material, a ratio

between thermal- and electrical conductivity of metals, λ_{therm} and σ_{el} respectively, is given by the *Wiedemann-Franz Law*

$$\frac{\lambda_{therm}}{\sigma_{el}} = L \cdot T \tag{3-20}$$

where L is the *Lorenz Number* and T is the absolute temperature in K [103]. If this correlation would also hold for thermal and electrical contacts, it would enable the calculation of the thermal contact resistance out of the known electrical contact resistance without the knowledge of the surface properties (e.g. roughness), which are needed for the detailed calculation via the approach of *Yovanovich et al.*. To prove this, the experimental values of figure 3-15 were used for the thermal contact resistance calculation via the *Wiedemann-Franz-Law*. For the approach of *Yovanovich et al.* given literature data such as $\gamma = 0.95$, surface properties $C = 1 \times 10^{-3}$ ($R_q = 0.4$ µm determined in chapter 3 and m assumed to be 4×10^{-4}) [102], were used to calculate the pressure dependence of the thermal contact resistance via equation (3-19). The conversion of the micro hardness into an equivalent stress was carried out according to *Bahrami et al.* [104, 105]. Figure 3-20 shows the calculation results of both approaches in comparison. It is obvious that the calculated values are in the same order of magnitude.

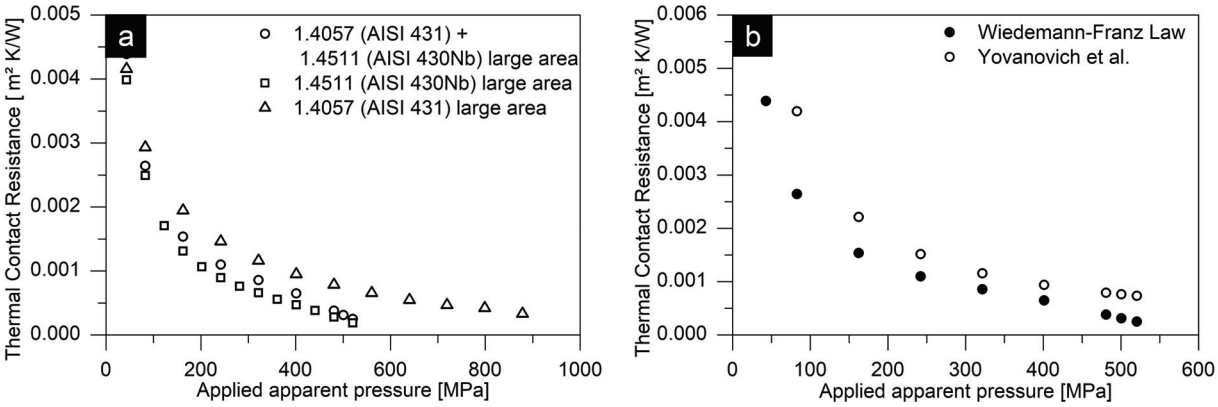

Figure 3-20: Pressure dependency of the thermal contact resistance according to the *Wiedemann-Franz-Law* for 1.4057 (AISI 431) and 1.4511 (AISI 430 Nb) stainless steel as well as for their combination a). Comparison of the results obtained by the calculations with *Wiedemann- Franz- Law* and the correlation given by *Yovanovich* et al. [102] exemplarily for the combination of 1.4511 (AISI 430 Nb) and 1.4057 (AISI 431) stainless steel. For a detailed graph including error bars see appendix B.

The curve based on the theory of *Yovanovich et al.* exhibits slightly higher values than the one described by the *Wiedemann-Franz-Law* (see fig. 3-20, b). *Bahrami et al.* [106] reported that equation (3-19) overestimates the $R_{heat,\alpha}$ for the lower pressure regime due to the assumptions made on their model (they account this effect to the assumption of a Gaussian distribution of asperity heights).

Nevertheless, in case of the results gained from the *Wiedemann-Franz Law*, equation (3-15) overestimates the thermal contact resistance for the whole pressure range investigated. Especially for the plastic regime around 500 MPa, the deviation becomes larger. Here, a limit of the model of *Yovanovich et al.* seems to be reached, since the deformation is fully plastic even in the base material. With these results an estimation of $R_{heat,\alpha}$ based on the *Wiedemann-Franz Law* is a suitable attempt, if electrical contact resistance values were already determined before.

Further, the calculations show that in the contact pressure regime present in projection welding also $R_{heat,\alpha}$ is negligible. Hence, the thermal contact can be assumed as ideal in numerical process simulation models.

The power of heat transfer via radiation (fig. 3-19 b) is described by the *Stefan-Boltzmann-Law* [107] as follows

$$P_{rad} = \varepsilon_{em} \cdot k_{SB} \cdot A_{surf} \cdot T^4 \qquad (3\text{-}21)$$

where ε_{em} is the emissivity coefficient and k_{SB} is the *Stefan-Boltzmann-Coefficient*.

Based on this expression the transferred heat was estimated. The emissivity coefficient was chosen to be ε_{em} = 1, which represents ideal black body radiation. The contact surface was taken from the mechanical simulation of chapter 3.1 (A_{surf} = 31 mm²). Further, a typical temperature profile of the example process was used according to the measurements in chapter 4.2.2 (see fig. 3-21 a). The radiation power as a function of time is given in figure 3-21 b. When the temperature maximum is reached at 22 ms, the radiation power reaches the maximum of 2.6 W. Integration over time results in the total radiation power (dashed area under the power curve in fig. 3-21 b) of P_{rad} = 337.3 W. This equals an energy of E_{rad} = 50.6 J and is only 0.2 % - 0.5 % of typical welding energies. In reality the emissivity coefficient for oxidized steel is only in the range between 0.6 and 0.75 (800 K - 1100 K), determined by *Shi et al.* [105] for

1.4301 stainless steel (AISI 304). For polished steel surfaces values of ε_{em} = 0.52 - 0.56 (700 °C - 1100 °C) are reported [109]. Hence, the values calculated above still overestimate the real heat transport by up to 50 % owing to the assumption of ideal black body radiation.

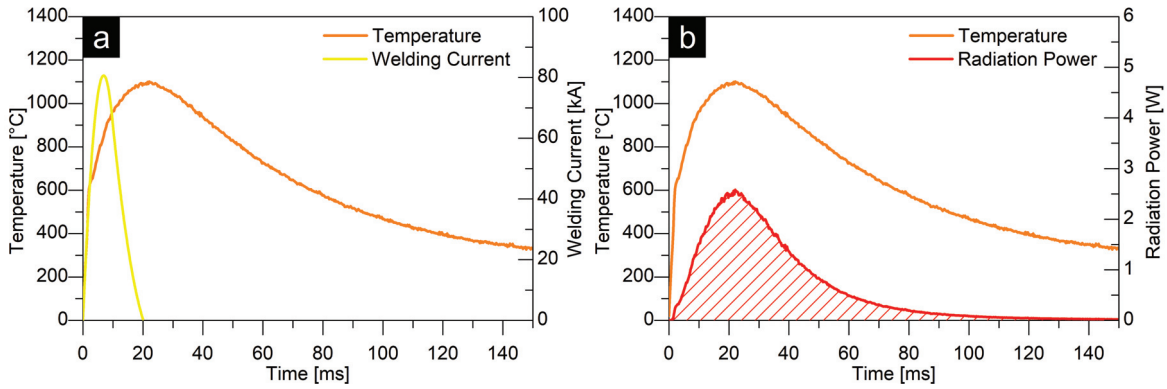

Figure 3-21: Temperature profile for a weld of the example process (a) with typical values for energy and force and calculated radiation power according to the Stefan-Boltzmann Law (b). The dashed area under the radiation power curve represents the total radiation energy transferred within the measured time and the initial contact area calculated in chapter 3.1. For details of the temperature measurement, see chapter 4.2.2.

The thermal resistivity for gap heat transport is mainly influenced by the physical properties of the interaction between the surrounding medium and the body with surface A_{surf}. It can be expressed as

$$R_{heat,gap} = \frac{1}{\chi \cdot A_{surf}} \tag{3-22}$$

where χ is the heat transfer coefficient of the gap medium [110]. For estimation of $R_{heat,gap}$, again, the contact surface was taken from the mechanical simulation of chapter 3.1 (A_{surf} = 31 mm²) in the cold pre-pressed state. Further, the heat transfer coefficient was used according to *Hahn* [108] who states χ = 3.5 - 35 W/ m² K for static ambient air at a metal surface. The calculation results in $R_{heat,gap}$ = 922 to $R_{heat,gap}$ = 9220 K/ W depending on the value of χ. To interpret this value, the maximum heat transfer achieved by convection within the process time is estimated as follows. The power P_{conv} can be calculated according to [110]

$$P_{conv} = \frac{\Delta T}{R_{heat,gap}} = \frac{T_{surf} - T_{amb}}{R_{heat,gap}} \quad (3\text{-}23)$$

where T_{surf} is the surface temperature and T_{amb} is the ambient temperature in K. Assuming T_{amb} = 21 °C, T_{surf} = 1200 °C and $R_{heat,gap}$ = 922 K/ W, P_{conv} results in 1.6 W. For a process time of t = 20 ms the heat q that can be transferred to the ambient air is

$$q = P_{conv} \cdot t = 1.6\,\text{W} \cdot 0.02\,\text{s} = 32\,\text{mJ} \quad (3\text{-}24)$$

This value is much smaller than the heat generated in the fusion zone by *Joule Heating*. Furthermore, heat transfer via convection is only relevant in areas of the fusion zone where no direct material contact is present. Since it is expected that under high contact pressure a complete material contact for the whole contact area is achieved, the convection heat transfer can thus be neglected.

Concluding the above estimations, $R_{heat,\alpha}$ is the only thermal resistance that could affect projection welding. The validity of the *Wiedemann-Franz Law* (eq. 3-20) for the calculation of thermal contact resistances based on electrical contact resistances was validated by comparison with a general thermal contact resistance theory (see fig. 3-20). But even $R_{heat,\alpha}$ can be neglected in projection welding due to the high contact pressures in the fusion zone.

3.3 Electro-magnetic effects

Process steps which involve electrical current, magnetic fields in the order of hundreds of Millitesla occur [112, 113]. Fields of this magnitude can influence the mechanical loads inside the fusion zone by *Lorentz Forces*. Further, a temperature increase due to *Eddy Current Heating* can occur. In order to judge the relevance of these effects on projection welding (and especially when capacitors are used as energy source, like in the example process) the underlying mechanisms are discussed in the following.
The electro-magnetic force arising from *Eddy Currents* can be derived straight forward from the energy density of a magnetic field which is given as [114]

$$W = \frac{1}{2} \cdot \mu \cdot H_{mag}^2 \tag{3-25}$$

where H_{mag} is the magnetic field strength and μ is the magnetic permeability. As for every conservative force field, the force F is the negative derivate of the energy with respect to the position variable x [103]

$$F(x) = -\frac{dW}{dx} \ . \tag{3-26}$$

Combining eq. (3-25) and (3-26) results in the mechanical loads arising from the magnetic field

$$F_{mag}(x) = -\frac{1}{2} \cdot \mu \cdot \frac{dH_{mag}^2}{dx} \tag{3-27}$$

An analytical solution of this equation is not possible for the complex welding geometry, but the forces can be calculated by numerical simulation using the principle of virtual work [114]. In general, the external magnetic field acting on a magnetized body is the average of the magnetic field strength of the surrounding air and the inner magnetic field strength (see fig. 3-21 a). For two bodies in contact, the magnetic force for each body can be calculated by inserting a virtual air gap at the interface (see fig. 3-21 b). The magnetic field strength is then the average of the magnetic field strength of the air gap and counter body.

For the determined magnetic field strength the resulting force for each body can then be calculated via the following equation

$$F = \mu_0 \cdot \int_v (M \cdot \nabla) H \, dv + \frac{\mu_0}{2} \cdot \oint_S (M \cdot n)^2 \, n \, dS \qquad (3\text{-}28)$$

where *M* is the magnetic momentum, v is the volume of the body *S* represents its surface and *n* is the magnetic fields normal vector [115, 116].

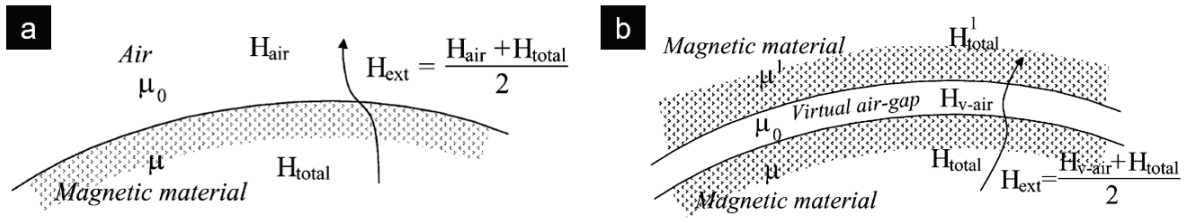

Figure 3-22: Magnetic material with surrounding air where the external magnetic field strength is the average of magnetic field strength in air and the one of the solid body (a). Two magnetic solid bodies in contact virtually separated by an air-gap where the external magnetic field strength on the upper part is the average of the magnetic field strength of the virtual air-gap and the one of the lower body and vice versa. Images are taken from [115].

Since *ABAQUS*, which is primarily used as FEM software in this work, is not able to implement the principle of virtual work, simulations were performed by Robert Bosch Engineering India (RBEI) using *ANSYS Maxwell*. The model was again chosen to satisfy the geometry (see fig 3-23) and current pulse function (see fig. 3-24) of a typical projection welding task with capacitor discharge as energy source.

As in case of the mechanical model presented in chapter 3.1, a cylinder was mounted onto a hollow cylinder forming a contact via two chamfers. The contact was assumed to be a metallurgical joint (tie contact formulation). All materials data used in the model were taken from earlier simulation studies and can be found in the appendix (see app. A). Model boundary conditions were defined like depicted in figure 3-23.

As output, the virtual force was plotted as a function of the process time (see fig. 3-24). From the simulation results, it becomes clear that the magnetic force increases proportionally with the applied current. When the peak electrical current is reached, the virtual force reaches its extremum. As a consequence of the induction, a repulsion of

the two parts can be observed (negative values indicate repulsion, positive values indicate attraction) with a maximum force of 400 N.

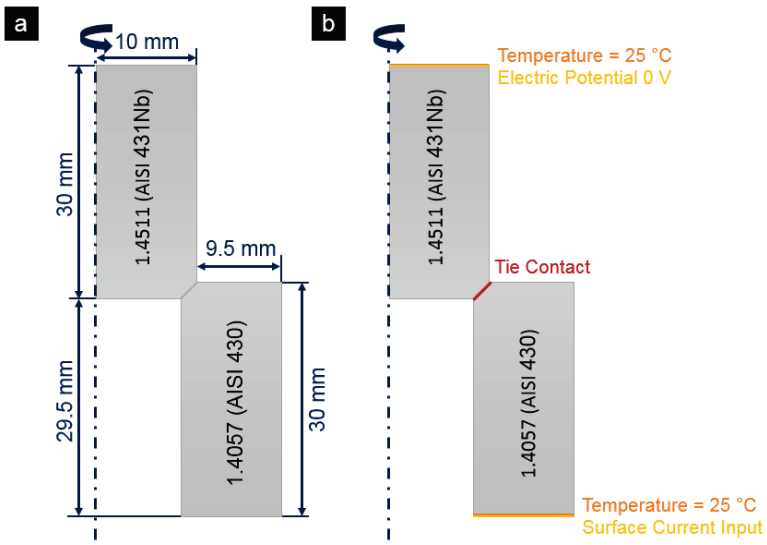

Figure 3-23: Sketch of the geometry obtained by the rotational symmetry (a) and boundary conditions used for *Eddy Current* simulation (b). Note that a 3D model was used for the FEM analysis. The geometries are depicted as rotational symmetric parts for convenient visualization of the boundary conditions.

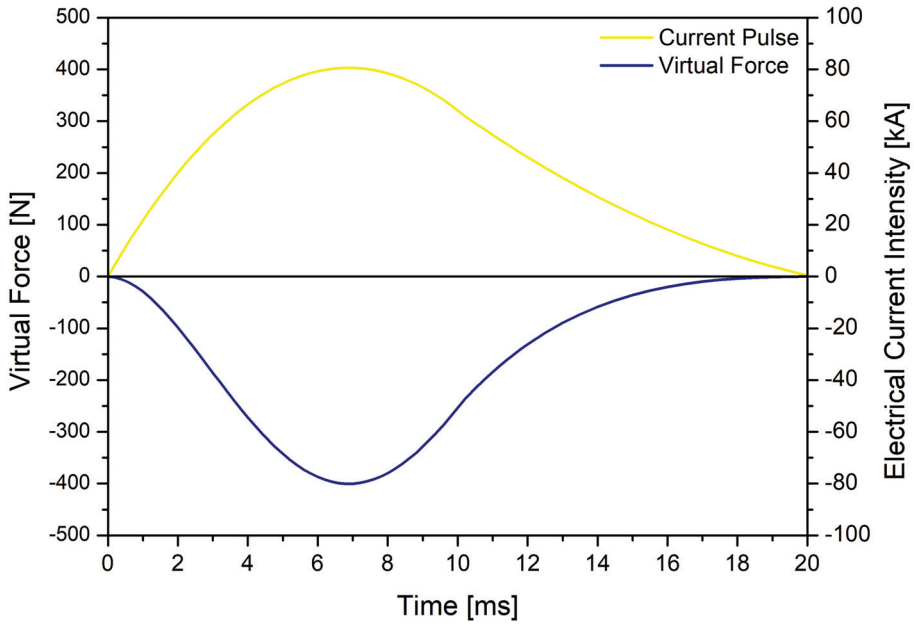

Figure 3-24: Results of FEM analysis of electro-magnetic forces performed by RBEI. The resulting repulsive virtual force (blue line) was plotted as a function of time for the given current pulse (yellow line). Negative values for the virtual force indicate a repulsion of the two bodies whereas positive values indicate an attraction of the bodies.

Compared to the electrode forces known from projection welding (5- 100 kN) the process is thus not significantly influenced by magnetic forces arising from the electrical current.

In addition to the mechanical effect, magnetic fields can also lead to heating due to *Eddy Current Losses* as a consequence of induction of the work pieces. For simple geometries (e.g. rods or wires) the energy loss per unit volume W_{loss} of a magnetic field which oscillates with the frequency *f*, can be expressed as an analytical formula (see eq. 3-29), which can be derived straight forward solving *Maxwell's Equation* [117].

$$W_{loss} = \frac{\pi^2 \cdot B_{peak}^2 \cdot d^2 \cdot f^2 \cdot \sigma_{el}}{6 \cdot \rho_{vol}} \tag{3-29}$$

B_{peak} is the peak value of magnetic field density, *d* is the thickness of the wire, σ_{el} is the conductivity of the material and ρ_{vol} is the volumetric mass density. The presented equation is valid under the assumptions of uniform material and low frequencies of a homogeneous magnetic field that do not allow skin effects.
Since equation 3-29 is only applicable for simple geometries and oscillating magnetic field, the magnetic response of the material on the current pulse of the example process cannot be calculated analytically. Thus, once again an electro-magnetic simulation model was used for the estimation of *Eddy Current Losses.* The same model as for the magnetic virtual force calculations was used and calculations were again performed by RBEI using *ANSYS Maxwell*. The eddy current losses are plotted as a function of process time in fig. 3-25.
The total energy dissipated due to *Eddy Currents* within the 20 ms lasting current pulse was calculated to be E_{loss} = 3.16 J. This value is very small compared to the energy dissipating via *Joule Heating* (10 kJ to 160 kJ depending on the application). From the results it is obvious that the main *Eddy Current Losses* occur at the beginning of the current pulse within the first millisecond. This behaviour can be explained by the sudden increase in current density inside the work pieces resulting in a change of the magnetic field. Once the magnetic field strength reaches values above 10 000 A/ m, a

saturation in the magnetic flux density is approached (see app. A-9). This stops further induction and finally leads to a decrease in *Eddy Current Losses*.

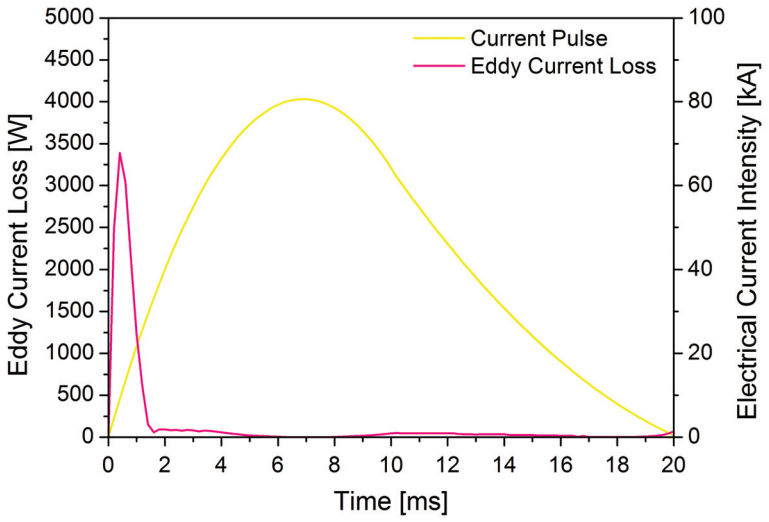

Figure 3-25: Results of FEM analysis of eddy current loss as a function of time.

Concluding the above considerations of magnetic field effects, no significant influence on the process, neither by *Lorentz Forces* nor by *Eddy Current Losses* is expected.

3.4 Conclusion of relevant physical effects

In the above chapters, the relevant physical effects in resistance projection welding, based on an example process with a capacitor discharge, were discussed. The physical quantities that need to be taken into account in numerical process simulations are identified. The specific relevance of the physical effects observed for the example process can be also be assumed in general for other projection welding applications.

3.4.1 Mechanical effects

The contact pressure p_{cont} is a parameter in projection welding, which affects various aspects. It directly affects a deformation of the materials on macroscopic and microscopic level. Furthermore, p_{cont} is linked to the heating behaviour of the fusion zone via the thermal- and electrical contact resistance. In addition, the constriction resistance is related to the mechanical load of the welding device. Due to plastic deformation, the welding force defines the size of the constriction. As shown for the example process, p_{cont} reaches values of 1 GPa and higher.

3.4.2 Thermo-electrical effects

Concerning the electrical effects, only the constriction resistance R_c contributes to significant *Joule Heating* in the process. The electrical contact resistance $R_{cont,el}$ vanishes due to the high contact pressures. Hence, it does not contribute to *Joule Heating*. The materials resistivity R_{mat} is of an order of magnitude that *Joule Heating* does not elevate the temperature of the base material significantly. Since the focus of every resistance welding process is to generate heat locally at the work piece interface, this fact is obvious a priori. Heating of the base material only appears as a consequence of heat dissipation from the fusion zone into the surrounding material. As the high contact pressures also lower the thermal contact resistance $R_{cont,th}$, the heat exchange between the work pieces is not affected by ideal interfaces without any additional barrier. The contribution of radiation and convection is negligible since the interface is almost closed and direct material contact is established.

3.4.3 Electro-magnetic effects

The additional thermal input resulting from *Eddy Current Losses* can be neglected since the energy transfer of the magnetic field is small compared to the welding energy. An estimation of the *Lorentz Force* arising from the magnetic field shows that, compared to the welding force, no additional mechanical loading (or unloading) of the

fusion zone occurs. The repulsive force of approximately 400 N is way smaller than the welding forces of tens of Kilonewton.

3.4.4 Overview

An overview of the estimated quantities and a specific rating (based on the example process) as well as a general rating is given in table 3-6. For the sake of completeness and comparability, the general quantities that are known to influence projection welding (e.g. welding energy) are also listed in the table.

Table 3-6: Estimated quantities as well as a rating of the relevance (specific: based on the example process; general: valid for projection welding) (!: relevant; x: negligible)

Quantity	Magnitude	Specific rating	General rating
Mechanical effects			
Initial Contact Area A_{cont}	~ 31 mm²	-	-
Contact Pressure P_{cont}	[950 … 1100] MPa	!	!
Thermo-electrical effects			
Welding Energy E_{weld}	[10 … 30] kJ	!	!
Electrical Materials Resistivity R_{mat}	[10 … 100] µΩ	x	x
Electrical Constriction Resistance R_c	[0.25 … 3]·R_{mat}	!	!
Electrical Contact Resistance $R_{cont,el}$	[0 … 0.05] Ω·mm²	x	x
Thermal Contact Resistance $R_{heat,\alpha}$ *(p)*	[0 … 0.004 m²·K/ W	x	x
Energy transferred by radiation E_{rad}	50.6 J	x	x
Thermal Gap Resistance $R_{heat,gap}$	[922 … 9220 K/ W]	x	x
Electro-magnetic effects			
Eddy Current Energy E_{eddy}	3.16 J	x	x
Lorentz Virtual Force F_{mag}	-400 N (repulsion)	x	x

4. Joint formation

The following chapter focusses on the joint formation of steels in the solid state. For this, a literature study is used to identify the general physical quantities relevant for solid-state welding processes. Further, the characteristics of projection welding are compared with the ones known from other solid-state welding processes (see ch. 4.1). The example process is analysed using metallography and temperature recording in chapter 4.2. Based on this information, in chapter 4.3, an experimental setup is designed to investigate and independently vary the quantities likely to influence the joint formation for the two stainless steels of the example process. The results of this experimental series are presented and discussed in chapter 4.5. A conclusion of the observations is given in chapter 4.6.

4.1 Introduction

In contradiction to general RW processes, in the example and in many projection welding applications, joint formation occurs in a solid. The following sections give a brief overview over joint mechanisms that are present in SSW processes. Furthermore, the transition from SSW to a liquid state welding (LSW) process is discussed based on the latest literature in context of RW.

4.1.1 Solid state welding processes

Since there is no literature on the joint formation physics of projection welding, this section focusses on the comparison of the process with other SSW processes that exhibit a similarity with respect to mechanical or thermal characteristics e.g. friction welding (FW), friction stir welding (FSW) or hot rolling (HR). Furthermore diffusion welding (DW) also known as diffusion bonding (DB) could reveal similarities with projection welding.

At the beginning of the 20th century, detailed studies of the mechanisms in SSW processes were conducted. A conclusion of the common understanding at that time is given by *Milner and Rowe* [26]. They identified two different theories predicting the bond formation, which enable a direct atom-to-atom-contact between two surfaces. The first one is that an energy barrier has to be overcome to achieve fusion of the surfaces. The origin of the energy was related to rearrangement of atoms (e.g. diffusion) [27] or for recrystallization of the microstructure [28]. The second theory was the break-up of surface oxides to establish a metal- to- metal contact [29]. Later *Mohamed and Washburn* [118] discussed the limitations of the mentioned theories and concluded that each mechanism can only be a part of the whole bond formation in SSW processes. *Tabata et al* derived a criterion for the cold pressure welding of aluminum stating that at least contact pressures of magnitude of the σ_y are necessary to form metallic bonds. For pressures higher than twice the σ_y, the bond formation only depends on the size of virgin contact area [119]. The recent work by *Cooper and Allwood*, who examined the influence of deformation conditions on the strength of aluminum welds, confirms this criterion [22]. Further, they state that a temperature up to one third of the melting temperature T_m is a key factor in SSW since a slight variation leads to a significant increase in bond strength. This phenomenon is linked to increased plastic flow of the material at elevated temperature [22]. They finally conclude that an increase in temperature leads to a decrease of a threshold stress which is necessary to form an intimate metallic contact [22]. Their results also show that the derived criterion predicts the bond strength too low for higher temperatures.

As an example for solid state joining at higher temperatures hot rolling can be adduced. Here the work pieces are rolled upon each other using high pressure and the aid of temperature to form a metallic bond. The degree of plastic deformation is in the range between 100 % and 140 %. *Zhang et al.* [120] examined the HR process for aluminum and magnesium sheets and derived a criterion for bonding. They conclude that the critical stress level for the formation of a metallic bond is reduced with increasing temperature and with increasing degree of plastic deformation. The results coincide with the observations of *Cooper and Allwood* [22] and *Soltan Ali Nezhad et al.* [121]

who state that for higher temperature the degree of plastic deformation is getting more important.

In DW two metal surfaces are brought together under pressure and elevated temperature for a time between a few minutes and several hours [1]. The resulting joint exhibits the highest strength among the various joining technologies which is accounted to the intensive diffusion possible during the long process time and the large area of contact [1]. A typical temperature range is in between 0.5 and 0.8 T_m and hence higher than for HR [1, 119]. The pressures acting on the interface are chosen to be as high as the high temperature σ_y of the respective material. Hence a pressure regime between 5 MPa and 100 MPa is common for DW [1]. E.g. for micro duplex stainless steel joints a pressure between 2 and 12 MPa for 1 ½ to 2 ½ hours at 1298 K is sufficient to form a sound diffusion bond [123]. Due to the long process times the joint formation mechanism proposed for DW [123–126] differs from the mechanisms found in other SSW processes (e.g. HR). DW exhibits three stages that incorporate

- The establishment of the surface to surface contact (see fig. 4-1 a)
- The surface deformation that leads to the generation of an intimate interface (see fig. 4-1 b)
- The migration of grain boundaries and incorporated elimination of surface voids (see fig 4-1 c)
- Finally the elimination of pores supported by volume diffusion (see fig. 4-1 d).

The influencing parameters on DW are temperature, pressure, time and surface condition, process environment [124–126]. These parameters may act as follows

- The temperature influences the diffusivity of the atoms and the mechanical behaviour of the materials. With increasing temperature diffusion becomes faster and σ_y decreases, i. e. plastic deformation becomes more pronounced at constant stress.
- The pressure upon the interface supports the deformation of the surface asperities (see fig. 4-1). Further surface oxides and impurities are broken up and sheared away from the fusion zone which enlarges the contact area for intimate atomic materials contact. It is reported that the pressure is a critical parameter within the initial contact and the first stage [125]. For the second and

third stage a reduction of the contact pressure may not negatively affect the bond quality [125].

- The process time, which is significantly larger than for other SSW processes, enables long range diffusion and the formation of a strong atomic bond between the work pieces. The deformation of the interface also increases with the process time and supports the formation of a large contact area. Due to this, the process time is chosen according to pressure and temperature.
- Surface corrugations such as roughness and waviness or the presence of oxide layers and impurities hinder the formation of the intimate contact and so the evolution of a strong diffusion bond.
- An inert atmosphere or vacuum prevents the surfaces from oxidation and support the joint formation. For this reason diffusion bonding is mainly performed in a controlled atmosphere.

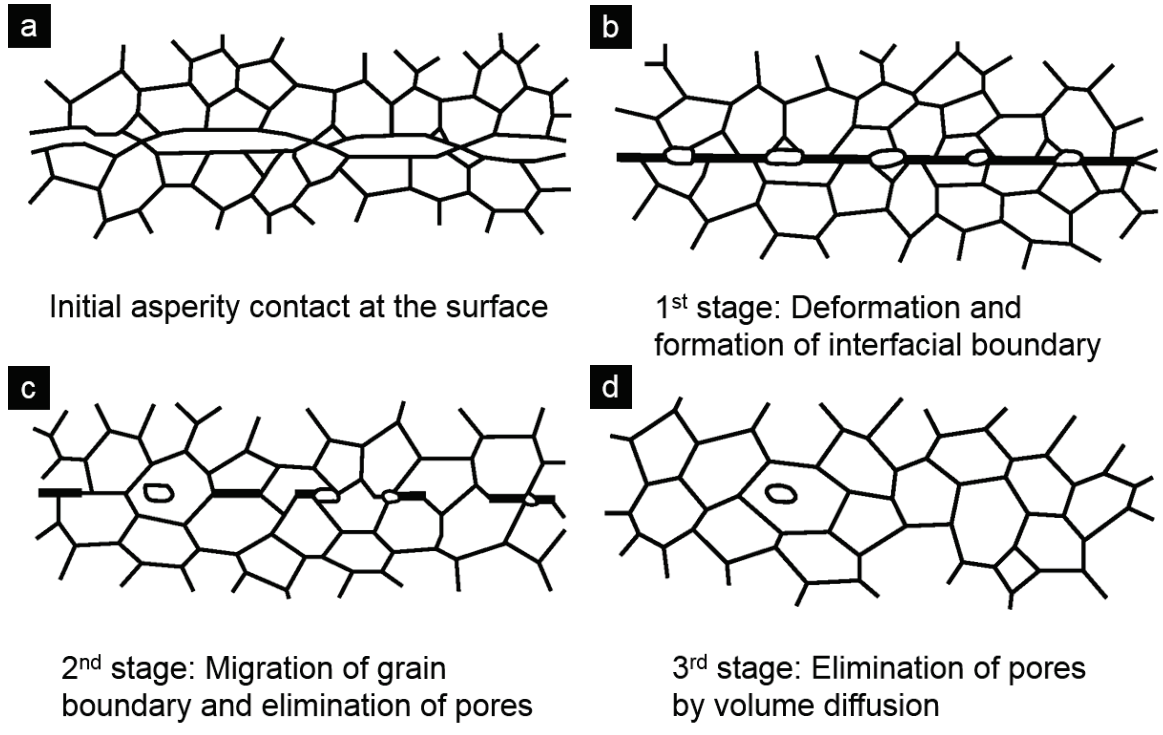

Figure 4-1: Illustration of the stages of diffusion bonding involving initial asperity contact (a), deformation and interfacial boundary formation (b), migration of the grain boundaries and elimination of pores by grain boundary and surface diffusion (c) and elimination of remaining pores by volume diffusion during longer annealing (d) taken from [124, 125].

Diffusion bonding was, among other materials, studied for stainless steels [123, 127], cast iron [128], carbon steels [129, 130] or non- ferrous materials combinations like nickel base alloys [122] or copper and titanium [131]. In all of these studies the temperature level was kept for a time between 6 minutes [130] and 24 hours [122] which is significantly longer than the process time of projection welding applications. Further, the experiments were performed in a vacuum atmosphere.

4.1.2 Resistance welding processes

The transition from SSW to a liquid state process is not as well defined as one may assume. A study of *Fukumoto and Zhou* on resistance micro welding (RMW) of crossed nickel wires concludes that a combination of solid phase welding and liquid phase welding occurs [10]. They state that only the interface between the two wires melts due to the current. A wetting of the solids and cleaning of the interface from impurities takes place. The impurity containing liquid phase is squeezed out of the fusion zone leading to a flash. The welds exhibits a non-molten recrystallized microstructure in the heat-affected zone (HAZ) [10].

For capacitor discharge powered resistance welding of steel, *Dattoma et al.* [132] found a correlation between fusion zone strength and welding force or welding energy of the examined butt welds. They state that with increasing force or increasing welding energy the strength of the joint is increasing [132]. *Carofalo et al.* and *Palano et al.* recently described an optimization of the joint strength by variation of the contact profile [133, 134]. The outcome of their work is that the initial contact area is a significant parameter for the joint strength.

Regarding the temperature profile, RW processes exhibit the highest cooling rates among many joining processes (e.g. laser welding or gas metal arc welding). The cooling rates can range from 2000 °C/ s to 100 000 °C/ s [135]. This fact complicates a detailed observation of the joint formation in projection welding (especially with capacitor discharge as an energy source). In addition, projection welding with

capacitors exhibits very higher heating rates than known from other current sources for RW due to the high electric current density.

4.1.3 Conclusion of literature study

The above literature study reveals that high plastic strains and high temperatures support the formation of metallurgical bonds in the solid state, while the presence of oxide layers inside the contact interface is a critical factor. Since stainless steels do not tend to form massive oxide layers (e.g. like known from aluminum) the key to successful prediction of the joint formation is in this case the knowledge of the temperature profile and pressure.

One should notice that the above studies on SSW were performed at lower temperatures than expected in projection welding, but they also give the outline that the prediction of bond strength for high fusion temperatures is possible when taking into account the temperature dependency of diffusivity and mechanical materials parameters [22]. Furthermore, the source of heating differs significantly since internal *Joule Heating* sources the thermal energy input in projection welding, whereas for the processes described above, thermal energy is transferred from ambient to the work pieces. In the previous discussion on joint mechanisms and parameters some synergies were identified between projection welding and the general theory of joint formation in SSW. The following significant parameters are identified as

- *Temperature Profile:*

  The temperature profile is influenced by the welding energy. An increase of welding energy leads to a higher temperature. The upper temperature level is limited by the melting of the material inside the contact area. Here namely the limit of SSW is reached. According to the DW theory the elevated temperature supports deformation of the interface and the evolution of atomic bonds.
- *Contact Pressure:*

  The contact pressure is a function of the welding force. It is needed to generate sufficient contact area in the initial stage of the process. If the pressure is too low, $R_{cont,el}$ is too high and the fusion zone is overheated leading to a liquid

phase which is expelled from the fusion zone. If the contact pressure is too high undesired massive plastic deformation may occur. Further the contact pressure supports the formation of a pore free interface. Stresses in the normal direction of the contact enable an intimate contact between the involved metals and are the prerequisite for the formation of metallic atomic bonds.

- *Interfacial Stresses:*
  The interfacial shear stresses are necessary for the break-up of oxides and the removal of surface impurities.

4.2 Characterization of the example process

To create a basis for understanding the joint formation, metallography, temperature measurements and mechanical testing was used to characterize the example process. Furthermore, these results provide the necessary data for the validation of numerical process simulations and pictures the details of each process step. The general procedure for qualification and quality assurance of resistance welds are regulated by the European Standards DIN EN ISO 15614-12 [136] and DIN EN ISO 6520-2 [137].

4.2.1 Metallographic characterization

For analysing the influence of the welding process on the materials microstructures, metallographic cross sections were prepared. The samples were cut perpendicular to the interface (along the sample length) embedded, ground, polished and finally etched using hot “V2A etching reagent” (Schmitz Metallografie GmbH). For imaging a stereo microscope (Zeiss Stemi 2000), a light microscope (Olympus BX-51) and scanning electron microscopes (Phenom Pro X; FEI Quanta 250) were utilized.
To comprehend the temporal development of the fusion zone the process was stopped artificially using a mechanical stopper that also deflected the remaining welding current from the sample. This stopper was adjusted in steps of 0.1 mm between 0.2 mm and 0.8 mm what represents the process stop at different process times ranging from 6 ms to 14 ms. For the welding tests a c-frame welding device (GLAMAtronic GKS-C) with

maximum 25 kJ welding energy, 250 kA peak current and 45 kN welding force was used.

Figure 4-2 shows the temporal evolution of the fusion zone for the same welding energy and welding force but different welding distances d_w (respectively timesteps t).

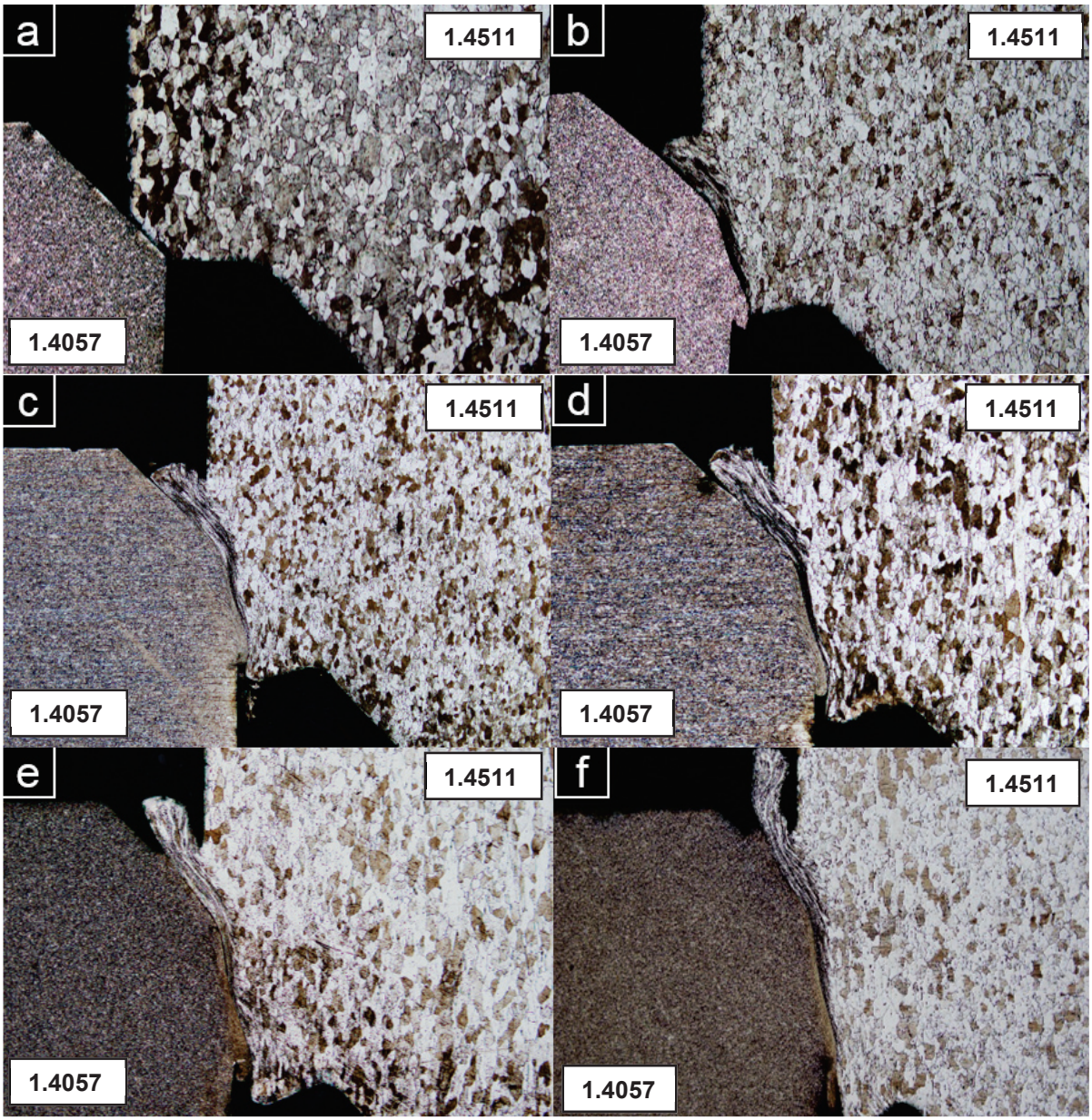

Figure 4-2: Artificially interrupted process cross sections to show the fusion zone evolution during the projection welding process for a) initial state of contact: t = 0, d_w = 0 mm, b) t = 6.6 ms, d_w = 0.24 mm, c) t = 7.4 ms, d_w = 0.36 mm, d) t = 8.0 ms, d_w = 0.58 mm, e) t = 10.1 ms, d_w = 0.79 mm, f) without mechanical stopper: t = 14.0 ms, d_w = 1.34 mm. The material of the top part is 1.4511 (AISI 430 Nb) and the material of the bottom part 1.4057 (AISI 431).

Even for high-magnified images, no diffusion effects are visible in the cross section images (see fig.4-3). Neither the interface between the work pieces vanishes, nor a diffusion seam is visible. The concentration changes only for Ni, since the 1.4057 (AISI 431) has a Ni content of 2 wt.-% whereas the 1.4511 (AISI 430 Nb) exhibits no measurable Ni content. Thus, the interface is indicated by a sudden jump in the Ni concentration profile. In vicinity of the interface, inside the ferritic 1.4511 (AISI 430 Nb), recrystallization can be observed within the first 30 µm from the interface (see fig. 4-3 a and b).

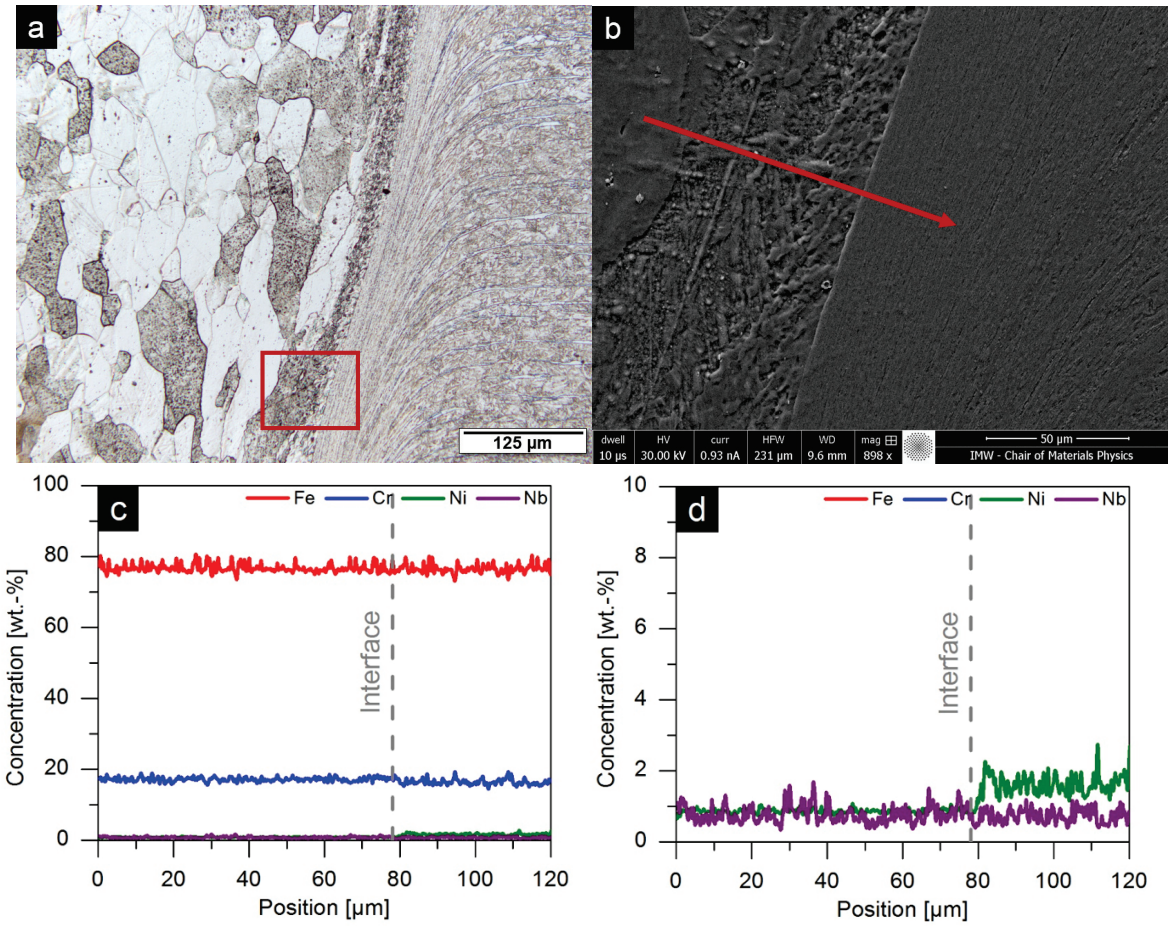

Figure 4-3: Detail image of the fusion zone. Light microscope image (a), scanning electron microscope image of the marked area with EDX line scan (b), concentration profile along the EDX line scan (c) and detail of the concentration profile to show the lower concentration elements. The interface between the work pieces is still present for sufficient and insufficient welds. A change in composition is only visible for Ni since the 1.4057 (AISI 431) (right side of the image) has a Ni content of 2 wt.-% while the ferritic stainless steel is practically Ni free.

It is promoted by the severe plastic deformation that occurs in this area and initialized by the elevated temperature. Farther away from the interface, the process does not influence the base materials. The recrystallization also shows that re-ordering processes occur, to form the joint.

4.2.2 Temperature measurements in the example process

To get an insight of the relevant temperatures for the joint formation in projection welding and to validate the numerical simulations, temperature measurements were performed during the process. For this, a high frequency temperature measurement device was used (ADWin Pro II). A measurement interval of 0.3 ms ensured a high temporal resolution of the temperature profile. The thermocouples were fixed on the sample surface by laser welding (HC handlaser AV100). This method enabled a small contact point of 140 +/- 20 µm in diameter and thus a high spatial resolution. An array of eight thermocouples, with an angle of 45° in between, was placed on the bottom part next to the chamfer that forms the contact area between the two work pieces (see fig. 4-3). The position of each thermocouple with respect to the fusion zone was measured by light microscopy (Zeiss Stemi 2000 C). Figure 4-4 shows an example of a welded thermocouple.

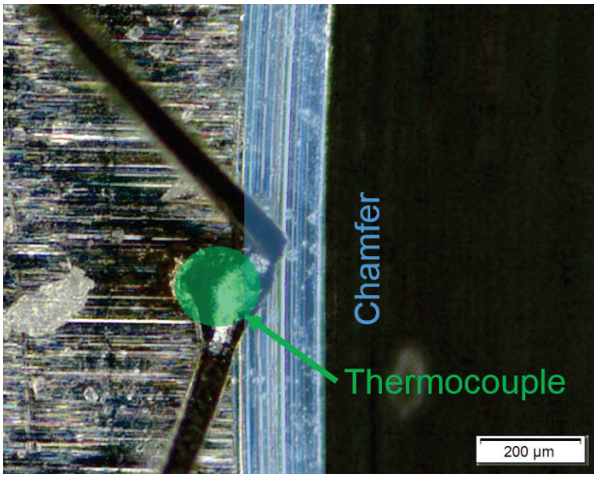

Figure 4-4: Optical microscope top view image of a welded thermocouple. The contact area of the thermocouple is marked green whereas the chamfer is illustrated in blue.

Since the microscope image only provides a planar measurement (distance d1 in fig. 4-5 b) the absolute distance (distance d2 in fig. 4-5 b) was calculated using the chamfer angle. It was possible to place the thermocouples in a mean distance of 731.6 +/- 77.5 µm to the fusion zone. The temperature measurements were performed for different welding energies. First, the welding energies were chosen according to the lower limit for successfully welded parts. In the following, the energy was stepwise increased until it was about a factor of 2 larger than the lower limit. Note that since the device performance differs between different welding devices (effect of manufacturing tolerances of the device and the capacitors) the energies are not explicitly mentioned. Furthermore, the current pulse shape and maximum is taken as a quality measure to be linked to the welding result. For all experiments, the welding force was kept constant to ensure comparability of the temperature profiles.

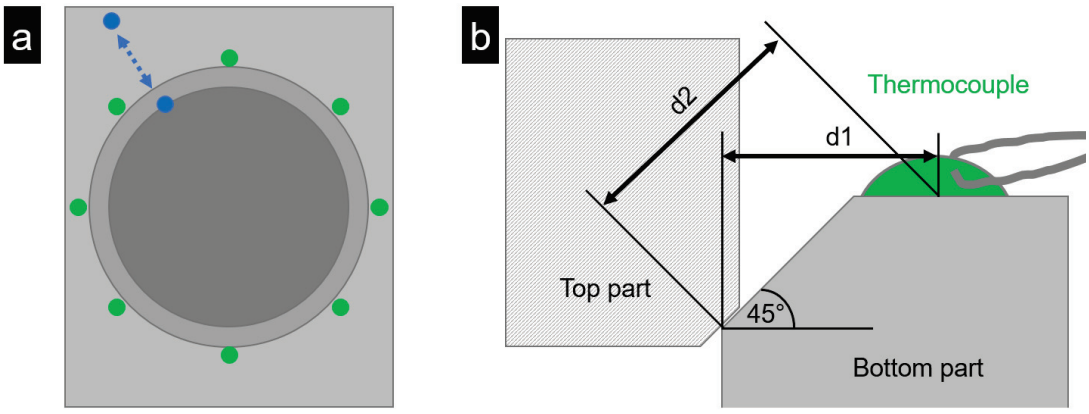

Figure 4-5: Top view of the thermocouple positions (green) on the bottom part of the welded geometry (a) and definition of the distances to the fusion zone in a cross section view (b). In a further measurement series the distance of the thermocouples to the fusion zone was varied systematically (blue dots). The welding geometry is the same as assumed for the mechanical simulation in chapter 3.1. The upper part is marked as the dashed area.

The measured temperature evolutions (see fig. 4-6) show an offset between the maximum of temperature and the maximum of the electrical current. Whereas the maximum of the electrical current is reached at around 7 ms (compare fig. 3-24) the maxima of the temperature range between 15.5 ms and 22.5 ms. This can be interpreted as the consequence of the spatial offset between the thermocouples and

the fusion zone. Since the heating of the fusion zone is directly linked to the applied current, the maxima should be reached simultaneously. To judge these results the temperature conductivity λ_{temp} is taken into account, which is a function of the specific heat c_p and the materials density ρ_{vol}. It is defined as [138]

$$\lambda_{temp} = \frac{\lambda_{therm}}{\rho_{vol} \cdot c_p}. \tag{4-1}$$

The time shift τ for a distance d from the heat source can then be calculated via [138]

$$\tau = \frac{d^2}{\lambda_{temp}} = \frac{\rho_{vol} \cdot c_p \cdot d^2}{\lambda_{therm}}. \tag{4-2}$$

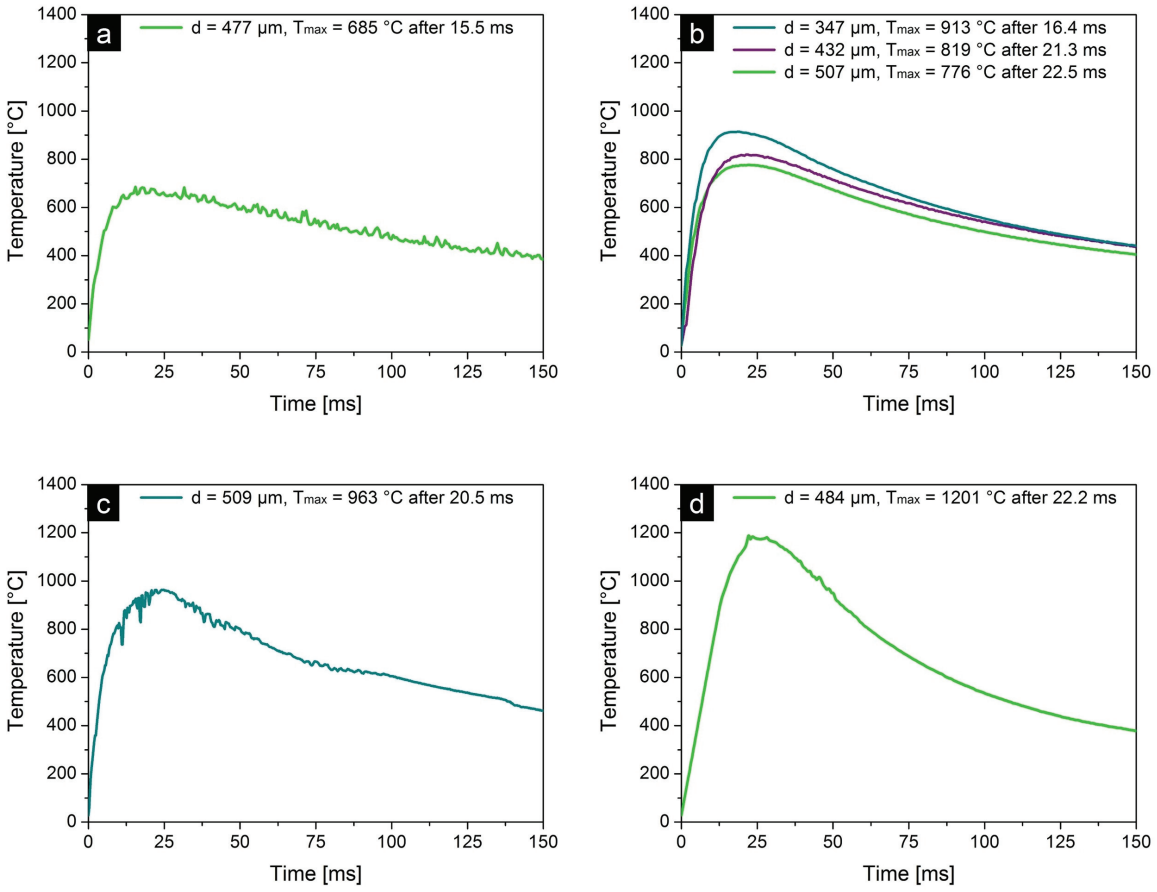

Figure 4-6: Temperature profiles measured for increasing welding energies from (a) to (d). The welding energy used for (a) was not sufficient to form a metallurgical joint. Figure (b) shows the temperature profile of the lower limit for sufficient metallurgical joint formation whereas figure (d) shows the temperature curve of a strong weld. Curves depicted in green are averaged on two data sets of thermocouples having the same distance from the fusion zone.

Applying equation (4-2) whith the materials properties of 1.4057 (AISI 431) stainless steel [86] the following time shifts result for the relevant distances given in figure 4-6:

d = 350 µm τ = 15.8 ms

d = 400 µm τ = 20.6 ms

d = 450 µm τ = 26.1 ms

d = 500 µm τ = 32.2 ms

The measured data are in the same range as the theoretical results. Nevertheless, there might be a discrepancy of a few milliseconds. This can be accounted to the magnetic field influence on the thermocouples. The measurements were strongly influenced by the magnetic field of the welding pulse that generates large noise. Due to this, an error in the time as well as in the amplitude may result. Thus, only a small number of temperature curves could be evaluated. Note that even some of the evaluated curves show the influence of the magnetic field (see fig. 4-6 a and c). To increase the data quality the signals of thermocouples, that showed a similar distance from the fusion zone, were averaged (see fig 4-6, green curves).

Figure 4-7 shows a plot of the maximum temperature as a function of the distance to the fusion zone (illustrated in blue in fig. 4-5). The closest thermocouple was clamped in between the work pieces and the farthest was placed in a distance of 2.5 mm. It is obvious that the temperature maximum significantly decreases with increasing distance. This is a result of the thermal conduction delay through the materials and thus the measurement gives a temporal resolution of the temperature front. The signal of the thermocouples far away from the fusion zone was not effected by noise but with decreasing distance the noise increased. Therefore, the data obtained from the clamped thermocouple only gives a rough estimation of the temperature profile. Nevertheless, a fit of the temperature distance relation shows good consistency and supports the roughly measured value for the thermocouple clamped into the fusion zone.

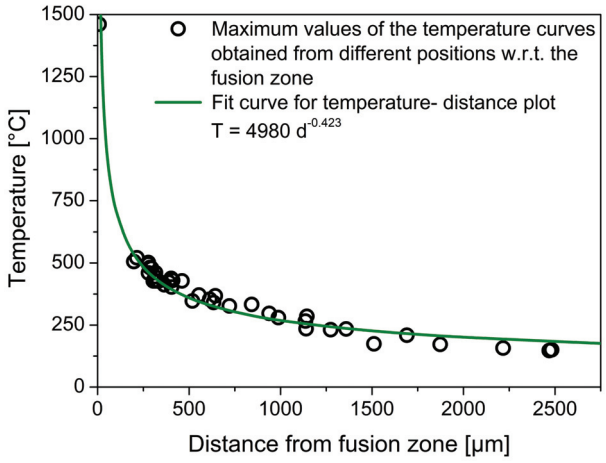

Figure 4-7: Temperature- distance plot obtained from measurements with thermo-couples placed in different distances w.r.t. the fusion zone (compare fig. 4-4, blue dots). A power law fit (green curve) supports the noisy measured maximum temperature for the thermo-couple clamped into the fusion zone.

Concluding the above results a temperature of around 1465 °C is reached inside the fusion zone. Since no melting is observed in the metallographic cross sections, this temperature should be interpreted as the upper limit of the fusion zone temperature. Further, the plot shows that the gradient within the first hundreds of microns from the fusion zone is large. This demonstrates the very local heat input in projection welding (especially with capacitor discharge) mentioned in the introduction (see chapter 2).

4.2.3 Estimation of diffusion influence on joint formation

To estimate the role of diffusion, the diffusion widths for the main alloying elements Fe, Ni and Cr were calculated based on the temperature measurements of the previous chapter. Diffusivity coefficients of Fe in α-Fe and γ-Fe were taken from *Buffington et al.* [134], for Cr in α-Fe and γ-Fe from *Bowen et al.* [140] and for Ni in α-Fe and γ-Fe from *Hirano et al.* [136]. The diffusion width w_{diff} is calculated through

$$w_{diff} = \sqrt{D(T) \cdot t} \qquad (4\text{-}3)$$

where D is the diffusion coefficient and t is the time [142]. Table 4-1 shows the data used for the calculations.

Table 4-1: Overview of the diffusion coefficients for volume diffusion used for the estimation of diffusion width within the example process. The magnetic phase transition from ferromagnetic (f) and paramagnetic (p) α-Fe is taken into account for Ni in and Cr diffusion. The values for the activation energy are given in J/ mol.

Material	*D* [cm²/ s]	Temperature [°C]	Reference
Fe in α-Fe (f)	2.0 exp(-60000 J/ RT)	700 - 750	[134]
Fe in α-Fe (p)	1.9 exp(-57200 J/ RT)	790 - 910	[134]
Fe in γ-Fe	0.18 exp(-64500 J/ RT)	910 - 1436	[134]
Cr in α-Fe	8.52 exp(-59900 J/RT)	797 – 877	[135]
Cr in γ-Fe	10.8 exp(-69700 J/RT)	960 – 1356	[135]
Ni in α-Fe (f)	1.4 exp(-58700 J/RT)	600 – 680	[136]
Ni in α-Fe (p)	1.3 exp(-56000 J/RT)	810 - 900	[136]
Ni in γ-Fe	0.77 exp(-69700 J/RT)	930 – 1050	[136]

For a process time of 20 ms and a cooling time of 130 ms (as shown in fig. 4-6) the calculations result in a width of 2.3 nm for Fe, 2.4 nm Ni and 4.6 nm for Cr. These results show that the bulk diffusion during the process is very small. Further, they coincide with the observations made by the EDX analysis performed in chapter 4.2.1. Since the used EDX is not able to detect concentration gradients on the nm scale, no change in the composition at the interface was detected (see fig. 4-3).

4.3 Methodology for joint formation studies

In the following sections, a systematic approach is given to derive a hypothesis of joint formation in solid state welding and particular in projection welding.

Contrary to the temperature, the stresses and the degree of plastic deformation as well as the contact pressure cannot be measured. Their estimation is only possible by using numerical FEM simulations like already performed for the estimation of significant process parameters in Chapter 3. Hence, a combination of measurements and FEM simulations seems to be expedient for a detailed observation of joint formation and finally the ability of predicting the joint quality from the outputs of FEM process simulation.

The examination of joint formation via experiments is only possible when the influencing parameters can be separated and varied independently. Since this is not

given in projection welding a model setup needs to be designed that provides a clear insight but allows the variation of all important process parameters. Based on the previous literature study the main influencing parameters are the temperature (-profile), pressure and interfacial shearing (see fig. 4-8). The electrical field plays a minor role for joint formation, since it is only the heat source of the process.

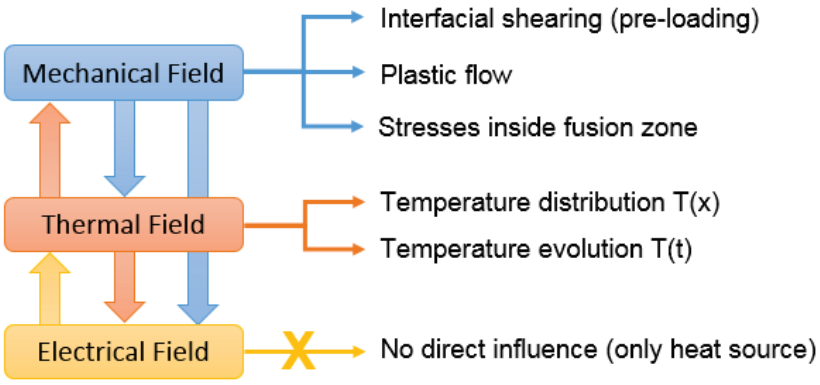

Figure 4-8: Identified influencing parameters on the joint formation in SSW/ PW arising from the mechanical, thermal and electrical field.

For the separate observation and variation of these quantities (given in figure 4-8), the following requirements need to be fulfilled by a clean model experiment

- Decoupling of the heat input from the electrical current since the transient changing constriction resistance of any sample geometry would affect the welding result
- Precise temperature adjustment, control and measurement
- Homogeneous contact pressure and temperature distribution
- Precise adjustment, control and measurement of the applied force/ contact pressure
- Possibility of interfacial shearing to examine the effect of a cold pre-deformed surface condition
- Identification of the surface condition to ensure comparability of the experimental results

As an alternative heat source, which produces high a temperature quickly, only inductive heating seems to be feasible. The use of a furnace would result in heating times of minutes to hours to obtain high temperatures up to 1400 °C. Although inductive

heating is the fastest alternative commercially available, the heating time to 1400 °C (10 to 30 s) is still longer than expected in projection welding (capacitor: 10 to 30 ms; inverter 100 to 300 ms) but has to be accepted as a compromise. Nevertheless, the heating duration may become only relevant when long-range diffusion occurs. As long as the time can be kept below several minutes significant diffusion welding is not expected to occur. Further, it needs to be ensured that the temperature of the fusion zone is homogenous, which can be achieved by a suitable sample geometry. For a precise temperature measurement and control, a pyrometer can be utilized.

The requirement of homogeneous temperature- and pressure distributions at the interface can only be fulfilled for simple geometries with plain contact surfaces. E.g. for stacked cylinders like those used for the electrical contact resistance measurements. The contact surface is nearly constant and hence the contact pressure only depends on the normal force. The latter one can be controlled by a compression testing device. Further, the penetration depth of the magnetic field limits the volume that can be heated by induction. Samples with small volume are therefore favourable. Here again a hollow cylinder shape is advantageous. To achieve cold pre-deformation under the mentioned prerequisites, a tangential movement of sample halves to each other may result in shearing of the interfaces similar as in the pre-pressing step of projection welding. Figure 4-9 shows an overview of the developed experiment design.

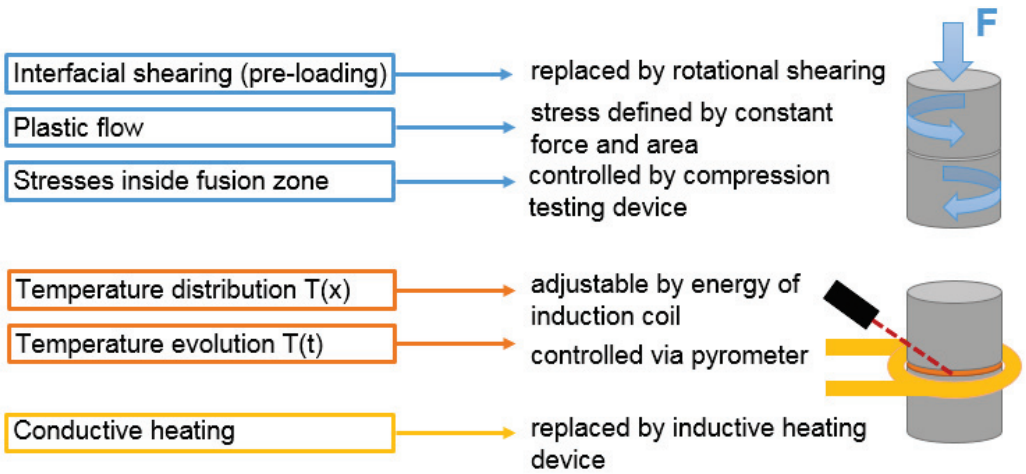

Figure 4-9 Illustration of the transfer of the identified influencing parameters to the model experimental setup.

A detailed design of the sample geometry is possible via FEM simulations, with special focus on the contact pressure distribution under high loads above σ_y. The methodology is described in the following chapter.

4.3.1 FEM simulations for design of a model experimental setup

In focus of the following criterions, numerical simulations were performed to design a suitable sample geometry:

- Homogeneous pressure distribution inside the contact interface
- Geometrical stability of the sample, especially at mechanical loads above σ_y
- Size of the contact surface chosen to reach σ_t of the weaker material (since $R_{cont,el}$ measurements showed that the weaker material dominates the mechanical performance of the interface)
- Sample volume at the interface needs to be small enough for homogeneous inductive heating

The final sample design is a cylindric geometry of 20 mm in diameter and a height of 40 mm. A bore of 15 mm diameter and a depth of 10 mm forms the fusion zone area (see fig. 4-10). Due to the small materials volume in this area, a homogeneous inductive heating of the fusion zone is expected. The samples were stabilized by a dowel pin inserted into a centric bore along the sample axis to prevent tilting of the sample while application of the torque. Figure 4-10 shows the final sample design.

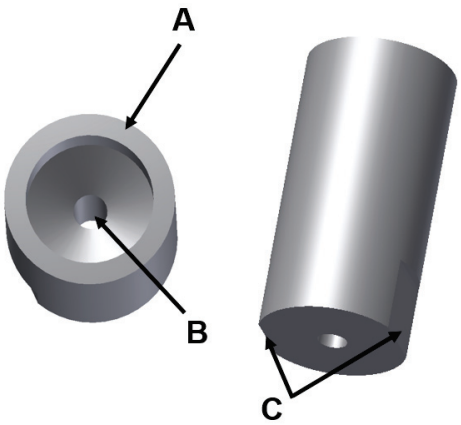

Figure 4-10: Final sample design (top view, left; bottom view, right) for the experiments on joint formation. An annular surface (A) forms the contact area and the small materials volume below enables homogeneous inductive heating. Further the samples exhibit a centric bore for the dowel pin (B) and surfaces for the fixation (C).

As already mentioned before, the sample design was inspired by the $R_{cont,el}$ measurements. Thus, the numerical model of chapter 3.2.2 was utilized again, but for different samples inserted between the punches. Figure 4-11 shows the simulation model (a), as well as the simulation results (b, c, d). These show that to prevent the sample from collapsing (and hence the occurrence of an inhomogeneous contact pressure distribution) under high loads and temperature the deformation distance should be limited (see fig 4-11 c).

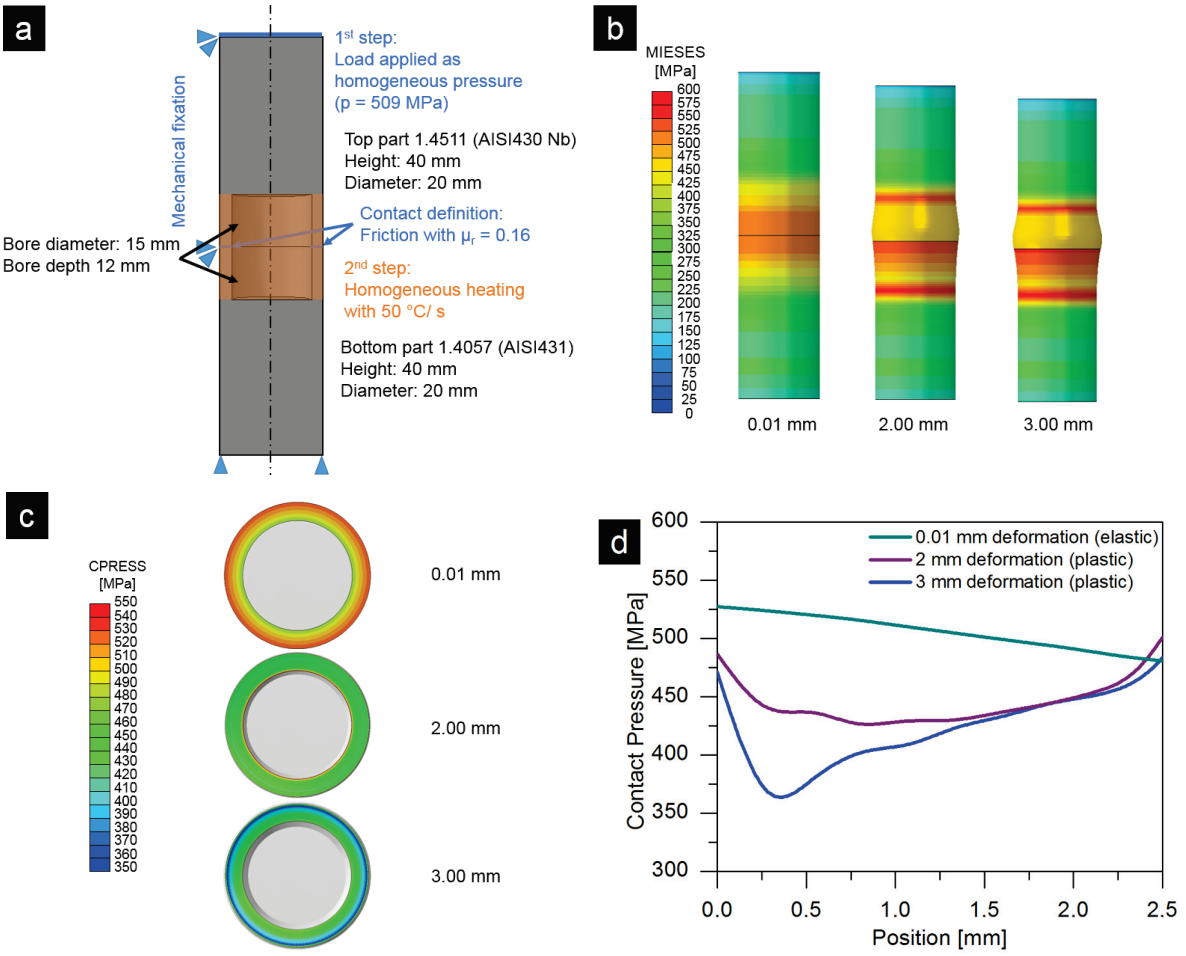

Figure 4-11: Definition of the FEM model for estimation of contact pressure homogeneity of the sample design at elevated temperature (a). Simulation results for different deformations (b; elastic deformation (left) and plastic deformations (mid and right)). The distribution of the contact pressure (CPRESS) for the different deformations is depicted in (c) and the radial pressure distribution at the interface is given in (d). Note that for illustration reasons the induction coil is not displayed.

A value of 2 mm is acceptable, whereas 3 mm of deformation distance lead to severe inhomogeneities of the contact pressure (CPRESS). Preliminary experiments showed that due to the inertia of the compression-testing device at high mechanical loads a deformation distance of less than 1 mm cannot be realized.

To apply torque for the interfacial shearing, the simple punches used in the $R_{cont,el}$ measurements were replaced by a fixation for the upper sample and a punch mounted onto a ball bearing to fix and rotate the lower sample. Further, a contact resistance measurement was included to quantify the surface quality and validate the measurements performed in chapter 3 with an additional geometry.

Concluding the features discussed above, the functions of the final test setup (see fig. 4-12) are

- Controlled force application via punches (3)
- Controlled heating of the interface by inductive heating (6)
    - Adjustable maximum temperature up to 1300 °C
    - Adjustable temperature profile (holding time and heating rate)
- Possibility of applying torque for interfacial shearing of the samples (4)
- Contact resistance measurement for quantification of the interface (5)

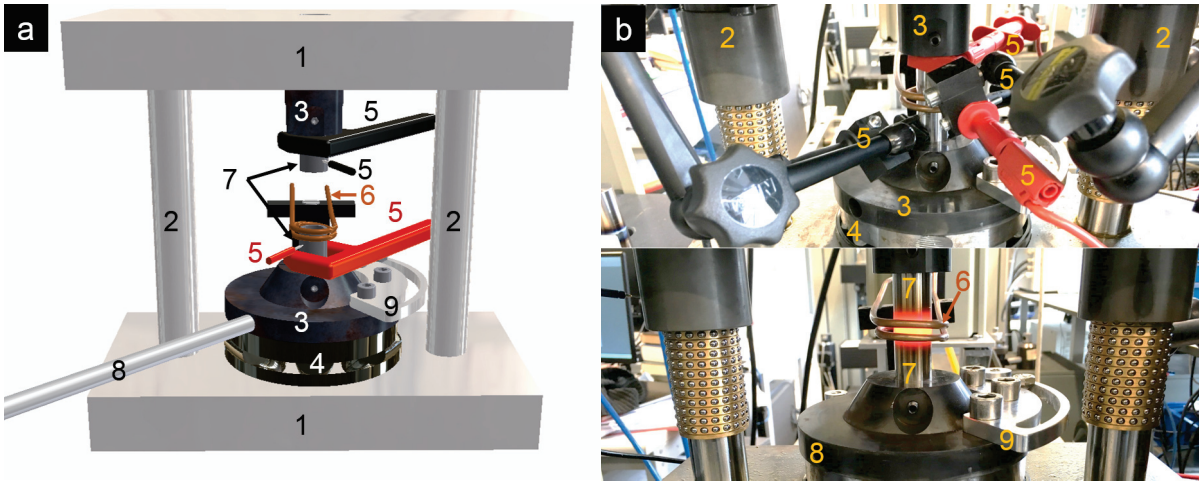

Figure 4-12: Experimental setup for observation of temperature-, pressure- and pre-deformation-dependent joint formation (a). The setup consists of a guide element frame (1 and 2), sample fixations (3), a bearing to carry the lower punch while torsional movement is applied (4), a four point measurement for $R_{cont,el}$ tracking (5), an induction coil for heating of the fusion zone (6), samples (7), a rod to apply the torsional force (8) and a gauge to measure and fix the torsion angle (9). Detailed photographs (b) show the setup with measurement equipment for $R_{cont,el}$ measurements (b; top) and while inductive heating (b; bottom).

4.3.2 Experimental approach

For the examination of the single parameters' influence on solid-state joint formation the following experiments were performed

- Variation of the normal force (apparent contact pressure) for fixed value of temperature
- Variation of the temperature for a fixed normal force
- Variation of the holding time of temperature
- Repeat of the above experiments including a shearing of the interface

For all experiments the evolution of $R_{cont,el}$ was recorded during the cold pre-loading and if applicable, before and after shearing of the interface. Figure 4-13 shows the principle experimental procedure for force F, temperature T as well as the distance s, which can be described as follows. First, the mechanical load is applied and held at a specified level (in this step the shearing of the interface is performed for some experiments). Second, the inductive heating starts accompanied by the plastic flow of

the material due to the mechanical load and the elevated temperature. The plastic flow is limited to a distance of 2 mm to keep the sample dimensions stable.

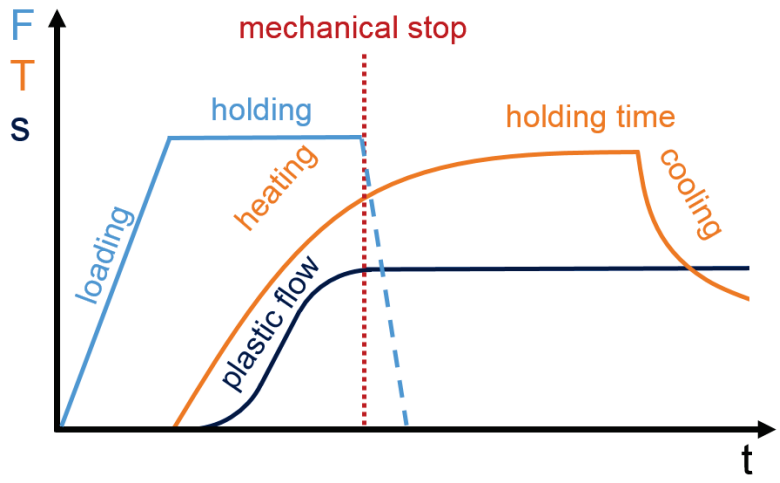

Figure 4-13 Illustration of the experiment consisting of a cold pre-loading phase, a plastic flow phase at rising temperature, a high temperature phase and a cooling phase.

Due to the mechanical stop, the force decreases while the temperature steadily increases. In the third step, the temperature reaches the specified level (and is kept constant, if needed). Note that since there is a force reduction due to the mechanical stopper, the high temperature phase (specified maximum temperature) is not necessarily occurring simultaneously with the applied load. Thus, cooling in the fourth step, takes place without a mechanical loading of the samples and for a fixed deformation distance of 2 mm. With respect to the joint formation, the experiment is divided into two stages. First, the plastic flow at elevated temperature that ends with the mechanical stop and second, the forceless heating. In the following, for simplification, the process is always discussed based on these two stages. Figure 4-14 shows a schematic sketch of the measurement/ control procedure for the different steps.

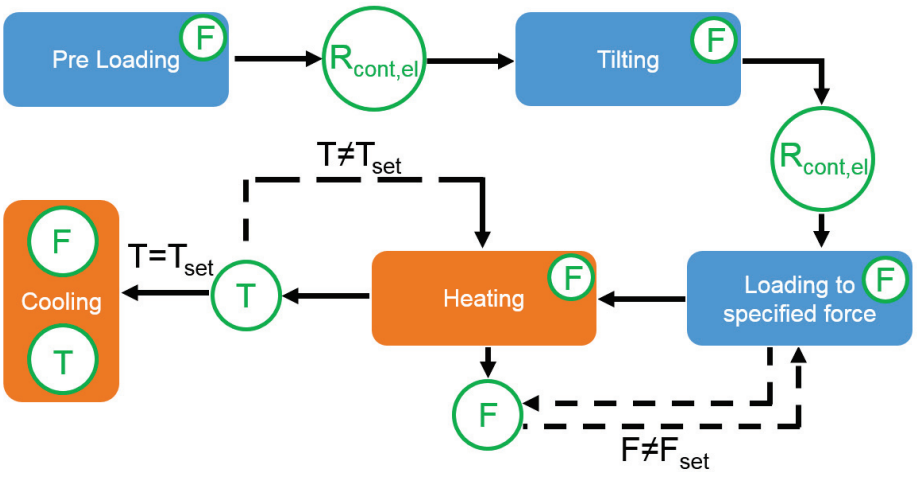

Figure 4-14 Schematic diagram of the experiment and measured data (green). Electrical contact resistance R_{cont} is measured before and after the pre-loading and after the rotation of the punches. The force *F* is kept constant for each force plateau and measured throughout the whole experiment. The temperature *T* in the vicinity of the interface is controlled and measured during heating and measured during cooling of the sample.

For different temperatures, the holding time was varied to ensure comparability of the results. This means that with increasing temperature the holding time was shortened, so that the total time was not changed when changing the temperature plateau (see fig. 4-15).

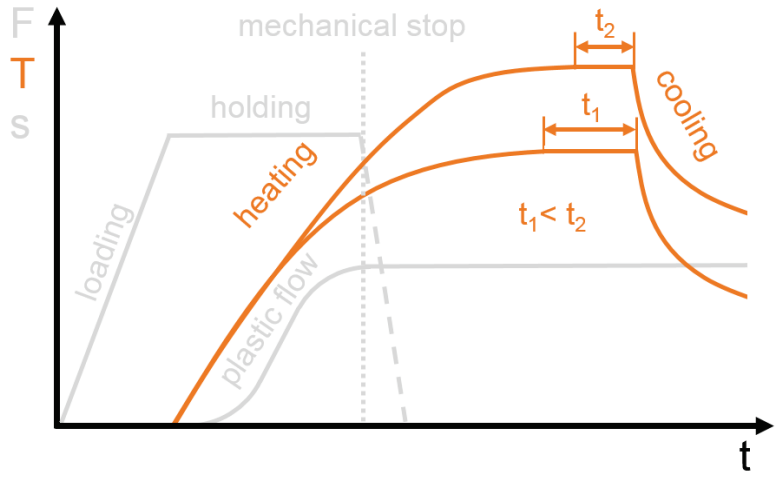

Figure 4-15:
Adjustments in the plateaus holding time when changing the temperature to ensure comparability of the results.

Additionally the holding time was reduced to 0 s to see whether there is an influence on the joint strength or not. Using the above procedure the parameters were varied according to table 4-2.

Table 4-2: Parameter matrix showing temperature- pressure combinations studied in the experiments. The holding times for each temperature- pressure- combination are listed in the lower part of the table. If different holding times were used, a semicolon separates them. Experiments including torsional movement are marked with an asterisk.

		Apparent Contact Pressure				
		72 MPa	174 MPa	258 MPa	345 MPa	509 MPa
Temperature	900 °C	-	x*	x*	-	x*
	1000 °C	x*	x*	x*	x*	x*
	1100 °C	x*	x*	x*	x*	x*
	1200 °C	x*	x*	x*	x*	x*
	1300 °C	x*	x*	x*	x*	x*

Holding Times [s] for each pressure and temperature combination

		Apparent Contact Pressure				
		72 MPa	174 MPa	258 MPa	345 MPa	509 MPa
Temperature	900 °C	-	0; 30.9	0; 30.9	-	0; 30.9
	1000 °C	0; 24.7	0; 24.7	0; 24.7	0; 24.7	0; 24.7
	1100 °C	0; 19.5	0; 19.5	0; 19.5	0; 19.5	0; 19.5
	1200 °C	0; 15	0; 15	0; 15	0; 15	0; 15
	1300 °C	0; 9.3	0; 1; 3.1; 9.3	0; 9.3	0; 9.3	0; 9.3

4.3.3 Preliminary experiments

Preliminary tests were performed to ensure that the temperature measured by the pyrometer really represents the temperature in the interface. The aim was to identify a possible temperature gradient inside the interface (tangential and radial) and to determine the accuracy of the pyrometer. For this, type K thermocouples were welded onto the sample surface, at the inside and outside as depicted in figure 4-16 a. With this setup the temperature measured by the pyrometer was tracked for different maximum temperatures.The results show that, beside the magnetic field noise, there is no offset between the outer and inner thermocouple. Further, there is a small offset of around 25 °C between the thermocouples and the pyrometer at the set maximum temperature. Since cooling occurs without the influence of the magnetic field the curves match in the cooling phase. This indicates that the temperature measured by the pyrometer represents the interface temperature very well.

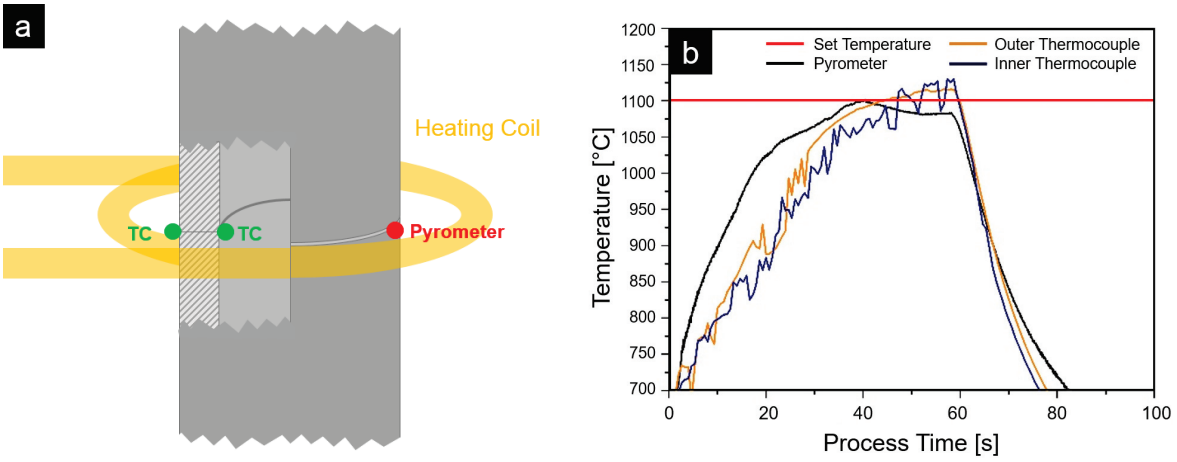

Figure 4-16 Positions of thermocouples for measurement of temperature radial homogeneity (a) and resulting temperature-time-curves for e.g. 1100 °C (b). Note that due to the measurement principle the pyrometer is only able to reliably detect temperatures above 550 °C. Further the magnetic field of the inductor generates noise in the thermocouples signals as can be seen in (b).

Adittionally, a decrease in the heating rate is visible for temperatures above 750 °C. This can be accounted to the ferromagnetic-paramagnetic transition at the *Curie Temperature* T_{Curie} of iron (T_{Curie} = 771 °C [143]). The tests were repeated with a radial alignment of the thermocouples (see fig. 4-17).

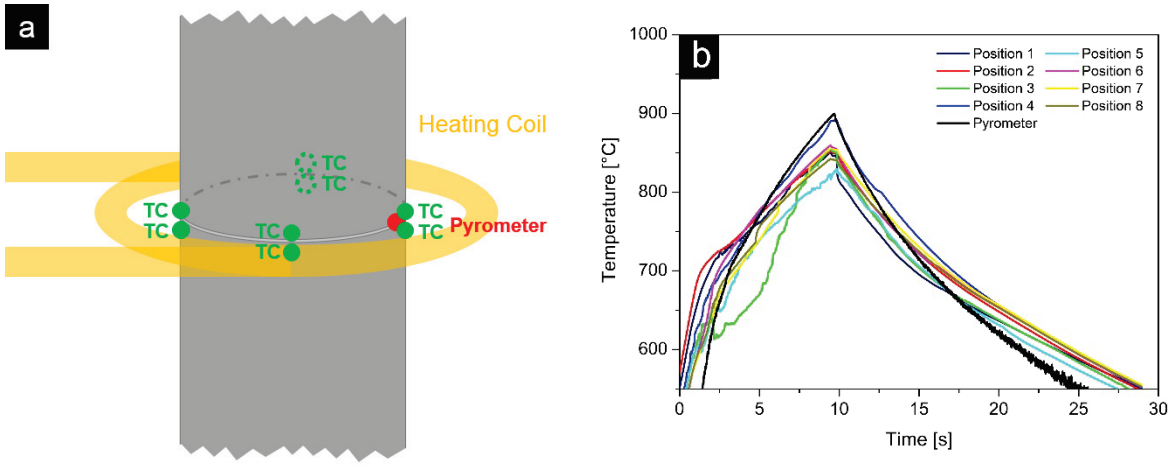

Figure 4-17: Measurement of the angular temperature distribution with 4 thermocouples at each sample (indicated in green) in an angle of 90°. The pyrometer was adjusted to measure in between two thermocouples as indicated by the red dot.

In addition, the gradient in normal direction of the interface was determined, to see whether the temperature decreases simultaneously within both materials (see fig. 4-18). Again, the results show only a small discrepancy between the thermocouples and the pyrometer of around 35 °C (see fig. 4-18 b). The measurements in normal direction show a continuous temperature decrease with increasing distance from the interface of the samples (see fig. 4-18 b) or the heating coil, respectively. Further, there is no jump in the temperature signal when crossing the samples interface. This indicates that the thermal contact is good enough to provide sufficient heat exchange between the samples. Concluding the exploratory experiments, the model setup features

- Homogeneous heating of the interface in
  - radial direction
  - angular direction
- The temperature measured by the pyrometer represents the interface temperature within an accuracy of +/- 30 K
- Homogeneity of contact pressure within deviation of 50 MPa can be achieved

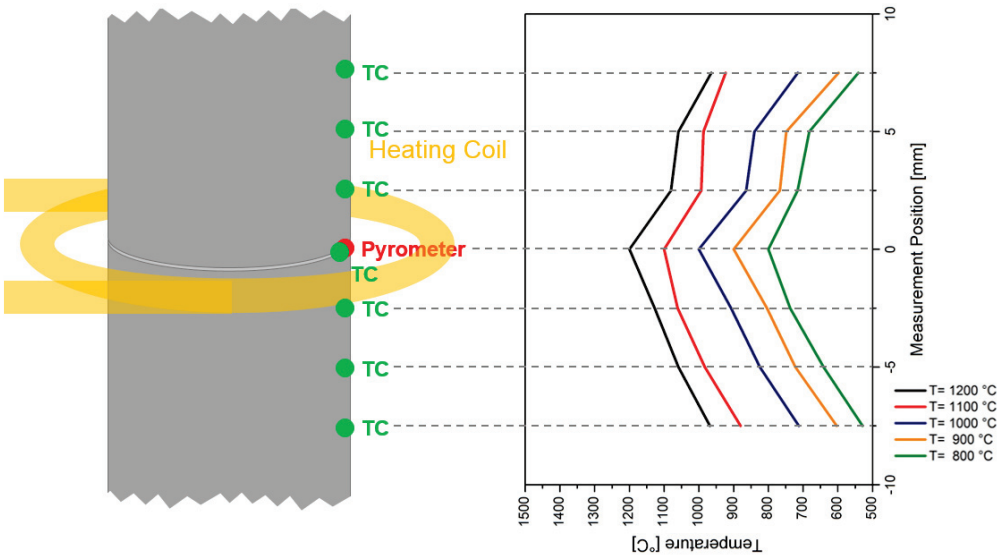

Figure 4-18 Temperature gradient along the sample length for different maximum temperatures. The results show that there is no sudden temperature change when crossing the interface.

In addition, the pre-deformation of the interface is enabled by shearing. To estimate a necessary shearing angle, the work of *Crinon and Evans* [95] was considered, who

examined the influence of interfacial shearing on $R_{cont,el}$ for aluminum samples. Their results show that already for low shearing angles between 0.2° and 3.0° $R_{cont,el}$ drops by six orders of magnitude which is explained by the rupture of the oxide layer. This phenomenon is linked to the plastic deformation of asperities and thus enables an intimate contact between the sample surfaces which is also important for SSW (see ch. 4.1.1). Since the strength of stainless steel is larger than the one of aluminum the shearing angle was set to 10° to ensure proper pre-deformation of the interface. As already mentioned in chapter 4.3.1 a $R_{cont,el}$ measurement was used to quantify this change of the contact morphology.

4.4 Testing methods

To assess the quality of the welded samples metallographic cross sections were prepared (see ch. 4.4.1). Further, the mechanical strength determined via mechanical tensile testing as described in chapter 4.4.2.

4.4.1 Metallographic examination

The cross sections for analytics of the sample material were prepared as described in chapter 4.2.1. Since this procedure could only be applied to sufficient welded samples (fracture remote from the initial interface), the fracture surface of the inadequate samples was also analysed via light microscopy and scanning electron microscopy.

4.4.2 Mechanical tensile testing

After welding, the joint strength of the samples was measured by tensile testing (Zwick 1484 with 250 kN load cell). The test speed was 30 mm/ min and the pre-load was 100 N. The tests were performed force controlled until fracture of the samples. From the stress-strain curve, the apparent tensile strength was calculated based on the apparent contact area and the maximum force.

4.5 Results and discussion

In the following the test results are described and discussed. In chapter 4.5.1 the electrical contact resistances are compared to the values measured in chapter 3.2.3 to assess the general validity of the measurements. The results of the mechanical tensile testing are presented in chapter 4.5.2. Chapter 4.5.3 and 4.5.5 focus on the parameters, which were systematically varied in the welding experiments, namely the joining time, the joining pressure, the joining temperature and the interfacial shearing. Since oxidation at high temperatures can influence the joint formation, this topic is discussed in chapter 4.5.6 in context of the experimental results. Lastly, the influence of diffusion on the joint formation is discussed. This topic is addressed in chapter 4.5.7.

4.5.1 Electrical contact resistance as measure for surface condition

During the joint formation experiments $R_{cont,el}$ was measured for the different mechanical loads applied to the samples. The values decrease with increasing contact pressure (see fig. 4-19 a). A comparison with the values of the contact resistance study of chapter 3.2 shows a good coincidence. Again, a large scattering of the data points can be observed for the low contact pressures whereas for higher loads scattering reduces significantly. The contact area as well as the contact conditions of the joint formation samples differ from the ones described in chapter 3.2, but the measurements lead to the same results (comparison of electrical contact resistance in Ω·mm²). This shows that the results of chapter 3.2 are of general validity and are independent on the measurement setup. When shearing is applied to the interface at constant normal load $R_{cont,el}$ suddenly drops to zero (see fig. 4-19 b).

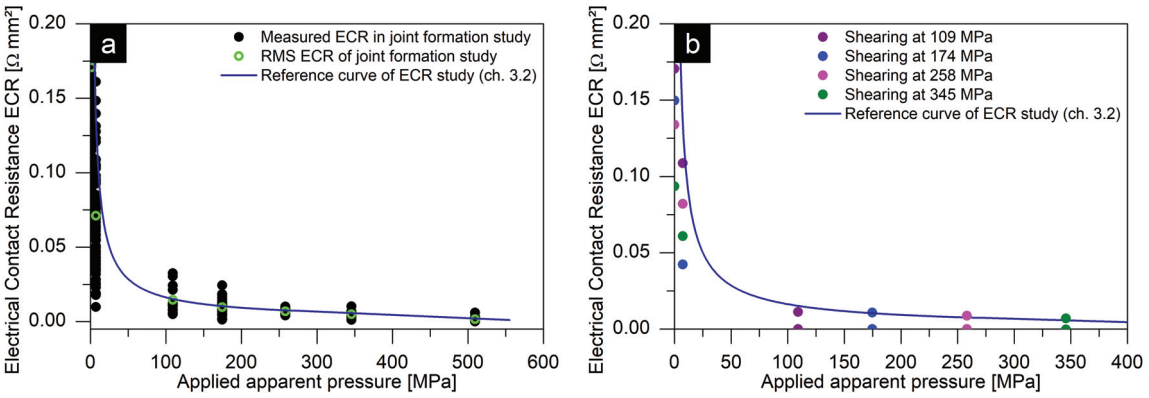

Figure 4-19 Measured $R_{cont,el}$ versus applied pressure during the joint formation experiments and comparison with the results of the $R_{cont,el}$ study of chapter 3.2 (a). Influence of interfacial shearing on the $R_{cont,el}$ (b). The $R_{cont,el}$ drops suddenly when shearing is applied. This observation is repeatable for different contact pressures. Figures including the error bars are given in appendix B-5.

This observation was already reported by *Crinon and Evans* [95] for aluminum samples and their explaination is the plastic deformation of surface asperities and the break-off of oxides. Hence, an ideal material contact is achieved and the electrical current is no longer hindered to pass the interface. Hence, these results also proof the hypothesis that the $R_{cont,el}$ is not relevant for projection welding.

4.5.2 Force distance curves from tensile testing

The tensile testing shows different mechanical behaviour for the different welding parameters (see fig. 4-20). While some samples already fracture below 20 kN others reach a maximum force of 78 kN.

A difference in the plastic behaviour is also obvious. The samples that fracture at lower forces exhibit a brittle fracture (see. fig 4-20, (b) red and blue curve; (c) pink, blue, green and turquoise curve) whereas the high strength samples show a ductile behaviour until fracture occurs (see. fig. 4-20, d). This difference in mechanical behaviour is also visible at macroscopic examination of the samples (see fig. 4-21 a). All samples that showed a brittle behaviour fractured at the fusion zone. An SEM image of the fracture surface of such samples proves the brittle fracture (see fig. 4-21 b).

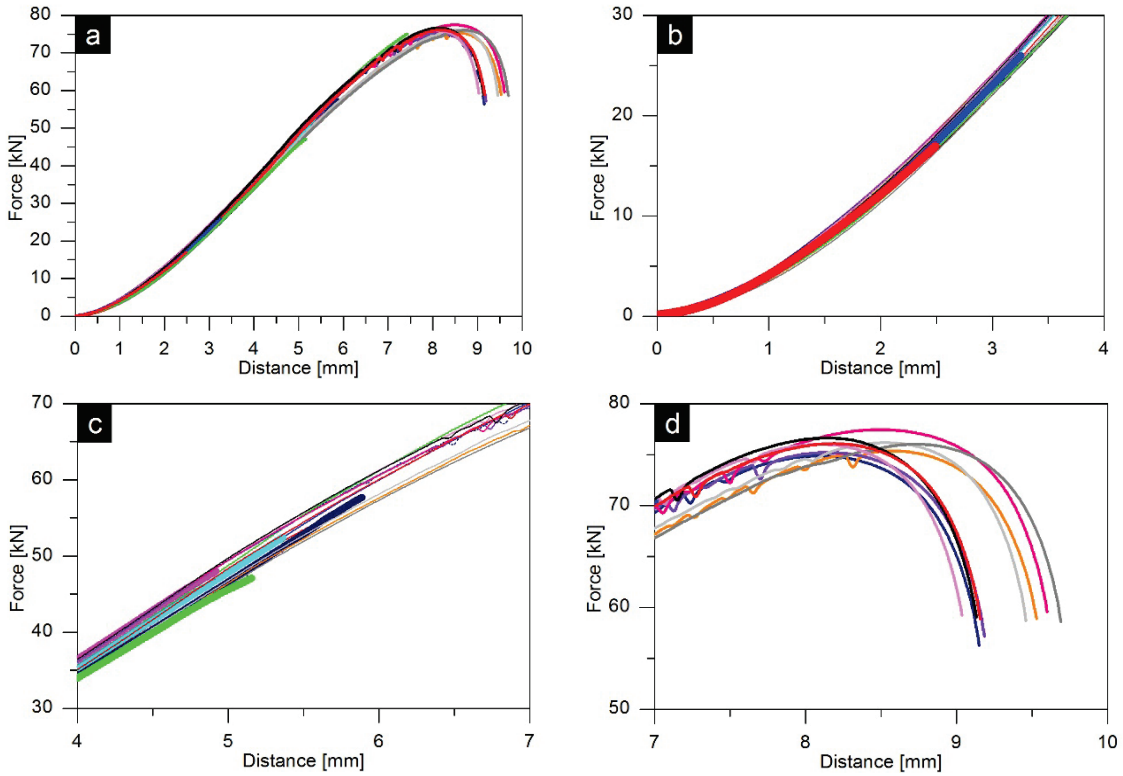

Figure 4-20: Results of the tensile tests depicted for selected representative samples (a). Detail of the lower force regime (b), medium force regime (c) and high force regime (d) with bold highlighted curves to indicate the different mechanical characteristics.

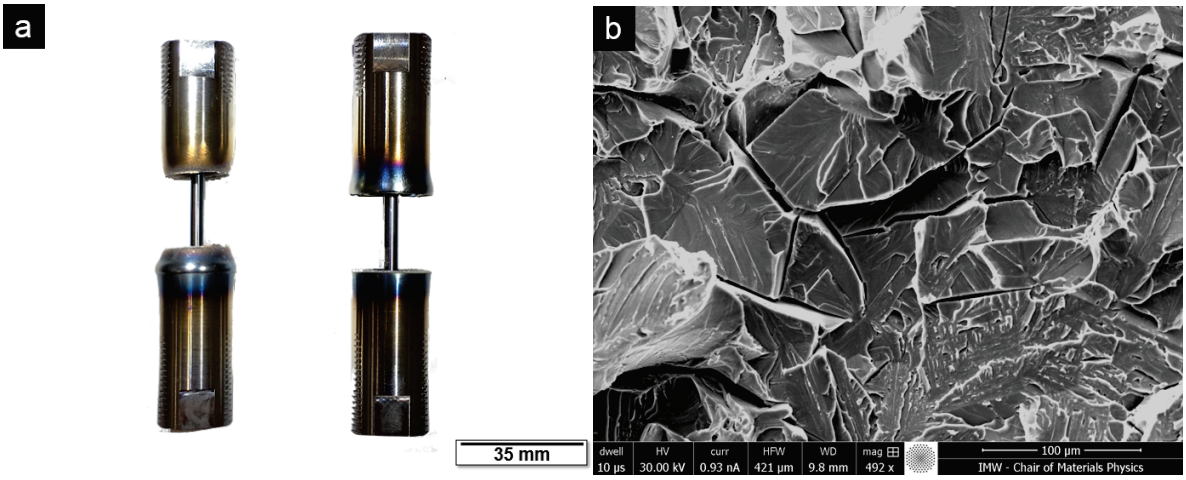

Figure 4-21: Comparison of macroscopic difference between a sample with ductile fracture in the weaker base material (a, left) and brittle fracture through fusion zone (a, right). An SEM image of the fracture surface of a brittle fracture is given in (b).

In contrast, the ductile samples fractured remote from the fusion zone in the weaker 1.4511 (AISI 430 Nb) base material. Hence, the ductile characteristics mainly depends

on the mechanical performance of the base material, whereas the brittle characteristics mainly depends on the mechanical behaviour of the fusion zone. In the latter case a sticking of the single grains to the surface of the other material results in a brittle fracture due to hindered strain in normal direction.

4.5.3 Influence of joint formation duration

To quantify the influence of the joint formation duration, the holding time was varied for constant contact pressure (step one) and various plateau temperatures (step two). Figure 4-21 shows the results for a contact pressure of 172 MPa and temperatures from 1100 °C to 1300 °C, including the influence of interfacial shearing.
It can clearly be observed that for 1100 °C (see fig 4-22 a) longer holding times negatively affect the joint strength, independent of interfacial shearing. For 1200 °C and 1300 °C (see fig. 4-22 b, c) no dependency of the joint strength on the holding time can be observed. These results indicate that 1100 °C seems to be a critical temperature for the joint formation (for 172 MPa in the first step). At elevated temperatures, oxidation of the surfaces occurs, but also diffusion is enabled. A possible explanation is that oxidation and diffusion are equally balanced at 1100 °C, whereas for higher temperatures diffusion dominates the process. Thus, a temporal influence of step two on the joint strength seems to be negligible for temperatures of 1200 °C and above, but not for lower temperatures. The influence of oxidation on the joint formation was also examined in this work and is discussed in detail in chapter 4.5.6.

For increasing pressure, mechanical flow of the material starts earlier and the temperature present when the mechanical stopper is reached, decreases (see fig. 4-23). Hence, the interface is closed at different temperatures T_{stop} in step one and heated up to the final plateau temperature in step two. For the further discussion on influencing parameters on joint formation, this fact needs to be kept in mind.

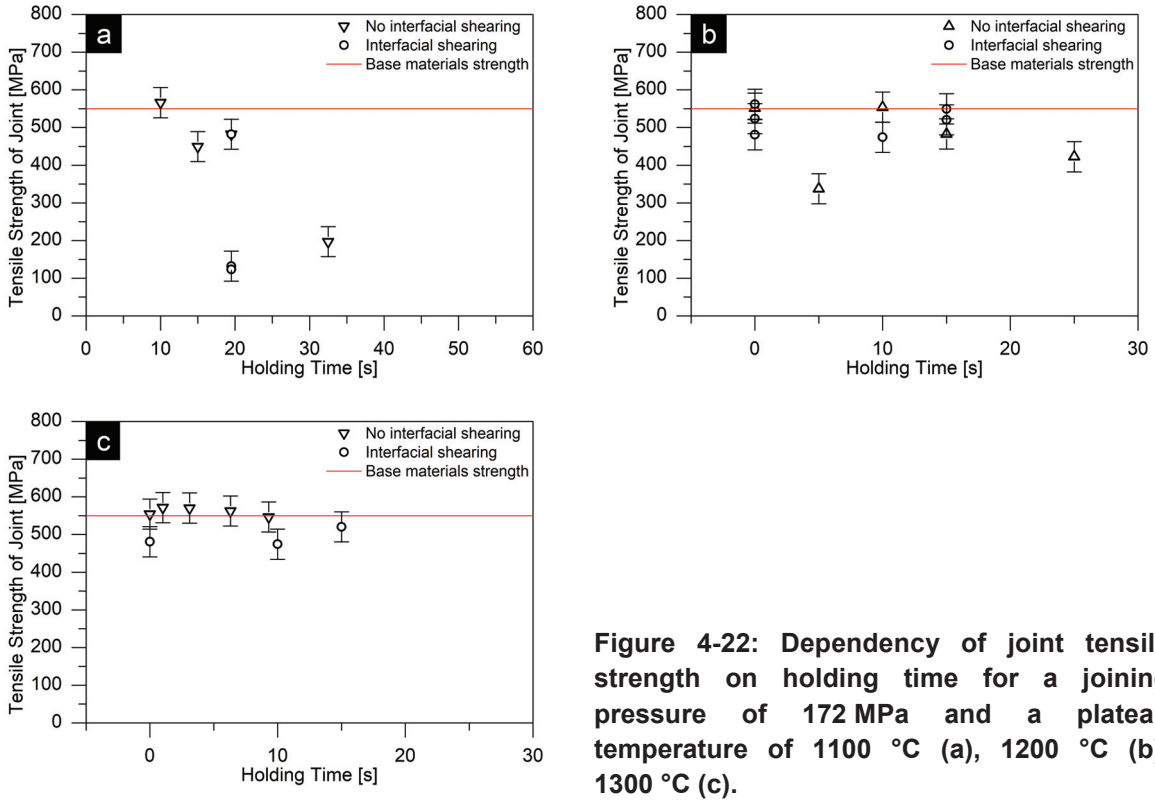

Figure 4-22: Dependency of joint tensile strength on holding time for a joining pressure of 172 MPa and a plateau temperature of 1100 °C (a), 1200 °C (b), 1300 °C (c).

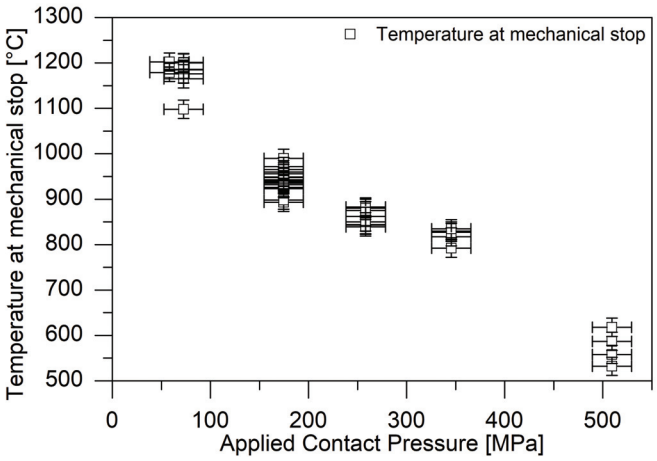

Figure 4-23: Pressure dependency of the temperature when the mechanical stopper is reached in the first step. With increasing contact pressure, this temperature decreases.

4.5.4 Influence of contact pressure and temperature

To analyse the influence of contact pressure in step one and maximum temperature in step two, the joint strength was depicted as a function of temperature for various pressures (see fig. 4.24). The results show that for an increasing contact pressure in

step one, for the same temperature in step two, the joint strength increases monotonously. For a pressure of 72 MPa (see fig. 4-24 a) the joint strength does not reach the strength of the base material, independent of the plateau temperature of step two. The same holds for 900 °C and 1000 °C, independent on the applied pressure.

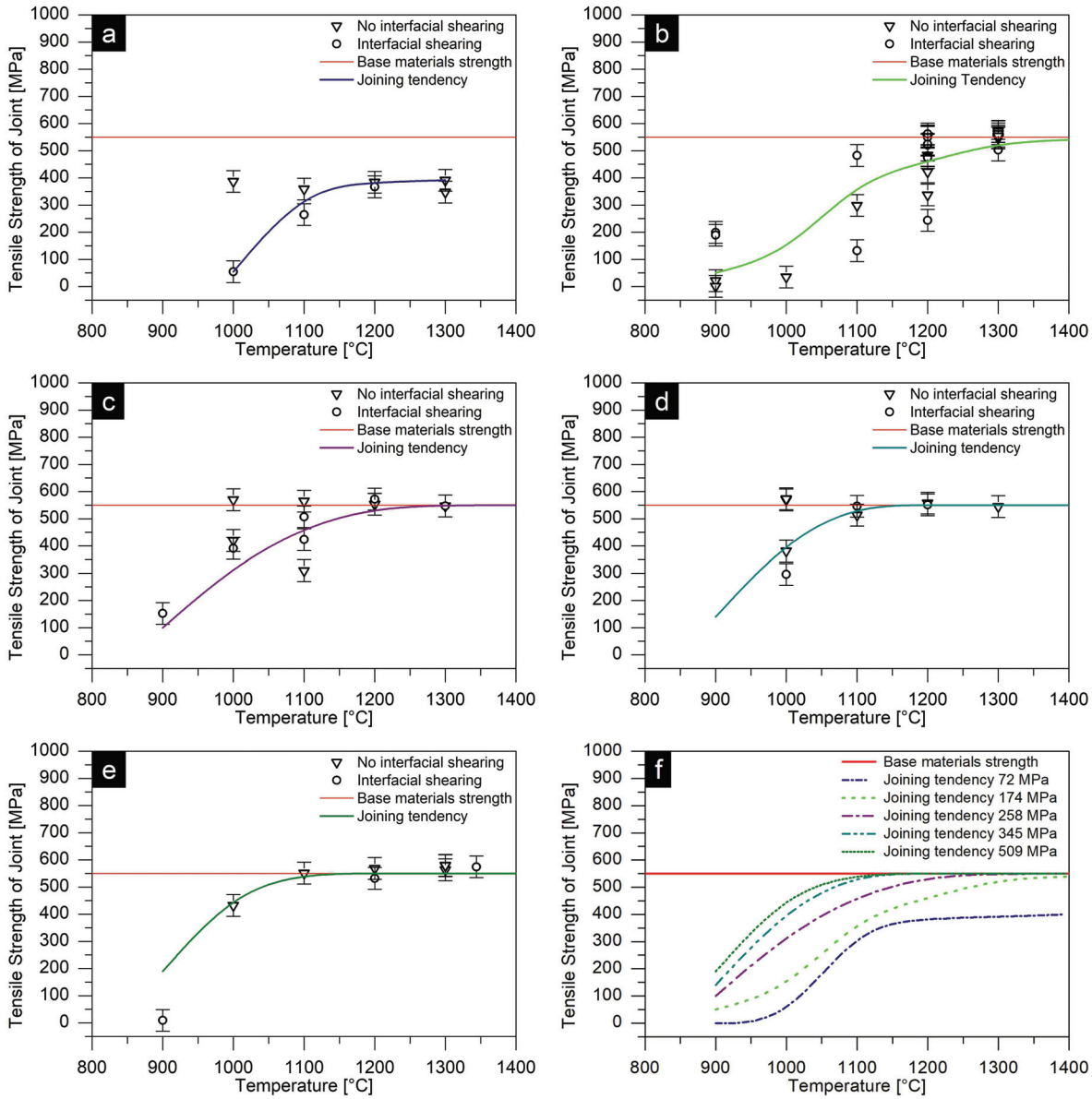

Figure 4-24: Influence of the temperature on the joint strength for different contact pressure; 72 MPa (a), 174 MPa (b), 258 MPa (c), 345 MPa (d), 507 MPa (e), comparison of the different pressures with tendencies (f). Note that the depicted tendencies (solid lines) only indicate the trend for joint formation, but do not represent a fit function.

Again, 1100 °C can be identified as a critical temperature. The values of joint strength scatter over a large range, except for the highest pressure of 507 MPa (see fig. 4-24 e). For 1200 °C and 1300 °C already 258 MPa are sufficient to produce a joint that reaches the strength of the base material. A further increase of the contact pressure does not increase the joint strength any further (see figs 4-24 c, d, e). To illustrate the joining tendency of the materials, coloured curves where inserted. In fig. 4-24 f), these tendencies for different pressures are composed.

Recalling the pressure dependency of the stop temperature (see fig. 4-23), the pressure levels of the first step, shown in figure 4-24, can be replaced by the corresponding temperature (e.g. 72 MPa corresponds to T_{stop} = 1180 °C).

If doing so, it becomes clear that a T_{stop} below 860 °C and T_{hold} above 1100 °C (see fig. 4-25), is sufficient to establish a joint with the strength of the base material. Higher values of T_{stop} are not favourable, since the joint strength decreases to values below the base materials strength.

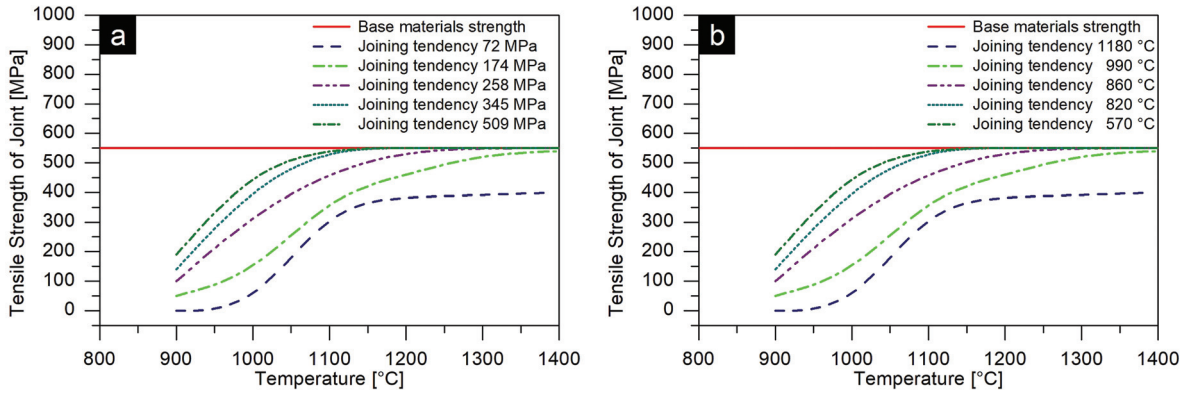

Figure 4-25: Comparison of the joining tendency for the variation of contact pressure (a) and the stop temperature T_{stop} (b). The graph shows that the joint reaches the strength of the base material at lower temperatures, with increasing contact pressure. An increase in the stop temperature T_{stop} leads to lower joint strength. Hence, the joint strength reaches the base materials strength for T_{stop} below 860 °C in the first step, for T_{hold} above 1100 °C in the second step.

4.5.5 Influence of interfacial shearing

To examine the influence of pre-deformation on the welding result, the experiments were conducted with- and without interfacial shearing at otherwise constant conditions (see fig. 4-24, empty circle data points). For low contact pressure and low temperature (see fig. 4-24 a and b) no distinct influence of the shearing on the joint strength is observed. For some samples the pre-deformation lowers the joint strength and vice versa (e.g. fig 4-24 a, 1000 °C and b, 900 °C). With parameters that lead to a successful weld (see fig. 4-24 c, d, e, 1100 °C – 1300 °C) the interfacial shearing does not change the result. For the intermediate range of parameters the improvement of joint strength by pre-deformation is also not clear. For 174 MPa and 258 MPa and temperatures of 1000 °C and 1100 °C the scattering of the data points is large (see fig. 4-24 b and c). This observation could be explained by the transition region between strong bond and insufficient bond. The mentioned parameters are in a region where small disturbances (e.g. unevenness, pressure inhomogenites or impurities) may already lead to an insufficient welding. Further, at lower contact pressure the applied torque may cause a loss of contact between the sample surfaces due to occurrence of a transverse force when the handle is moved manually.

4.5.6 Influence of high temperature Oxidation

When examining the welded samples by optical micrsocopy, it is obvious that severe oxidation occurs at high temperatures (see fig. 4-26 a). Since a correlation between the occurrence of oxides in the fusion zone and a low joint strength was observed, this effect is discussed in the following. For samples that were joined at low contact pressures the joining surface was completely oxidized (see fig. 4-26 a). This effect was not observed for higher pressures, even when the plateau temperatures were higher (e.g. fig. 4-26 b). Reconsidering the T_{stop}-dependency on the contact pressure in the first step (see fig. 4-23), a higher temperature and thus faster oxidation can occur at low contact pressures (high temperatures respectively).

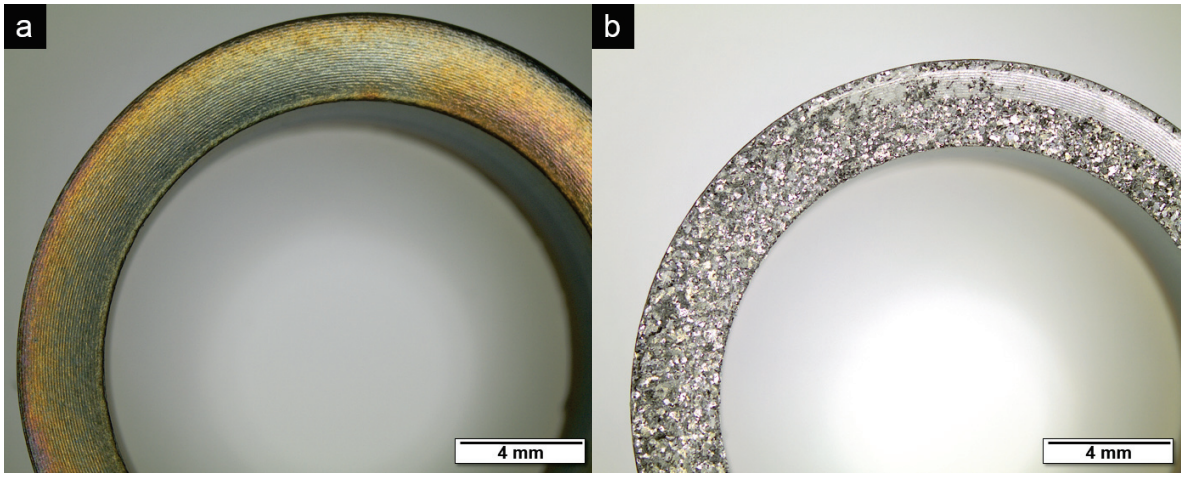

Figure 4-26: Difference between an unsuccessful weld with low pressure (18 MPa) (a) and higher, but still insufficient contact pressure (72 MPa) (b). In the first case, high temperature oxidation can be observed at the whole sample surface. In the latter case, the oxidation can be prevented but bonding does not occur completely. Note that the plateau temperature for (a) was 1100 °C and thus significantly lower than 1300 °C for (b).

A possible explanation of this phenomenon is given by the review on the oxidation of iron and carbon steels by *Chen and Yuen* [144]. Their overview reveals that the oxidation in general follows a parabolic rate law which was proven by different experimental results for various materials [145–148]. They further conclude that the work of further researchers [149–151] coincide in the statement that for temperatures above 850 °C the oxidation rate significantly increases. This observation was explained by a phase-structure change in the steel. Since the ideal T_{stop} identified in the experiments of this work (see fig. 4-23) is below 860 °C, a rapid oxidation of the interfaces before intimate contact is established seems possible above this temperature. This result thus coincides with the general understanding of steel oxidation. Contrarily to the “natural oxide layer” that can be fractured by interfacial shearing (as shown by the results of chapter 3.2, chapter 4.5.1, as well as the results of *Crinon and Evans* [95]), the oxides formed at high temperature cannot be broken off. This effect was examined via experiments where samples were pre-oxidized pressureless at the plateau temperature, cooled down and welded at the same temperature. The results show that, compared to the non-pre-oxidized samples, the joint strength is much lower (see fig. 4-27 a). Further, the pre-oxidized samples could

also not be successfully welded when interfacial shearing was performed after the pre-oxidation (see fig. 4-27 b).

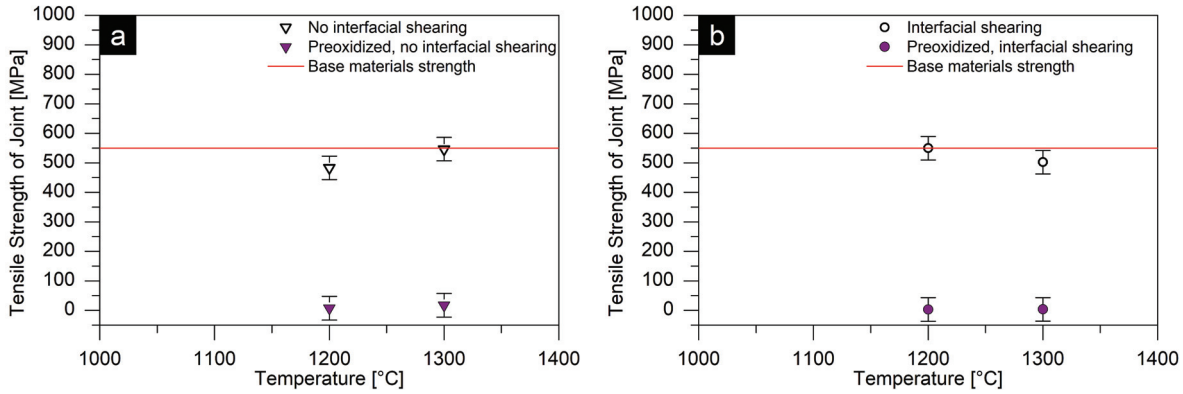

Figure 4-27: Effect of high temperature pre-oxidation for samples without interfacial shearing (a) and with interfacial shearing (b). The samples were oxidized at the same temperature as the joining temperature, cooled down and then joined by the usual procedure. For comparison, the experiments were repeated without the pre-oxidation to show the influence of oxidation on the joint strength.

4.5.7 Estimation of diffusion influence on the joint formation

EDX measurements across the interface were conducted to estimate the influence of bulk diffusion in the joint formation (compare ch. 4.2.1). Further, the diffusion width was calculated as shown in chapter 4.3.2 and the temperature data measured by the pyrometer. Apparently no diffusion seam is visible in the microcraphs of the fusion zone (see fig. 4-28), even for higher magnifications in the SEM (see fig. 4-28 b).
The difference in Ni concentration between the top part 1.4511 (AISI340 Nb) and the bottom part 1.4057 (AISI 431) is visible in the line scan whereas the Nb concentration seems to be constant (see fig. 4-28 d). This can be accounted to the fact that the Nb concentration in both materials is below the detection limit of the EDX. From the concentration profiles, no significant bulk diffusion is visible. The abrupt change of Ni when crossing the interface indicates that there is no diffusion of Ni from the Ni rich 1.4057 (AISI 431) to the Ni poor 1.4511 (AISI 430 Nb) stainless steel. Since the Cr concentration in both steels is nearly equal, no change can be observed in the line scan (see fig. 4-28 c).

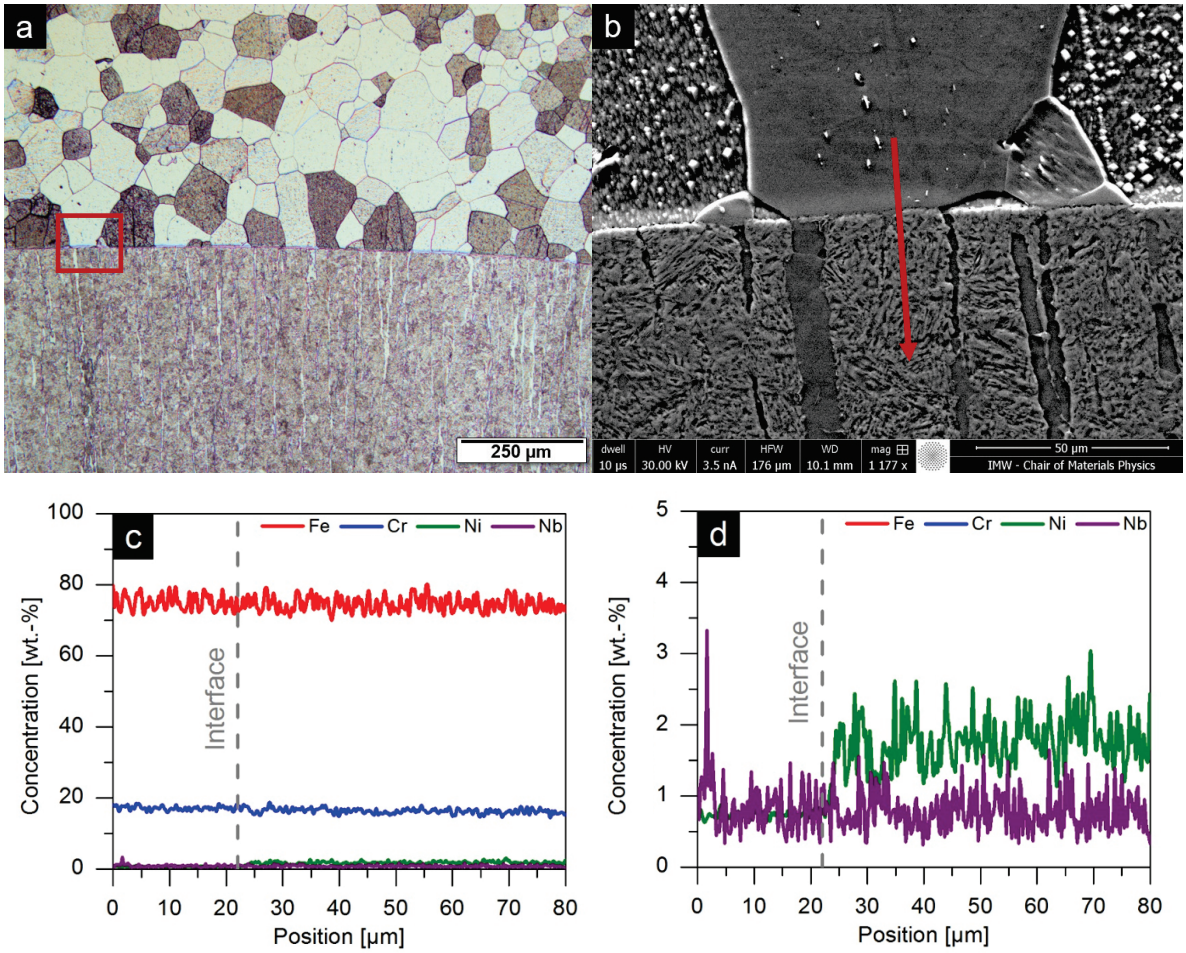

Figure 4-28: Micrograph of the fusion zone for a successful weld (a), SEM image of the marked area with EDX line scan (red arrow) (b), line scan showing the wt.-% concentration of Fe, Cr, Ni and Nb (c) and detailed view of the concentration profile of Ni and Nb (d).

The calculation results on the diffusion width (again utilizing eq. 4-3 and the data given in tab. 4-1) show that Fe diffuses 41.1 µm, Ni 40.1 µm and Cr 120 µm within the time needed to heat the sample up to 1300 °C, hold for 9.3 seconds and cool down to ambient temperature. Since this is in contradiction to the EDX measurements, volume diffusion seems not to occur in the process. Hence, the generation of a strong and defect free interface can be accounted to elimination of pores via surface diffusion.

4.6 Conclusion and comparison of results

Based on the above discussion, the following conclusion can be drawn:

- The role of plastic pre-deformation (interfacial shearing) at room temperature cannot be clarified completely. A large scattering of the joint strength is observed, especially for the critical contact pressure and temperature range (< 258 MPa and < 1200 °C). For samples that are already suffiently joined without plastic pre-deformation, no difference to the ones that were sheared in the cold state.
- The sudden force drop when reaching the mechanical stopper does not affect the joint formation. This is also observed in the example process, where a mechanical stopper was used to understand the fusion zone evolution.
- A strong metallurgical joint can be achieved for temperatures above 1200 °C in ambient atmosphere.
- The contact pressure is only relevant in the first phase where plastic flow at elevated temperature occurs. For initial contact pressures above ½ σ_y (for the weaker 1.4511 (AISI 430 Nb) stainless steel) a strong metallurgical joint can be achieved. For lower contact pressures the interface tends to oxidized and as a consequence the formation of a joint is hindered.
- For joint formation at sufficiently high temperatures (> 1200 °C) the plateau time does not affect the joint formation.
- It is obvious that for a sound weld it is not necessary that pressure maximum and temperature maximum act at the same time, but high temperatures should be avoided until the interfacial pores are closed to prevent oxidation of the interface.
- Recrystallization can be observed in the example welding process (projection welding process with a real welding setup and capacitor bank as an energy source) but not in the model experiment (inductive heating and application of pressure). Thus, it is judged as not necessesary for the joint formation but indicates the severe plastic deformation that occurs in projection welding. Further, the recrystallization shows that re-orientation occurs at the interface.

- Volume diffusion is not observed in both experiments, neither the example process nor the model experiment. Contradictory to diffusion width calculations, EDX measurements show no volume diffusion across the interface, especially for Ni (whose concentration differs in both materials)

In context of the work of other researchers, these observations should further be discussed:

Recently *Harada et al.* [152] examined the joint formation in projection stud welding between steel studs and steel plates, with capacitors as energy source, as a function of the capacitors charging voltage. Apparently, the microstructure of the interface of their welds shows the same features as described in chapter 4.2.1 and chapter 4.5.6. The work pieces are separated by a thin interfacial line but show a high joint strength. Further large plastic deformations are observed near the interface and a change in the grain sized is reported inside the heat-affected zone. To estimate the temperature distribution inside the work pieces *Harada et al.* compared the microstructures of the welds with the ones of the same material heated separately. They found a maximum temperature above 900 °C for sufficient welds and between 727 °C and 900 °C for the transition from insufficient to sufficient. These observations show that in ambient atmosphere at least 900 °C must be reached to form a metallurgical joint between two steel parts. As shown by the temperature measurements in this work (ch. 4.2.2) and the results of the model experiments (ch. 4.5.4) the temperature needs to be much higher than 900 °C. This effect can be accounted to the different metallurgy of the materials, since Harada et al. used steels without Cr or Ni content.

The brittle characteristics of the fracture surface (see fig. 4-21) indicates that the first phase of joint formation (plastic flow and bonding to the other material's surface) has already been completed. Nevertheless, the second phase (high temperature re-arrangement of the interface and pore elimination) has not been completed. Thus the large ferritic grains of the 1.4511 (AISI 430 Nb) are pinned to the surface of the other material but in a way that the interface is not re-arranged to perfect fit. When a mechanical load is applied, the grains therefore fracture brittle and transgranular (see fig. 4-21).

Pongmorakot et al. examined the joint formation of low carbon steel for temperatures up to 650 °C in vaccum [153]. The experimental procedure was different from the one of this work, since in a first step the samples were heated up, followed by a short compression at the specified temperature and finally isothermal holding (with comparable times) and cooling without the application of pressure. As shown by the results of this work, such an experimental approach is not possible in ambient atmosphere due to the high temperature oxidation of the interface. Nevertheless, the same observations were made regarding the timing of compression and isothermal holding, which does not need to be performed simultaneously. Further, *Pongmorakot et al.* reported that when the samples are held at constant temperature after the compression (at elevated temperature) the joint strength increase with holding time could be separated into two regimes. First, the increase of interfacial strength is fast right after high temperature compression is performed and slows down for pressureless isothermal holding [153]. Contradictory to the results of this work, bonding with high strength was only observed after the isothermal holding, which may be a consequence of the low temperature compared to the experiments of chapter 4. Since there is no remark on the used contact pressure, the results cannot be compared regarding this aspect of joint formation.

The observations that no massive bulk diffusion, neither in the example process nor in the model experiment can be observed (see figs. 4-3 and 4-28) coincides with the mechanisms proposed by *Pongmorakot et al*. [153]. Based on the results of molecular dynamics simulations, they state that the compression at elevated temperature leads to a small increase in contact area accompanied by atomic rearrangement and thus an increase in joint strength. Nevertheless, for the isothermal holding at the temperatures examined they suggest “long range diffusion” and subsequent increase of the contact area as an explaination for the elimination of voids in the interface. The experimental results of the examined resistance welding process or the model experiment suggest short-range diffusion for elimination of pores at the interface and a subsequent achievement of a close atom-to-atom contact by the high contact pressure as a mechanism for joint formation.

5. Explanatory approach and criterion for joint formation

As shown in the previous chapter, the joint formation in projection welding is comparable with the mechanisms known from diffusion welding. The variation of the fusion temperature and pressure in a model experiment lead to results that were comparable to the ones gained by welding trials with the example projection welding process. Nevertheless, since the model experiment is never able to completely reproduce the full physics of a projection welding process the outcome of the experiments of chapter 4.5 need to be critically discussed. Obviously, the main difference is the significantly longer heating time (20 ms compared to 60 s) resulting in a larger heat-affected zone in the model experiments.

As can be seen from figure 4-22, above 1200 °C, the holding time does not affect the joint strength. Together with the temperature, measurements of the example process (see fig. 4-6), a transfer of the results from the model experiment to the example process seems to be possible. A sample that is sufficiently welded in projection welding exhibits a maximum temperature above 1200 °C (in a distance of 500 µm from the fusion zone and above). Below this temperature, a decrease of the joint strength can be observed for short holding times indicating that temporal effects may be only relevant in a critical temperature range of transition. For a practical application, one should focus on the parameter that unambiguously lead to a sufficient weld. Thus, it seems to be justified to derive a criterion for the joint formation based on the temperature information of the model experiments.

The example process, as well as the model experiment show no significant volume diffusion at the interface and a pore free fusion zone (see figs. see figs. 4-3 and 4-28). Further the interface does not vanish which would be a consequence of bulk diffusion. This indicates that even for the model experiment the same mechanism of joint formation is applicable.

Comparing these results with the general understanding of diffusion welding (see fig. 4-1) [124, 125] it is obvious that projection welding as well as the joining performed with the model experiments differs for the third and fourth phase of the mechanism.

The first and the second phase, namely the initial contact of asperities and the formation of an interface by plastic deformation stays equal. Since there is no evidence that the initial interface vanishes in projection welding and in particular the model experiment, the grainboundary migration proposed in the third step of diffusion welding, does not occur. Furthermore, it needs only short range surface diffusion and re-orientation of the interfacial grains to form a closed interface. Remaining pores in the fusion zone are eliminated by the aid of the large plastic deformation that makes severe volume diffusion in the bulk material unnecessary. The applied high pressure also leads to a close contact of atoms and finally enables atomic bonding when the interface stops moving.

Modifing the illustration of *Nai et al.* [125] to satisfy the observations made for the joining of stainless steels in this work, thus leads to the scheme shown in figure 5-1.

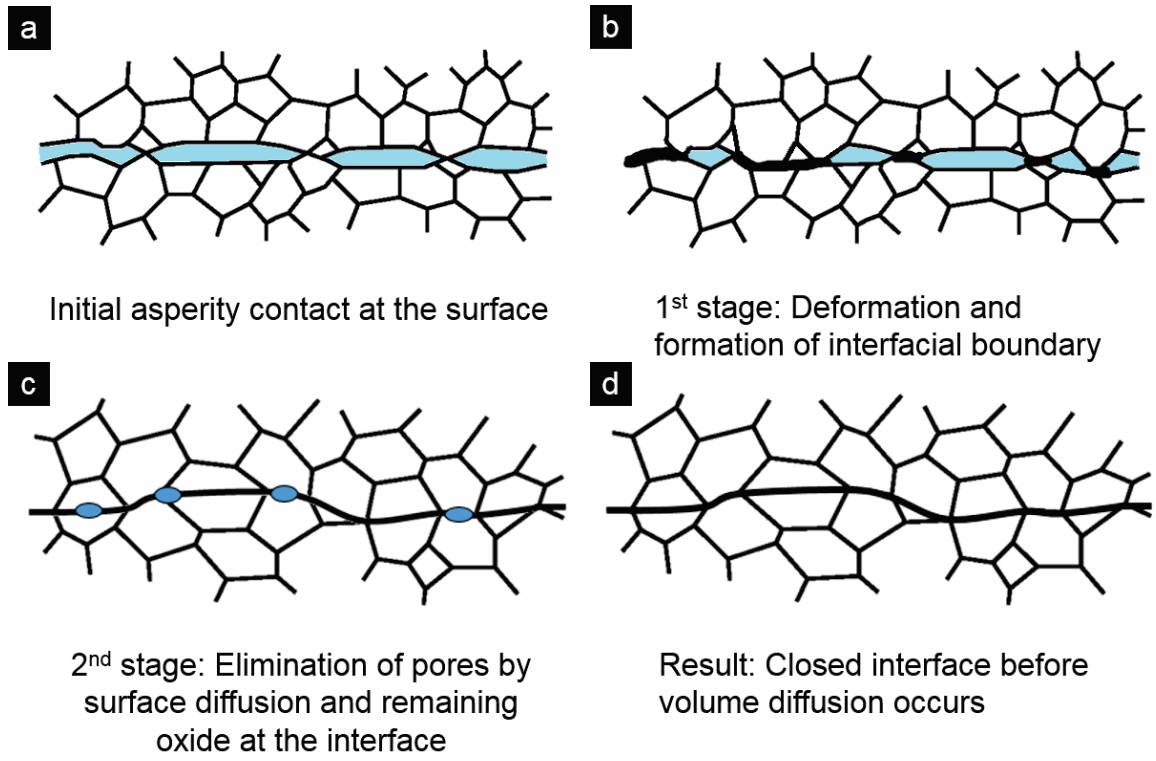

Figure 5-1: Illustration of the joint formation stages in solid state welding involving initial asperity contact (a), deformation and interfacial boundary formation (b), elimination of pores and grain boundary formation by surface diffusion (c) and closing of interface before volume diffusion occurs (d). Original image taken from [124, 125]. The enclosed ambient air is depicted blue.

The same can be done for the high temperature oxidation that occurred for low contact pressures. In this case the interface cannot be closed fast enough to exclude the oxygen which subsequently leads to oxidation of the hot contact surfaces (see fig. 5-2 a and b). In the following, the plastic deformation cannot break up the oxide but leads to flattening of the interface with remaining pores (see fig. 5-2 c). From the experiments, it cannot be clarified whether the interface is completely closed and all pores are vanished, since the oxidized samples could not be analysed in the joined state (examination of the interface was only possible after mechanical testing). Nevertheless, surface diffusion is expected at the high temperatures, which may eliminate remaining pores and form a closed oxidized interface (see fig. 5-2 d). This understanding needs to be examined in detail in the future.

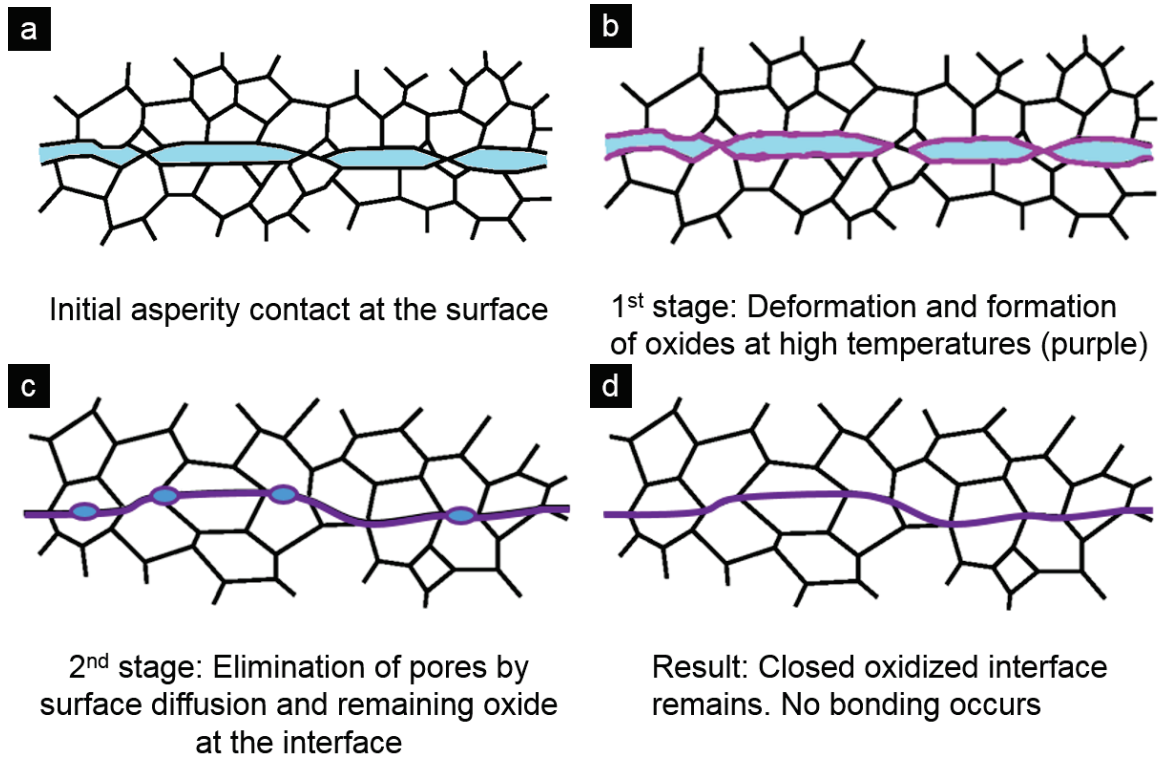

Figure 5-2: Illustration of the high temperature oxidation in solid state welding for high contact temperatures and low pressures in the approaching phase of the surfaces. Initial asperity contact (a), deformation and interfacial oxide formation (b), elimination of pores by surface diffusion and remaining oxide at the interface (c) and oxidized interface with no bonding (d). Original image taken from [124, 125]. The enclosed ambient air is depicted in blue, the oxide is shown in purple.

To derive a criterion for the joint formation that can be used for practical applications (e.g. welding process design or the interpretation of numerical simulation results), the temperature- and pressure-dependency of the joint strength is considered again. From the results shown in chapter 4 the criterion for joint formation of stainless steels can be formulated as follows:

- The first phase, where plastic flow at elevated temperature and contact pressure occurs, must be performed below 850 °C. Otherwise high temperature oxidation occurs and joint formation is hindered.
- In the second phase, sufficient joint formation can be achieved above 0.83 T_m. For temperatures below the re-arrangement of the grains and elimination of pores is not completed and joint strength decreses.

For the practical application in numerical simulation, thus the evaluation of the numerical result should focuse on the occurrence of the second phase. A sound weld can be identified by a fulfilment of the requirements of phase 2 at the interface between the two work pieces. If temperatures above 1200 °C (0.83 T_m) are reached in the heat-affected zone the criterion is fulfilled. The first criterion can be seen as mainly accounted to the design of the model setup. Since the contact pressures are much higher than possible in the model experiment (509 MPa compared to 1091 MPa) the temperature is much lower when plastic flow is initiated. Thus, the first criterion is fulfilled by projection welding processes in general.

Additionally the load bearing area, independent on the maximum temperature of the fusion zone, must be large enough to carry mechanical loads above σ_y of the weaker base material.

Since the work of other researchers [153] shows a sufficient joint formation at lower temperatures in vaccum, the use of shielding gas in projection welding may positively affect the welding results.

6. Numerical process simulation of projection welding

As mentioned in the state of the art (ch. 2), the numerical simulation of resistance welding processes is challenging due to the complex physical nature of the process. The coupling of thermo-electrical mechanical effects and the contact properties, such as friction, electrical contact resistance as well as thermal contact resistance need to be taken into account. This chapter focusses on the implementation of the physical process model derived in chapter 3 into an existing simulation method developed by Long [62] for the coupled thermo-electro-mechanical simulation of projection welding. The coupling method is introduced in chapter 6.1 and the model definition is given in chapter 6.2. A validation for the cold pre-pressing step is performed in chapter 6.3.1. Further the $R_{cont,el}$ influence (see ch. 6.3.2) on the process is again judged, based on the experimental data of chapter 3. A first attempt to check the model for the meaningful simulation of the fusion zone evolution with process time is made in chapter 6.3.3.

6.1 Introduction to the simulation method

Numerical simulation methods for projection welding are described e.g. by *Sun* [34], *Zhu et al.* [52], *Kristensen et al.* [49] or recently by *Nielsen et al.* [154]. Since these publications use their own code for the models the method of *Long* [63], running on the commercially available software *ABAQUS*, is applied in this work.

In general, the method consists of two implicit models, mechanical and thermo-electrical, which are explicitly sequentially coupled via a *Fortran* subroutine. In the mechanical model, the translations U and the resulting contact pressure p_{cont} are calculated based on the applied welding force for a defined analysis time. U is then transferred to the thermo-electrical model to define the deformed geometry and p_{cont} is mapped upon the parts to redefine the new contact situation ($R_{cont,el}$, $R_{cont,th}$). The themo-electrical model then calculates the temperature T due to the current flux through the newly defined geometry. After finishing the calculation, the temperature is

transferred back to the mechanical model, which then calculates U and p_{cont} again for the new temperature distribution. To handle large plastic deformations re-meshing of the geometries at defined time steps is performed before the restart of the next mechanical run. With this method, a severe mesh distortion leading to numerical instability is prevented. The coupling principle is illustrated in figure 6-1. For further details on the coupling method see the work of *Long* [63] and also the previous work of Woitun [155].

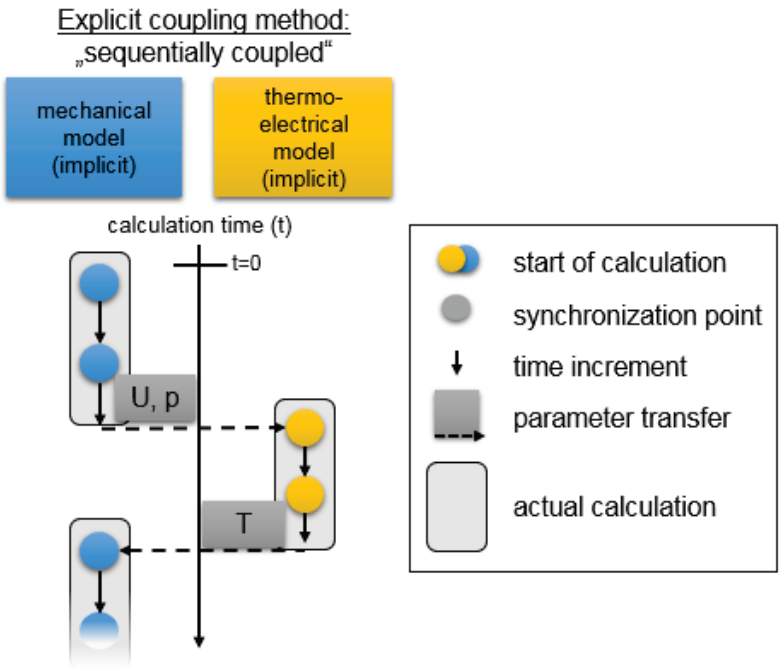

Figure 6-1:
Schematic illustration of the coupling method for thermo-electrical and mechanical simulation of resistance welding processes taken from [155].

6.2 Model definition

The model of *Long* used generic materials properties and contact properties to show the general applicability of the coupling method for the process simulation of projection welding. In this work, these properties were replaced according to the findings of chapter 3 to make first attempts of realistically simulating the example process used for the estimation of physical influencing parameters. A schematic overview of the considered quantities and the output parameters is given in figure 6-2.

For the simulation model no temperature dependent materials data was available. Thus the materials data was calculated based on the composition (according to the manufacturer delivery note) using the commercially available software *JMatPro*. In order to fit the mechanical results to the room temperature values of σ_y (provided by the manufacturer [89, 90], see appendix A, table A-1) the calculated stress-strain-curves were modified. The proportions of the high temperature curves to the room temperature curve was kept constant to keep the elevated temperature dependency. An overview of the data is given in table A-2 (appendix A).

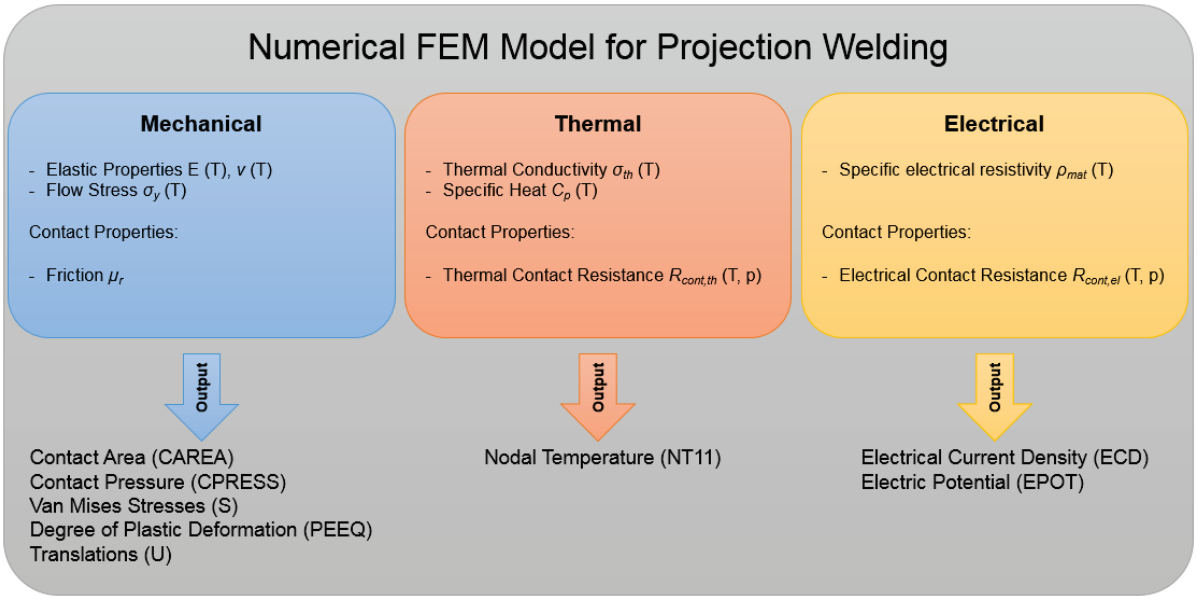

Figure 6-2: Model overview for input in the numerical FEM simulation of the example welding process. Note that thermal- and electrical contact resistances are used according to the concrete measurements and calculations in chapter 3.2. Although their relevance for projection welding is shown here to be neglectable, they are defined because *ABAQUS* needs a definition of these quantities in the model. The friction coefficient was set temperature independent to μ_r = 0.15 according to Popov [77].

The original welding geometry was adapted to simplify the simulation model. Upper and lower part were modeled as cylinders with an outer diameter of 21 mm for the top part and 42 mm for the bottom part. For better comparability of simulation and experiment, the geometry in the area of the fusion zone and especially the contact contour of both parts was not changed. Figure 6-3 shows a schematic of the welding setup as well as the details of the derived simulation model.

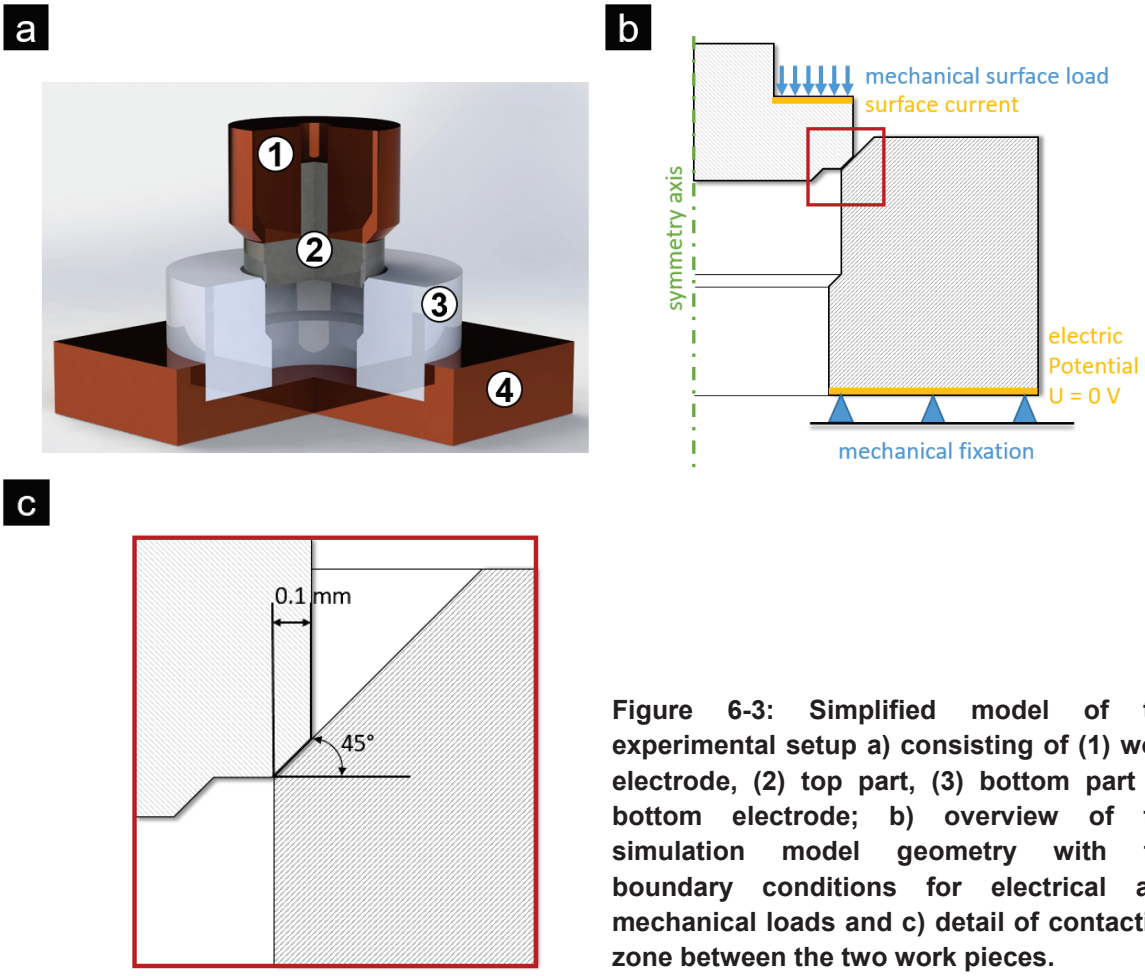

Figure 6-3: Simplified model of the experimental setup a) consisting of (1) work electrode, (2) top part, (3) bottom part (4) bottom electrode; b) overview of the simulation model geometry with the boundary conditions for electrical and mechanical loads and c) detail of contacting zone between the two work pieces.

6.3 Model validation

For the validation of the used simulation, the models of chapter 3.1 and 6 metallographic cross sections were used. Further, the recorded temperature profiles of chapter 4.3 were used to prove the simulation concept. An estimation of $R_{cont,el}$ influence on heating behaviour was examined. The simulation model was validated based on cross sections at different process time steps as well as the temperature evolution measured within the process.

6.3.1 Cold pre-deformation

To proof the validity of the numerical results for the cold pre-deformation, metallographic cross sectioning was utilized. The work pieces were loaded with a force of 18 kN by the aid of the welding device and then unloaded again. After this procedure, the parts were separated and the deformed contour of each work piece was measured out from the cross section. The results were then compared to the simulation results (see fig. 6-4). To take into account the elastic recovery of the materials, the simulations also contained an unloading of the geometry and thus a separation of the parts.

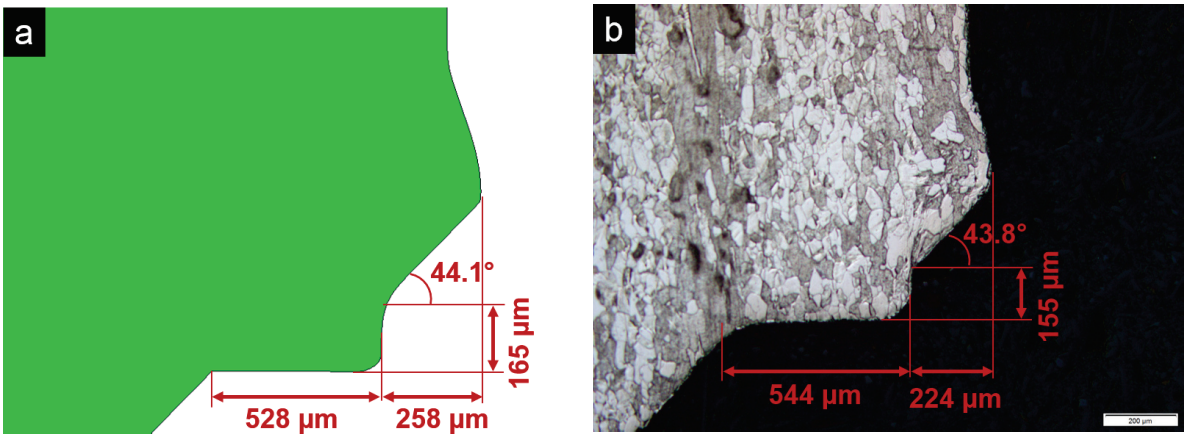

Figure 6-4: Result of the numerical simulation for the cold pre-pressing step (a) and metallographic cross section of a work pieces loaded with 18 kN of force (b).

A comparison of the simulation contours with the experimental results demonstrates a high accuracy of the FEM model. The depth of the press fit is calculated sufficiently whereas the extrusion of material and the bead formation is slightly overestimated (258 µm vs. 224 µm). These results are important for the estimated contact pressure distribution determined in chapter 3.1 (see fig 3-3). Since the contact pressure was used in the discussion of process physics, especially for thermal- and electrical contact resistances, a validated simulation model supports these discussions and the results of the performed estimations.

6.3.2 Contact resistance influence

Since the electrical contact conductance is a mandatory variable for thermal-electrical contact models in *ABAQUS*, the experimental values of chapter 3.2.3 were implemented in the simulation model. For the high-pressure regime where $R_{cont,\,el}$ goes to zero, the electrical contact conductance, as the inverse of $R_{cont,\,el}$, is divergent. To ensure numerical stability the values were modified and kept constant at pressures above 520 MPa (see fig 6-5,a). This pressure was chosen according to the last data point of the measurements for the combined $R_{cont,\,el}$ (see fig. 3-15, c).

To quantify the role of $R_{cont,\,el}$ for projection welding it was systematically varied in a simulation series (see fig. 6-5, b) for the same welding current, welding force and further contact conditions. $R_{cont,el}$ was varied within the accuracy of the measurements indicated by the error bars in appendix B-3. Figure 6-5 shows the input curves for numerical simulation (contact resistance (a) and contact conductance (b)) that were used for the study.

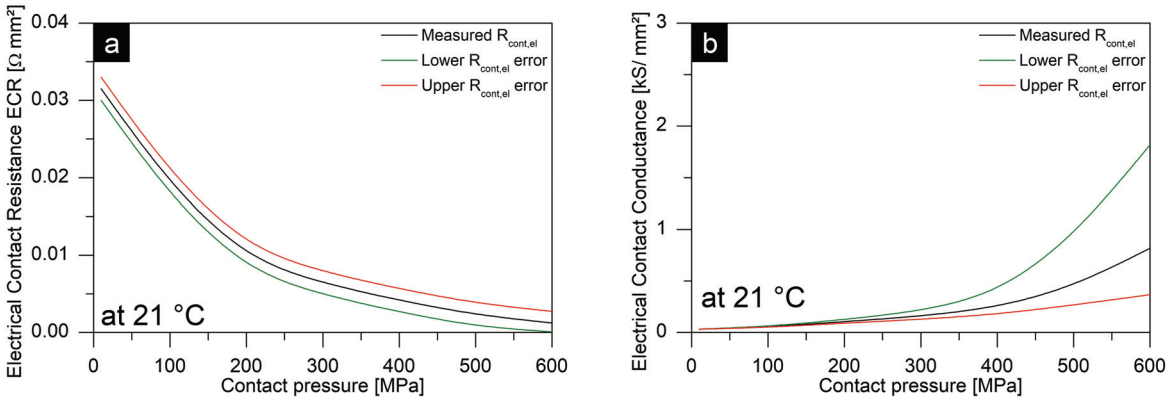

Figure 6-5: Original curve as well as adjusted curves of the electrical contact resistance (a) and conductance (b) at room temperature. The adjusted curves represent the upper and lower error of the $R_{cont,el}$ measurements and were used in the *ABAQUS* model to quantify the effect on the heat generation inside the fusion zone. Note that the calculation of the contact conductance is needed since *ABAQUS* uses these values as input parameter. The data at different temperature for each of the three cases are given in appendix A-10 to A-12.

Since the thermal influence on $R_{cont,el}$ was not examined in chapter 3 the high temperature values were assumed according to the observations of Rogeon et al [87].

As already mentioned, they observed a drop of $R_{cont,el}$ by a factor of six within the first 330 °C when heating up the contact starting from room temperature.
The numerical results show a non-homogeneous temperature distribution in the fusion zone for every time step as depicted in figure 6-6. This observation can be accounted to the constriction resistance effect induced by the geometrical shape of the samples. This leads to a higher temperature in areas where the current density increases (point A and C in figure 6-6 a, c, d) and lower temperature in the middle of the fusion zone (point B in figure 6-6 a, c, d). From these images it also beomes clear that the variation of $R_{cont,el}$ within the error of the measurement has no significant influence on the temperature profile (see fig. 6-6 b, d, f). Furthermore, the results confirm the statement of chapter 3.2.2 that $R_{cont,el}$ does not substantially contribute to the heating of the fusion zone, due to the small (or vanishing) values at high contact pressures.

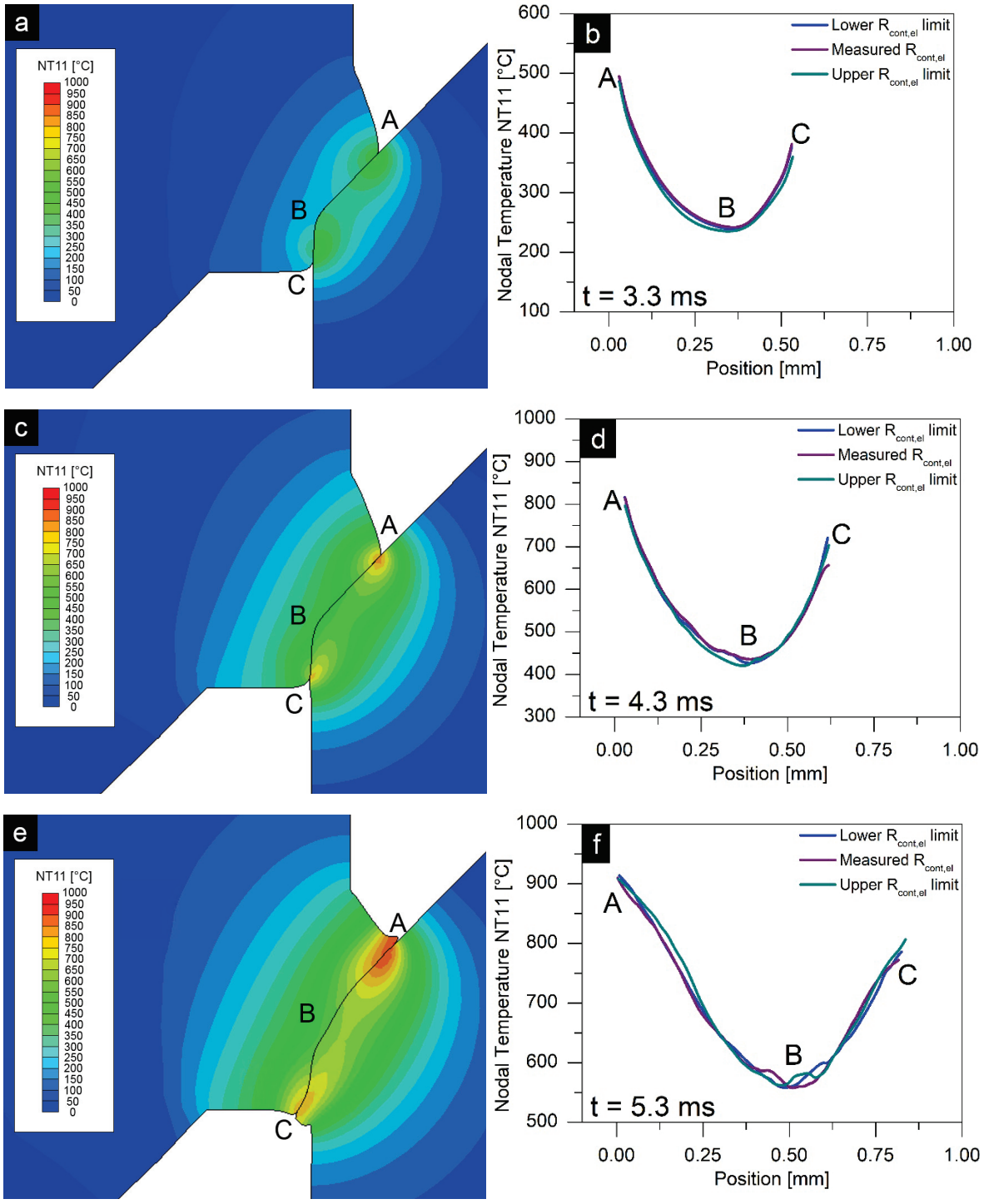

Figure 6-6 Numerical results of the $R_{cont,el}$ study at different times showing temperature distribution in the fusion zone (a, c, e) as well as the temperature profile for the path A-B-C along the interface (b, d, f). The $R_{cont,el}$ values were varied according to the lower error limit (blue curve), the measured values (purple curve) and the upper error limit (turquoise curve). Note that the path A-B-C is stretched due to the plastic deformation and is thus longer for 5.3 ms than for 4.3 ms and 3.3 ms.

6.3.3 Progress of fusion zone formation

The described model was used to simulate the example welding process with a peak electrical current of I = 57 kA and the use of a mechanical stopper adjusted to a welding distance of 0.68 mm. A metallographic cross section was used to check the simulation result (see fig. 6-7). Apparently, the simulation is in good agreement with the cross section. Only the detailed geometry of the material expelled from the fusion zone differs from the experiments. Further, the simulation also predicts the double “s” shaped interface of the work pieces.

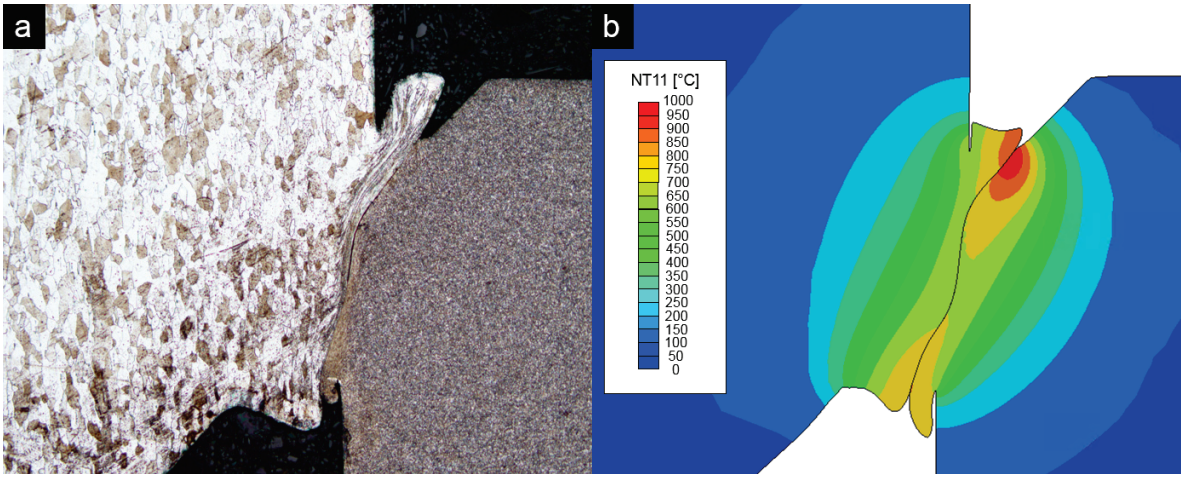

Figure 6-7: Comparison of the metallographic cross section for a weld with mechanical stopper at 0.6 mm (a) and the simulation with depicted temperature field for the same distance (b).

Further the welding distance as well as the temperature evolution was used (see fig. 6-8 a) for validation of the model. For the distance, a good agreement was found (see fig. 6-8 b). Since the temperature measurement was not possible directly in the fusion zone, a comparison of the numerical prediction with the experimental data is difficult. The maximum temperature from the simulation is rising faster, reaches a higher maximum at an earlier time. Due to dissipation of heat apart from the fusion zone, this result seems plausible. The thermocouple placed in a distance of 495 µm from the fusion zone detects the temperature much later due to the thermal conductivity delay. In addition, the detected temperature is lower due to dissipation of the heat. In

context of these observations, the results seem to fulfil the physical understanding of heat transport. Nevertheless, a quantitative comparison of the simulations validity is not possible.

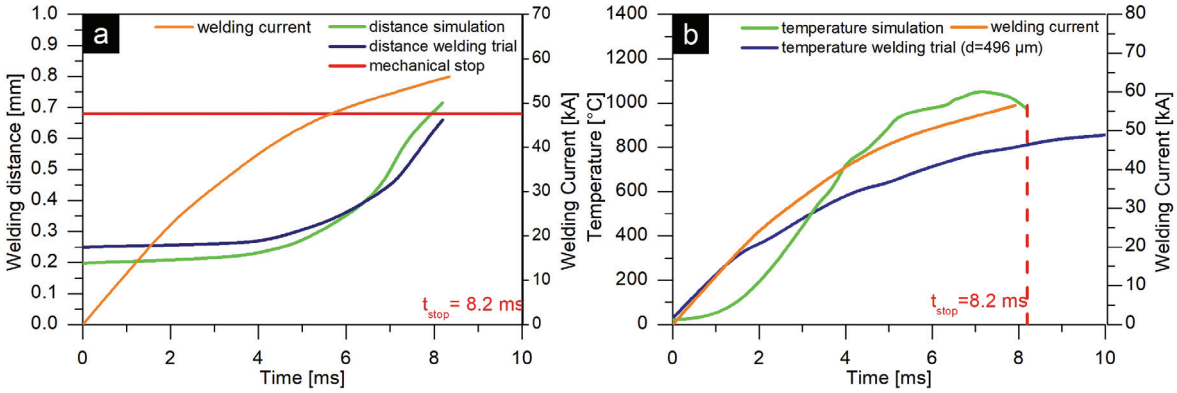

Figure 6-8: Comparison of simulation results with experimental data of distance (a) and maximum temperature evolution (b). Since the example process was stopped artificially using a mechanical stopper (adjusted to a distance of 0.7 mm; corresponding to 8.2 ms; welding peak current 57 kA; orange curve), the simulation data was only evaluated until this point. The temperature data was taken from figure 4-5.

Concluding the above simulation study, the first attempts showed a good agreement with the welding experiments of the example process. For the cold pre-pressing step, the numerical results fit to the metallographic cross section for the same mechanical load. This indicates that the contact pressures identified in chapter 3 are realistic values. Furthermore this means, that the estimated pressure range for $R_{cont,el}$ should be valid. The same holds for the relevance of $R_{cont,el}$ as a heat source, since the numerical results do not show a dependency of the fusion zone temperature profile on the values of $R_{cont,el}$.

Nevertheless, due to numerical instabilities of the model, it has never been possible yet to finish a complete welding simulation and thus to compare the simulation output with the final welding result of the example process.

7. Conclusion and outlook

This work's results are concluded in a sub-chapter for each of the focal points. The process physics of projection welding is discussed in chapter 7.1, the joint formation in projection welding in chapter 7.2 and the numerical simulation of projection welding in chapter 7.3. An outlook for the respective focal point is given at the end of each sub-chapter.

7.1 Process physics of projection welding

A systematic estimation of the physical quantities that are influencing projection welding processes was conducted. For this, an example process was utilized to measure, analytically calculate or numerically determine these quantities.

It was shown that high contact pressures above 1 GPa can be achieved in projection welding applications, which significantly influence the electrical and thermal conditions of the contact interface. Interfacial shearing makes the process unsusceptible to surface qualities of the work pieces.

In focus of process physics, the profound study on the role of the electrical contact resistance is one of the most noticible parts of this work. In the literature, only experimental results on absolute and non-area-related contact resistances can be found, which were determined on a complex, real application-oriented geometry. On the other hand, the area-related contact resistance could be determined on the basis of academic samples, but these measurements were limited to pressures well below the yield strength. A method used for the determination of electrical contact resistances was optimized in this dissertation in such a way that a (geometry-independent) measurement of contact resistances for mechanical loads up to the yield strength of the material is made possible. For this, an experimental setup was developed to directly measure electrical contact resistances in this mechanical load regime.

Measurements were performed using 1.4511 (AISI 430 Nb) and 1.4057 (AISI 431) stainless steels as test materials. Furthermore, contacts between the single materials as well as the combination of both were included in the measurements. The results show that the electrical contact resistance vanishes for contact pressures above the tensile strength of the considered stainless steels. To proof the transferability of the results, the measurements were performed for two different geometries and, additionally, in experiments on the joint formation in projection welding which are described in chapter 7.2.
Since the electrical contact resistance vanishes for pressures around the yield strength (where the examined resistance projection welding process is usually applied), no contribution of this quantity to the *Joule Heating* in projection welding is expected.
The analysis of the measurements also revealed a linear decrease of the electrical contact resistance for contact pressures above half of the yield strength. For pressures around the yield strength, the electrical contact resistance vanishes completely. These findings were not reported in literature yet. A theoretical description of the observed linear relation between contact resistance and contact pressure was derived. Part of the theoretical consideration was the collapse of small pores remaining at the interface even at high pressures, and vanishing completely at yield strength of the considered materials. The derived relation was validated by the aid of results from numerical molecular dynamic simulations of previous works.

To understand the thermal contact physics in context of projection welding the measured electrical contact resistances were converted into thermal contact resistances by the aid of the *Widemann-Franz Law*. The calculations show that an ideal thermal contact can be assumed in such applications due to the high contact pressures in the fusion zone. A comparison with the analytical results of the common thermal contact theory confirms this statement.

The relevance of electro-magnetic effects was estimated using numerical methods. *Eddy Current Heating* was modeled for a typical current pulse using ANSYS Maxwell. To take into account mechanical effects of the magnetic field, a virtual force simulation

was performed, which enabled evaluation of the *Lorentz Forces* as a function of the current pulse time. Concluding the simulation results, neither *Eddy Current Heating* nor *Lorentz Forces* are influencing the process.

The presented results enable a deeper understanding of the physics of resistance projection welding processes. Since the relevant physical quantities are known now, tailoring of such processes to new welding applications is simplyfied. To further enhance the process understanding and the physical basis for numerical process simulation a repetition of the electrical contact resistance experiments is suggested with respect to the electrode materials. The contact pressures occurring at the electrode-workpiece interface are expected to be much smaller than at the workpiece-workpiece interface due to a larger area for same applied force. Thus, a repetition of the measurements considering electrode materials and combinations of workpiece materials and electrode materials is meaningful. Also, the thermal influence of these components, e.g. cooling of the work pieces due to high thermal conductivity of the electrodes may not be negligible. Hence, with this knowledge, the simulation model could be expanded to the eletrodes and the accuracy of the predicted welding result could be increased.

7.2 Joint formation in projection welding

The second focal topic of this work is the joint formation in resistance projection welding. There is no mechanism for the joint formation described in literature yet. However, this question is of decisive importance both for the more precise design of the processes and for the numerical process simulation. This thesis presents a deeper analysis of this topic and proposes a possible mechanism for the joint formation.
Projection welding, especially the considered example process, can be accounted to the solid state welding processes. To enhance the understanding of joint formation in projection welding, experiments were performed for the example of stainless steels as work piece materials. Since the influencing quantities, namely temperature, contact pressure and pre-deformation, cannot be varied idependently in the projection welding

process, a model experiment was designed. By the aid of these experiments, these quantities were varied within a range of 1173 K and 1573 K and 72 MPa to 509 MPa in ambient atmosphere. Further, cold pre-deformation and the influence of the heating step were considered. For comparison of the model experiments with the example projection welding process, temperature-measurements, mechanical testing as well as metallographic analytics were utilized.

It was found that sufficient metallurgical joining is achieved for temperatures above 1473 K and contact pressures above 258 MPa. These values are 0.83 of the melting temperature T_m and ½ of the yield strength σ_y of the weaker of both stainless steels. Between the model process and the results of the considered example projection welding process good agreement was found. For further work on numerical process simulation, these threshold conditions can thus be taken as a criterion to judge the success of the weld.

The results were discussed in context of the common understanding of solid state welding mechanisms (diffusion welding, hot rolling, etc.). Based on these theories an explanatory approach is suggested. Solid state projection welding incorporates four different steps that can be concluded as follows:

1. When the sample surfaces are brought together a contact between the surface asperities is established.
2. An intimate interfacial boundary is formed when the interface is plastically deformed at elevated temperatures
3. Contradictory to diffusion welding an elimination of pores by volume diffusion does not occur. Furthermore, it is surface diffusion that enables re-arrangement of the interface to perfectly fit. The interface persists during the whole process.
4. Closed interface that visually separates the incorporated materials after cooling

For low contact pressures and temperatures above 1073 K, high temperature oxidation of the interface was observed which prevented the joint formation. This indicates that

plastic materials flow and closing of the interface needs to be completed already at low temperatures to exclude oxidation.

For further improvement of the understanding of joint formation in projection welding the following future work is suggested. To proof the validity of the determined criterion the experiments can be repeated for materials with lower melting temperature (such as copper or aluminum). Aditionally, materials combinations with dissimilar melting temperatures can be investigated, since it is expected that a modification of the criterion may be necessary under these circumstances. A repetition of the experiments in vacuum or with shielding gas could verify the high temperature oxidation hypothesis. In this case the formation of reliable joints without oxidation of the interfaces should already be possible at lower contact pressures even for higher temperatures, due to the lack of oxygen.

7.3 Numerical simulation of projection welding

Numerical process simulation can be utilized to safe development time and reduce experimental effort. To show theses potentials, the process physics model concluded in chapter 7.1 was implemented into an existing coupling method for the commercially available software ABAQUS.
First simulation attempts showed good agreement with the welding device data and metallographic analytics, as well as temperature measurements. This indicates that the derived understanding of process physics is sufficient to describe projection welding and serve the numerical process simulaton.
Nevertheless, the used numerical coupling method needs to be improved further, since none of the simulations was numerically unstable up to the end of the process. Thus, a validation of the applicability of the joint formation criterion by the numerical simulation could not be realized.

Publications

Parts of this work were already published as follows:

Chapter 3:

Wehle M., Schmid, F. and Schmitz, G. “Bedeutung des elektrischen Kontaktwiderstandes beim KE-Einpressschweißen, *DVS Congress 2017*, Düsseldorf, 2017, p. 143- 147. [156]

Wehle M., Schmid, F., Schmitz, G and Greitmann, M. “Experimental Study on the Role of the Electrical Contact Resistance in Resistance Projection Welding”, *The 10th International Seminar & Conference on Advances in Resistance Welding*, Esslingen, 2018. [157]

Wehle M., Schmid, F., Schmitz, G and Greitmann, M.: “*Experimental Determination of Electrical Contact Resistance for high mechanical Loads up to Tensile Strength*”, to be published

References

[1] Fahrenwaldt, H. J., Schuler, V., Twrdek, J. 2014. *Praxiswissen Schweißtechnik*. *Werkstoffe, Prozesse, Fertigung*. Springer Fachmedien, Wiesbaden. ISBN 3658031417.

[2] Pouranvari, M. and Marashi, S. P. H. "Critical review of automotive steels spot welding". *Science and Technology of Welding and Joining*, **18,** 5, (2013), p. 361–403.

[3] Hamedi, M. and Atashparva, M. "A review of electrical contact resistance modeling in resistance spot welding". *Welding in the World*, **61,** 2, (2017), p. 269–290.

[4] DIN EN ISO 4063:2011-03. *Schweißen und verwandte Prozesse – Liste der Prozesse und Ordnungsnummern*. Deutsches Institut für Normung. 2011. Beuth Verlag, Berlin.

[5] DVS Ausschuss für Technik, Arbeitsgruppe "Widerstandsschweißen" "Merkblatt DVS 2911 Kondensatorentladungsschweißen – Grundlagen, Verfahren und Technik, (2016).

[6] DVS Ausschuss für Technik, Arbeitsgruppe "Widerstandsschweißen" "Merkblatt DVS 2905 Buckelschweißen von Stählen, (2001).

[7] DIN EN ISO 16432: „Widerstandsschweißen - Verfahren zum Buckelschweißen von niedriglegierten Stählen mit oder ohne metallischem Überzug (ISO 16432:2006).“, Europäisches Komitee für Normung, Deutsches Institut für Normung. 2007. Beuth Verlag, Berlin.

[8] DVS Ausschuss für Technik, Arbeitsgruppe "Widerstandsschweißen" "Merkblatt DVS 2950 Widerstandsschweißen in der Elektronik und Feinwerktechnik – Übersicht und Grundlagen, (2010).

[9] Chen, Z. "Joint formation mechanism and strength in resistance microwelding of 316L stainless steel to Pt wire". *J Mater Sci*, **42,** 14, (2007), p. 5756–5765.

[10] Fukumoto, S. and Zhou, Y. "Mechanism of resistance microwelding of crossed fine nickel wires". *Metallurgical and Materials Transactions A*, **35,** 10, (2004), p. 3165–3176.

[11] Fukumoto, S., Matsuo, T., Tsubakino, H., and Yamamoto, A. "Resistance Microwelding of SUS304 Stainless Steel Fine Wire". *Materials Transactions*, **48,** 4, (2007), p. 813–820.

[12] Khan, M. I., Kim, J. M., Kuntz, M. L., and Zhou, Y. "Bonding Mechanisms in Resistance Microwelding of 316 Low-Carbon Vacuum Melted Stainless Steel Wires". *Metallurgical and Materials Transactions A*, **40,** 4, (2009), p. 910–919.

[13] Zhou, Y., Gorman, P., Tan, W., and Ely, K. J. "Weldability of thin sheet metals during small-scale resistance spot welding using an alternating-current power supply". *Journal of Electronic Materials*, **29,** 9, (2000), p. 1090–1099.

[14] Khan, M. I., Kuntz, M. L., and Zhou, Y. "Effects of weld microstructure on static and impact performance of resistance spot welded joints in advanced high strength steels". *Science and Technology of Welding and Joining*, **13,** 3, (2013), p. 294–304.

[15] Matsuda, F., Fukada, Y., Okada, H., Shiga, C., Ikeuchi, K., Horii, Y., Shiwaku, T., and Suzuki, S. "Review of mechanical and metallurgical investigations of martensite-austenite constituent in welded joints in Japan". *Welding in the World / Le Soudage dans le Monde*, **3,** 37, (1996), p. 134–154.

[16] Venkataraman, S. and Devletian, J. H. "Rapid Solidification of Stainless Steels by Capacitor Discharge Welding". *Welding Journal*, **67,** 6, (1988), p. 111–118.

[17] Venkataraman, S. 1986. *Rapid solidification of stainless steels and FeAl ordered alloy by capacitor discharge welding*.

[18] Wilson, R. D., Woodyard, J. R., SR., and Devletian, J. H. "Capacitor Discharge Weding: Analysis through Ultrahigh Speed Photography". *Welding Journal*, **72**, (1993), p. 101–106.

[19] Chiozzi, S., Dattoma, V., and Panella, F. "Capacitor discharge welded bars of Inconel 718 and TiAl6V4 superalloys under fatigue". *Materials & Design*, **29,** 4, (2008), p. 839–851.

[20] Tušek, J., Tuma, J. V., Jenko, M., and Pograjc, M. "Direct resistance projection welding of copper and brass". *Science and Technology of Welding and Joining*, **10,** 1, (2005), p. 1–6.

[21] Tslaf, A. "A Thermophysical Criterion for the Weldability of Electric Contact Material in a Steady-State Regime". *IEEE Trans. Comp., Hybrids, Manufact. Technol.*, **5,** 1, (1982), p. 147–152.

[22] Cooper, D. R., Allwood, J. M. "The influence of deformation conditions in solid-state aluminium welding processes on the resulting weld strength". *Journal of Materials Processing Technology*, **214,** 11, (2014), p. 2576–2592.

[23] Tang, W. ,Guo, X. McClure, J., Lawrence, M., Nunes, A. C. "Heat Input and Temperature Distribution in Friction Stir Welding". *Journal of Materials Processing & Manufacturing Science*, **7**, (1998), p. 136–172.

[24] Zhu, X. K., Chao, Y. J. "Numerical simulation of transient temperature and residual stresses in friction stir welding of 304L stainless steel". *In Journal of Materials Processing Technology*, **146,** 2, (2004), p. 263–272.

[25] Costanzi, G., Bachmann, A., Zäh, M. F. "Entwicklung eines FSW Spezialwerkzeugs zur Messung der Schweißtemperatur". *DVS Congress 2017, Düsseldorf*, (2017), p. 119–125.

[26] Milner, D. R. and Rowe, G. W. "Fundamentals of Solid-Phase Welding". *Metallurgical Reviews*, **7,** 1, (1962), p. 433–480.

[27] Erdmann-Jesnitzer, F. and May, M. "Gesetzmäßigkeiten bei Verwachsungszuständen von Kristallen- 1. Zeit-Temperatur-Gesetz und Energiewerte". *Zeitschrift für Metallkunde,* 46, (1955), p. 756–764.

[28] Parks, J. M. "Recrystallization Welding". *Welding Journal Supplement,* 32, (1953), p. 209–222.

[29] Tylecote, R. F. "Investigations on Pressure Welding". *British Welding Journal*, **1,** 3, (1954), p. 117–135.

[30] Mackerle, J. "Finite element analysis and simulation of welding- A bibliography (1976- 1996)". *Modelling and Simulation in Materials Science and Engineering*, **4,** 5, (1996), p. 501–533.

[31] Mackerle, J. "Finite element analysis and simulation of welding - an addendum: a bibliography (1996-2001)". *Modelling and Simulation in Materials Science and Engineering*, **10,** 3, (2002), p. 295–318.

[32] Zhang, W., Ed. 2003. *Design and Implementation of Software for Resistance Welding Process Simulations.* SAE Technical Paper Series. SAE International400 Commonwealth Drive, Warrendale, PA, United States.

[33] Zhang, W. "Recent Advances and Improvements in the Simulation of Resistance Welding Processes". *Welding in the World*, **50,** 3-4, (2006), p. 29–37.

[34] Sun, X. "Modeling of Projection Welding Processes Using Coupled Finite Element Analyses". *Welding Journal*, **79,** 9, (2000), p. 244–251.

[35] Huh, H. and Kang, W. J. "Electrothermal analysis of electric resistance spot welding processes by a 3-D finite element method". *Journal of Materials Processing Technology*, **63,** 1-3, (1997), p. 672–677.

[36] Kußmaul, K., Blind, D., Zeng, L., Greitmann, M. J., Schäfer, P. M. "Numerische Prozeßsimuation von Widerstandsbuckelschweißungen.". *DVS Berichte,* 142, (1991), p. 143–150.

[37] Erofeev, V. A. and Pyankov, I. B. "Physico-mathematical model of resistance projection welding of cruciform joints". *Welding International*, **31,** 10, (2017), p. 796–801.

[38] Nied, A. "The Finite Element Modeling of the Resistance Spot Welding Process". *Welding Journal*, **63,** 4, (1984), p. 123–132.

[39] De, A., Thaddeus, M. P., and Dorn, L. "Numerical Modelling of Resistance Spot Welding of Aluminium Alloy". *ISIJ International*, **43,** 2, (2003), p. 238–244.

[40] Sun, X., Stephens, E. V., Khaleel, M. A., Shao, H., and Kimchi, M. "Resistance Spot Welding of Aluminum Alloy to Steel with Transition Material- From Process to Performance- Part I: Experimental Study". *Welding Journal*, **83**, (2004), p. 188–195.

[41] Sun, X. and Khaleel, A. "Resistance Spot Welding of Aluminum Alloy to Steel with Transition Material Part II: Finite Element Analyses of Nugget Growth". *Welding Journal*, **83,** 7, (2004), p. 197–202.

[42] Sun, X. and Dong, P. "Analysis of Aluminum Resistance Spot Welding Processes Using Coupled Finite Element Procedures". *Welding Journal*, **79,** 8, (2000), p. 215–221.

[43] Greitmann, M. J., Rauch, R. "SPOTWELDER - Ein Rechenprogramm zur numerischen Simulation des Widerstandspunktschweißprozesses". *Deutscher Verlag für Schweißtechnik, DVS Berichte*, **189**, (1998).

[44] Kußmaul, K. 1993. *Qualitätssicherung durch numerische Analyse der mechanischen und thermischen Prozesse beim Widerstandspunktschweißen*. *Abschlussbericht Forschungsvorhaben DVS-Nr. 04.191 / IGF-Nr.: Q10*.

[45] Lanier, O. *Kontaktwiderstandsmodell für die Simulation des Fügens durch Widerstandserwärmen*. Dissertation, Institut für Materialprüfung, Werkstoffkunde und Festigkeitslehre (IMWF), Universität Stuttgart.

[46] Dreyer, W., Duderstadt, F., and Hömberg, D. "Finite-Element-Simulation des Kondensator-Impuls-Schweißens". *Technische Mechanik*, **19,** 4, (1999), p. 331–340.

[47] Luo, A. H. and Chen, G. L. "Process Analysis on a Special Projection Welding with Coupled FEM". *Materials Science Forum*, **471-472**, (2004), p. 795–800.

[48] Sun, X. "Effect of Projection Height on Projection Collapse and Nugget Formation — A Finite Element Study". *Welding Journal*, **80,** 9, (2011), p. 211–216.

[49] Kristensen, L., Zhang, W., and Bay, N. "Numerical and experimental investigation of geometric parameters in projection welding". *10th Int. Conf. on Computer Technology in Welding and Manufacturing*, (2000).

[50] Greitmann, M. J. ,Roos, E. 2011. *Grundlegende Untersuchung zur Kontaktsituation beim Widerstandsschweißen von Kupferwerkstoffen*. *FORSCHUNGSVORHABEN AiF-Nr. 15710 N/1 ▪ DVS-Nr. 04.046*.

[51] Wang, S. C. and Wei, P. S. "Modeling Dynamic Electrical Resistance During Resistance Spot Welding". *Journal of Heat Transfer*, **123,** 3, (2001), p. 576.

[52] Zhu, W.-F., Lin, Z.-Q., Lai, X.-M., and Luo, A. H. "Numerical analysis of projection welding on auto-body sheet metal using a coupled finite element method". *International Journal of Advanced Manufacturing Technology*, **28**, (2006), p. 45–52.

[53] Browne, D. J., Chandler, H. W., Evans, J. T., and Wen, J. "Computer Simulation of Resistance Spot Welding in Aluminum: Part I". *Welding Journal*, **74,** 10, (1995), p. 339–344.

[54] Browne, D. J., Chandler, H. W., Evans, J. T., James, P. S., Wen, J., and Newton, C. J. "Computer Simulation of Resistance Spot Welding in Aluminum: Part II". *Welding Journal*, **74,** 12, (1995), p. 417–422.

[55] Casalino, G. and Ludovico, A. D. "Finite element simulation of high speed pulse welding of high specific strength metal alloys". *Journal of Materials Processing Technology*, **197,** 1-3, (2008), p. 301–305.

[56] Song, Q., Zhang, W., and Bay, N. "Contact Modelling in Resistance Welding. Part 1". *Proceedings of the Institution of Mechanical Engineers, Part B: Journal of Engineering Manufacture*, **220,** 5, (2006), p. 599–606.

[57] Song, Q., Zhang, W., and Bay, N. "Contact Modelling in Resistance Welding. Part 2". *Proceedings of the Institution of Mechanical Engineers, Part B: Journal of Engineering Manufacture*, **220,** 5, (2006), p. 607–613.

[58] Song, Q. "Testing and Modeling of Contact Problems in Resistance Welding, (2013).

[59] Feulvarch, E., Robin, V., and Bergheau, J. M. "Resistance spot welding simulation: A General Finite Element Formulation of Electrothermal Contact Conditions". *Journal of Materials Processing Technology*, **153-154**, (2004), p. 436–441.

[60] Robin, V., Sanchez, A., Dupuy, T., Soigneux, J., and Bergheau, J. M. "Numerical Simulation of Spot Welding with special attention to contact conditions". *Book Institute of Materials*, **784**, (2002), p. 997–1016.

[61] Sibilia, G., Rogeon, P., Paillard, P., Saindrenan, G., Soigneux, J., Lemasson, P., and Carron, D. "Experimental validation of an electro-thermo-metallurgical predictive model in resistance spot welding". *Journal de Physique IV*, **120**, (2004), p. 689–696.

[62] Cavaliere, P., Dattoma, V., and Panella, F. W. "Numerical analysis of multipoint CDW welding process on stainless AISI304 steel bars". *Computational Materials Science*, **46,** 4, (2009), p. 1109–1118.

[63] Long, F. X. 2018. *Development of a Re-meshing Method for the Finite-Element Simulation of a Capacitor Discharge Press-Fit Welding Process*. Bachelor Thesis, Karlsruher Institut für Technologie.

[64] Fritz, A. H. , Schulze, G. 2012. *Fertigungstechnik*. Springer-Lehrbuch. Springer, Berlin, Heidelberg. ISBN 9783642297854.

[65] Grote, K.-H., Feldhusen, J. 2011. *Dubbel*. *Taschenbuch für den Maschinenbau*. Springer, Berlin. ISBN 9781283365703.

[66] Timsit, R. S. "Electrical contact resistance: Properties of stationary interfaces". *IEEE Transactions On Components and Packaging Technology*, **22,** 1, (1999), p. 85–98.

[67] Timsit, R. S. "Constriction Resistance of Thin Film Contacts". *IEEE Transactions On Components and Packaging Technology*, **33,** 3, (2010), p. 636–642.

[68] Nakamura, M. "Constriction resistance of conducting spots by the boundary element method". *IEEE Transactions on Components, Hybrids, and Manufacturing Technology*, **16,** 3, (1993), p. 339–343.

[69] Yovanovich, M. M. "Conduction and thermal contact resistances (conductances)". *Handbook of Heat Transfer,* 3, (1998), p. 3–34.

[70] Holm, R. 1967. *Electric contacts*. *Theory and application*. Springer-Verlag, Berlin, New York. ISBN 364205708X.

[71] Holm, R. 1941. *Die technische Physik der elektrischen Kontakte*. Springer-Verlag, Berlin Heidelberg. ISBN 978-3-662-42222-9.

[72] Holm, R. 1958. *Elektrische Kontakte/ Electric Contacts Handbook*. Springer-Verlag, Berlin Heidelberg. ISBN 978-3-662-23790-8.

[73] Dorsey, G. 2015 "If Holm had used a Scanning Tunneling Microscope: What the nanoscientists are teaching us about electrical contacts. In *Proceedings of the Sixty-first IEEE Holm Conference on Electrical Contacts*. IEEE, Piscataway, NJ, p. 63–75.

[74] Greenwood, J. A. and Williamson, J. B. P. "Contact of Nominally Flat Surfaces". *Proceedings of the Royal Society A: Mathematical, Physical and Engineering Sciences*, **295,** 1442, (1966), p. 300–319.

[75] Greenwood, J. A. "Constriction resistance and the real area of contact". *British Journal of Applied Physics*, **17,** 12, (1966), p. 1621–1632.

[76] Ben Jemaa, N. "Contacts conduction and switching in DC levels". *Electrical Contacts - 2002. Proceedings of the Forty-Eighth IEEE Holm Conference on Electrical Contacts*, **2002**, , p. 1–15.

[77] Popov, V. L. 2009. *Kontaktmechanik und Reibung. Ein Lehr- und Anwendungsbuch von der Nanotribologie bis zur numerischen Simulation*. Springer Berlin Heidelberg, Berlin, Heidelberg. ISBN 9783540888369.

[78] Zhai, C., Hanaor, D., Proust, G., Brassart, L., and Gan, Y. "Interfacial electro-mechanical behaviour at rough surfaces". *Extreme Mechanics Letters*, **9**, (2016), p. 422–429.

[79] Babu, S. S., Santella, M. L., Feng, Z., Riemer, B. W., and Cohron, J. W. "Empirical model of effects of pressure and temperature on electrical contact resistance of metals". *Science and Technology of Welding and Joining*, **6,** 3, (2001), p. 126–132.

[80] Song, Q., Zhang, W., and Bay, N. "An Experimental Study Determines the Electrical Contact Resistance in Resistance Welding". *Welding Journal*, **84,** 5, (2005), p. 73–76.

[81] Vogler, M. and Sheppard, S. "Electrical Contact Resistance under High Loads and Elevated Temperatures". *Welding Journal*, **9,** 10, (1993), p. 231–238.

[82] Ciavarella, M., Greenwood, J. A., and Paggi, M. "Inclusion of “interaction” in the Greenwood and Williamson contact theory". *Wear*, **265,** 5-6, (2008), p. 729–734.

[83] Greitmann, M. J. and Roos, E. "Neues Verfahren zur Bestimmung von Übergangswiderständen an Blech-halbzeugen aus Aluminium- und Stahlwerkstoffen". *15. Fachmesse für Prüftechnik, 16.-19. Oktober 2006, Ulm,*, **15,** 1, (2006), p. 24–26.

[84] DIN EN ISO 18594: „Widerstandspunkt-, Buckel- und Rollennahtschweißen - Verfahren für das Bestimmen des Übergangswiderstands von Aluminium- und Stahlwerkstoffen (ISO 18594:2007).“, Europäisches Komitee für Normung, Deutsches Institut für Normung. 2007. Beuth Verlag, Berlin.

[85] DVS Ausschuss für Technik, Arbeitsgruppe "Widerstandsschweißen" „Merkblatt DVS 2929-1 bis 4: Messung des Übergangswiderstandes“, (2014).

[86] Monnier, A., Froidurot, B., Jarrige, C., Testé, P., and Meyer, R. "A Mechanical, Electrical, Thermal Coupled-Field Simulation of a Sphere-Plane Electrical Contact". *IEEE Transactions on Components and Packaging Technologies*, **30,** 4, (2007), p. 787–795.

[87] Rogeon, P., Carre, P., Costa, J., Sibilia, G., and Saindrenan, G. "Characterization of electrical contact conditions in spot welding assemblies". *Journal of Materials Processing Technology*, **195,** 1-3, (2008), p. 117–124.

[88] Pradille, C., Bay, F., and Mocellin, K. 2010. *An experimental study to determine electrical contact resistance*. *25th International Conference on Electrical Contacts (ICEC)*. IEEE. ISBN 1424481775.

[89] Deutsche Edelstahlwerke GmbH. 2008. *Datenblatt 1.4511 X3CrNb17*, Witten.

[90] Deutsche Edelstahlwerke GmbH. 2015. *Werkstoffdatenblatt X17CrNi16-2 1.4057*, Witten.

[91] DIN EN ISO 4287. *Geometrische Produktspezifikation (GPS) – Oberflächenbeschaffenheit: Tastschnittverfahren – Benennungen, Definitionen und Kenngrößen der Oberflächenbeschaffenheit*. Deutsches Institut für Normung. 2010. Beuth Verlag, Berlin.

[92] Ben Jemaa, N., El Abdi, R., and Carvou, E. "Numerical and experimental study of the contact resistance for high copper alloys in force domain 1–100 N". *The European Physical Journal Applied Physics*, **49,** 2, (2010), p. 22906.

[93] Zhai, C., Hanaor, D., Proust, G., and Gan, Y. "Stress-Dependent Electrical Contact Resistance at Fractal Rough Surfaces". *Journal of Engineering Mechanics*, **143,** 3, (2017), p. B4015001.

[94] Aperam Stainless Steel Europe "Product Brochure- Our stainless steel automotive structural components offer, (2013).

[95] Crinon, E. and Evans, J.T. "The effect of surface roughness, oxide film thickness and interfacial sliding on the electrical contact resistance of aluminium". *Materials Science and Engineering: A*, **242,** 1-2, (1998), p. 121–128.

[96] Galler, M., Enzinger, N., and Sommitsch, C. "The estimation of the contact interface temperature during resistance spot welding of zinc coated steels using numerical technique. Ermittlung der Kontaktoberflächen-Temperatur während des

Widerstandspunktschweißens an einem feuerverzinkten Stahl mittels numerischer Verfahren". *Materialwissenschaft und Werkstofftechnik*, **41,** 11, (2010), p. 925–930.

[97] Kamm, V. 2019. *Stability of nanopores under external pressure*. Bachelor Thesis, Universität Stuttgart.

[98] Madhusudana, C. V. 2014. *Thermal contact conductance*. Mechanical engineering series. Springer, Cham. ISBN 9783319012759.

[99] Mikic, B. B. "Thermal contact conductance; theoretical considerations". *International Journal of Heat and Mass Transfer*, **17**, (1974), p. 205–214.

[100] Cooper, M. G., Mikic, B. B., and Yovanovich, M. M. "Thermal contact conductance". *International Journal of Heat and Mass Transfer*, **12,** 3, (1969), p. 279–300.

[101] Yovanovich, M. M. "Thermal Contact Correlations". *Progress in Aeronautics and Aerodynamics*, **83**, (1982), p. 83–95.

[102] Yovanovich M. M., Culham J. R., Teertstra P. "Calculating interface resistance". *Electronics Cooling*, **3,** 2, (1997), p. 24–29.

[103] Meschde, D. 2015. *Gerthsen Physik*. Springer Verlag GmbH, Berlin, Heidelberg. ISBN 78-3-662-45977-5.

[104] Bahrami, M., Culham, J. R., Yovanovich, M. M., and Schneider, G. E. "Thermal Contact Resistance of Nonconforming Rough Surfaces, Part 2". *Journal of Thermophysics and Heat Transfer*, **18,** 2, (2004), p. 218–227.

[105] Bahrami, M., Culham, J. R., Yovanovich, M. M., and Schneider, G. E. "Thermal Contact Resistance of Nonconforming Rough Surfaces, Part 1". *Journal of Thermophysics and Heat Transfer*, **18,** 2, (2004), p. 209–217.

[106] Bahrami, M., Yovanovich, M. M., and Culham, J. R. "Thermal contact resistance at low contact pressure: Effect of elastic deformation". *International Journal of Heat and Mass Transfer,* 48, 16, (2005), p. 3284–3293.

[107] Karwa, R. 2017. *Heat and Mass Transfer*. Springer Singapore. ISBN 978-981-10-1556-4.

[108] Shi, D., Zou, F., Wang, S., Zhu, Z., and Sun, J. "Effect of surface oxidization on the spectral emissivity of steel 304 at the elevated temperature in air". *Infrared Physics & Technology*, **66**, (2014), p. 6–12.

[109] Bramson, M. A., Ed. 1968. *Infrared radiation*. *A handbook for applications : with a collection of reference tables*. Optical physics and engineering. Springer Science and Business Media, LLC, New York.

[110] Annaratone, D. 2010. *Engineering heat transfer*. Springer, Heidelberg. ISBN 9783642039324.

[111] Hahn, U. 2015. *Physik für Ingenieure*. Studium. De Gruyter Oldenbourg, Berlin. ISBN 3110376784.

[112] Shan, P., Yao, Q., Li, Y., and Luo, Z. "Reconstruction of current density distribution in weld area during resistance spot welding of aluminum alloy based on magnetic field". *Transactions of Tianjin University*, **21,** 2, (2015), p. 129–134.

[113] Xuan, W., Luo, Z., Li, Y., Wang, R., and Fan, N. 2011 "Analysis and simulation research of electromagnetic field model in resistance spot welding. In 7997. International Society for Optics and Photonics, p. 79972J.

[114] Lee, Y.-h. 2013. *Introduction to engineering electromagnetics*. Springer, Berlin, New York. ISBN 9783642361173.

[115] Choi H. S., Park I. H., Lee S. H. "Force Calculation of Magnetized Bodies in Contact Using Kelvin's Formula and Virtual Air-Gap". *IEEE Transactions on Applied Superconductivity*, **16,** 2, (2006), p. 1832–1835.

[116] Bobbio S., Delfino F., Girdinio P. and Molfino P. "Equivalent sources methods for the numerical evaluation of magnetic force with extension to nonlinear materials". *IEEE Transactions on Magnetics*, **36**, (2000), p. 663–666.

[117] Fiorillo, F. 2004. *Measurement and characterization of magnetic materials*. Elsevier series in electromagnetism. Elsevier Academic Press, Amsterdam, London. ISBN 0122572513.

[118] Mohamed, H. A. and Washburn, J. "Mechanism of Solid State Pressure Welding". *Welding Journal*, **55**, (1975), p. 302–310.

[119] Tabata, T., Masaki, S., and Azekura, K. "Bond criterion in cold pressure welding of aluminium". *Materials Science and Technology*, **5,** 4, (1989), p. 377–381.

[120] Zhang, X. P., Yang, T. H., Castagne, S., Gu, C. F., and Wang, J. T. "Proposal of bond criterion for hot roll bonding and its application". *Materials & Design*, **32,** 4, (2011), p. 2239–2245.

[121] Soltan Ali Nezhad, M. and Haerian Ardakani, A. "A study of joint quality of aluminum and low carbon steel strips by warm rolling". *Materials & Design*, **30,** 4, (2009), p. 1103–1109.

[122] Ravisankar, B., Krishnamoorthi, J., Ramakrishnan, S. S., Angelo, P. c. "Diffusion bonding of SU 263". *Journal of Materials Processing Technology*, **209**, (2009), p. 2135–2144.

[123] Islam, M. F., Ridley, N. "Isostatic Diffusion Bonding of a Microduplex Stainless Steel". *Scripta Materialia*, **38,** 8, (1998), p. 1187–1193.

[124] Guo, J. 2015 "Solid State Welding Processes in Manufacturing. In *Handbook of manufacturing engineering and technology*, A. Y. C. Nee, Ed. Springer Reference, Berlin, p. 569–592.

[125] Nai, S. M. L., Sarangapani, M., and Yeung, J. 2015 "Solid State Microjoining Processes in Manufacturing. In *Handbook of manufacturing engineering and technology*, A. Y. C. Nee, Ed. Springer Reference, Berlin, p. 641–683. DOI=10.1007/978-1-4471-4670-4_60.

[126] Derby, B. and Wallach, E. R. "Theoretical model for diffusion bonding". *Metal Science*, **16,** 1, (1982), p. 49–56.

[127] Noh, S., Kasada, R., Kimura, A. "Solid-state diffusion bonding of high-Cr ODS ferritic steel". *Acta Materialia*, **59**, (2011), p. 3196–3204.

[128] Kolukisa, S. "The effect of the welding temperature on the weldability in diffusion welding of martensitic (AISI 420) stainless steel with ductile (spheroidal graphite-nodular) cast iron". *Journal of Materials Processing Technology*, **186,** 1-3, (2007), p. 33–36.

[129] Karfoul, M. K., Tatlock, G. J., and Murray, R. T. "The behaviour of iron and aluminium during the diffusion welding of carbon steel to aluminium". *Journal of Materials Science*, **42,** 14, (2007), p. 5692–5699.

[130] Katoh, M., Nishio, K., Yamaguchi, T. "Materials evaluation of diffusion bonded steel bar and its impact characteristics". *Independent Nondestructive Testing and Evaluation International*, **35,** 4, (2002), p. 263–271.

[131] Aydin, K., Kaya, Y., Kahraman, N. "Experimental study of diffusion welding/bonding of titanium to copper". *Materials & Design*, **37**, (2012), p. 356–368.

[132] Dattoma, V., Palano, F., and Panella, F. W. "Mechanical and technological analysis of AISI 304 butt joints welded with capacitor discharge process". *Materials & Design*, **31,** 1, (2010), p. 176–184.

[133] Palano, F., Chiozzi, S., Panella, F. W., and Dattoma, V. "Characterization of Steel Welded Joints with Hybrid Projection and Capacitor Discharge Welding (CDW) Processes". *Materials and Manufacturing Processes*, **27,** 12, (2012), p. 1387–1391.

[134] Carofalo, A. P., Dattoma, V., Palano, F., and Panella, F. W. "Characterization of Aluminum Alloy Capacitor Discharge Joints Using Non Destructive and Mechanical Testing". *4th International Conference on Integrity, Reliability and Failure*, (2013).

[135] Gould, J. E., Khurana, S. P., and Li, T. "Predictions of microstructures when welding automotive advanced high-strength steels". *Welding Journal,* 85, (2006), p. 111–116.

[136] DIN EN ISO 15614-12: „Anforderung und Qualifizierung von Schweißverfahren für metallische Werkstoffe - Schweißverfahrensprüfung - Teil 12: Widerstandspunkt-, Rollennaht- und Buckelschweißen (ISO 15614-12:2014).“, Europäisches Komitee für Normung, Deutsches Institut für Normung. 2014. Beuth Verlag, Berlin.

[137] DIN EN ISO 6520-2: „Schweißen und verwandte Prozesse - Einteilung von geometrischen Unregelmäßigkeiten an metallischen Werkstoffen - Teil 2: Pressschweißungen (ISO 6520-2:2013)“, Europäisches Komitee für Normung, Deutsches Institut für Normung. 2013. Beuth Verlag, Berlin.

[138] Böckh, P. v. and Wetzel, T. 2017. *Wärmeübertragung*. *Grundlagen und Praxis*. Springer-Verlag, Berlin, Heidelberg. ISBN 978-3-662-55480-7.

[139] Buffington, F. S., Hirano, K., Cohen, M. "Self diffusion in iron". *Acta Metallurgica*, **9,** 5, (1961), p. 434–439.

[140] Bowen, A.W., Leak, G.M. "Solute diffusion in alpha- and gamma-iron". *Metallurgical Transactions*, **1,** 6, (1970), p. 1695–1700.

[141] Hirano, K., Coher, M., Averbach, B. L. "Diffusion of Nickel into Iron". *Acta Metallurgica*, **9,** 5, (1961), p. 440–445.

[142] Shewmon, P. 2016. *Diffusion in Solids*. Springer International Publishing, Cham. ISBN 978-3-319-48564-5.

[143] Arajs, S. and Colvin, R. V. "Ferromagnetic-Paramagnetic Transition in Iron". *Journal of Applied Physics*, **35,** 8, (1964), p. 2424–2426.

[144] Chen, R. Y., Yuen, W. Y. D. "Review of the High-Temperature Oxidation of Iron and Carbon Steels in Air or Oxygen". *Oxidation of Metals*, **59,** 5- 6, (2003), p. 433–468.

[145] Boggs, W. E. and Kachik, R. H. "The Oxidation of Iron-Carbon Alloys at 500°C". *Journal of the electrochemical Society*, **116,** 4, (1969), p. 424–430.

[146] Baud, J., Ferrier, A., Manenc, J., and Bérnard, J. "The oxidation and decarburizing of Fe-C alloys in air and the influence of relative humidity". *Oxidation of Metals*, **9,** 1, (1975), p. 69–97.

[147] Sachs, K. and Tuck, C. W. "Scale Growth during Re-heating Cycles". *Materials and Corrosion*, **21,** 11, (1970), p. 945–954.

[148] Abuluwefa, H., Guthrie, R. I. L., and Ajersch, F. "The effect of oxygen concentration on the oxidation of low-carbon steel in the temperature range 1000 to 1250°C". *Oxidation of Metals*, **46,** 5-6, (1996), p. 423–440.

[149] Malik, A. U. and Whittle, D. P. "Oxidation of Fe-C alloys in the temperature range 600–850°C". *Oxidation of Metals*, **16,** 5-6, (1981), p. 339–353.

[150] Meurer, H. and Schmalzried, H. "Die Entkohlung von Eisen-Kohlenstoff-Legierungen durch Zunderschichten". *Archiv für das Eisenhüttenwesen*, **42,** 2, (1971), p. 87–93.

[151] Nectoux, G. "Study of Oxidation Phenomena and of Decarburization in Steels". *Traitement Thermique*, **92**, (1975), p. 41–50.

[152] Harada, Y., Sada, Y., and Kumai, S. "Joining steel studs and steel plates by solid-state stud welding and estimation of temperature near the joint interface". *Journal of Manufacturing Processes*, **23**, (2016), p. 75–82.

[153] Pongmorakot, K., Nambu, S., Shibuta, Y., and Koseki, T. "Investigation on the mechanism of steel/steel solid-state bonding at low temperatures". *Science and Technology of Welding and Joining*, **22,** 3, (2016), p. 257–263.

[154] Nielsen, C. V., Zhang, W., Martins, P. A. F., and Bay, N. "Numerical and Experimental Analysis of Resistance Projection Welding of Square Nuts to Sheets". *Procedia Engineering*, **81**, (2014), p. 2141–2146.

[155] Woitun, D. 2017. *Gekoppelte Simulation eines Widerstandsschweißprozesses*. *Coupled simulation of a resistance welding process*. Masters Thesis, Universität Stuttgart.

[156] Wehle, M., Schmid, F., and Schmitz, G. "Bedeutung des elektrischen Kontaktwiderstandes beim KE-Einpresschweißen". *DVS Congress 2017, Düsseldorf*, (2017), p. 143–147.

[157] Wehle M., Schmid F., Schmit, G. and Greitmann M. "Experimental Study on the Role of the Electrical Contact Resistance in Resistance Projection Welding". *The 10th International Seminar & Conference on Advances in Resistance Welding*, (2018).

[158] Deutsche Edelstahlwerke GmbH. 2016. *Lieferzeugnis 1.4057 ACIDUR 4057*, Siegen.

[159] Zapp Precision Metals GmbH. 2016. *Abnahmeprüfzeugnis Edelstahl Rostfrei 1.4511*, Schwerte.

[160] Hottinger Baldwin Messtechnik GmbH. *Datenblatt Kraftaufnehmer HBM Z4 350*, Darmstadt.

[161] Olympus Life Science Europa GmbH. 2008. *Olympus LEXT OLS4000 User Manual*.

[162] Gadelmawla, E. S., Koura, M. M., Maksoud, T. M. A., Elewa, I. M., and Soliman, H. H. "Roughness parameters". *Journal of Materials Processing Technology*, **123**, (2002), p. 133–145.

Appendix

Appendix A: Materials data

Table A-1: Composition of 1.4511 (AISI 430 Nb; X3CrNb17) and 1.4057 (AISI 431; X17CrNi16-2) stainless steels in weight percent according to the delivery certificates of the manufacturers [158, 159]

Material	C	Cr	N	Mn	Ni	Nb	S	P	Fe
1.4511	0.013	17.110	0.015	0.660	-	0.23	0.002	0.017	81.953
1.4057	0.15	16.12	-	0.61	2.04	0.031	< 0.001	0.023	81.026

Table A-2: Mechanical properties of 1.4511 (AISI 430 Nb; X3CrNb17) and 1.4057 (AISI 431; X17CrNi16-2) calculated using JMatPro and modified values according to fit the room temperature data provided by the manufacturer.

		JMatPro		Modification	
Material	**Temperature [°C]**	**σy [MPa]**	**σy(T) / σy [-]**	**σy [MPa]**	**σy(T) / σy [-]**
1.4511 (AISI 430 Nb)	21	473.2	1	523	1
	200	445.2	0.94	492	0.94
	400	428.9	0.91	474	0.91
	600	305.8	0.65	338	0.65
	800	142.1	0.30	157	0.30
	1000	68.8	0.15	76	0.15
	1100	3.9	0.01	4.3	0.01
	1200	2.1	0.004	2.3	0.004
1.4057 (AISI 431)	21	984.3	1	719	1
	200	819.7	0.83	599	0.83
	400	587.1	0.60	429	0.60
	600	433.8	0.44	317	0.44
	800	266.9	0.27	195	0.27
	1000	60.2	0.06	44	0.06
	1100	17.8	0.02	13	0.02
	1200	7.6	0.01	5.6	0.01

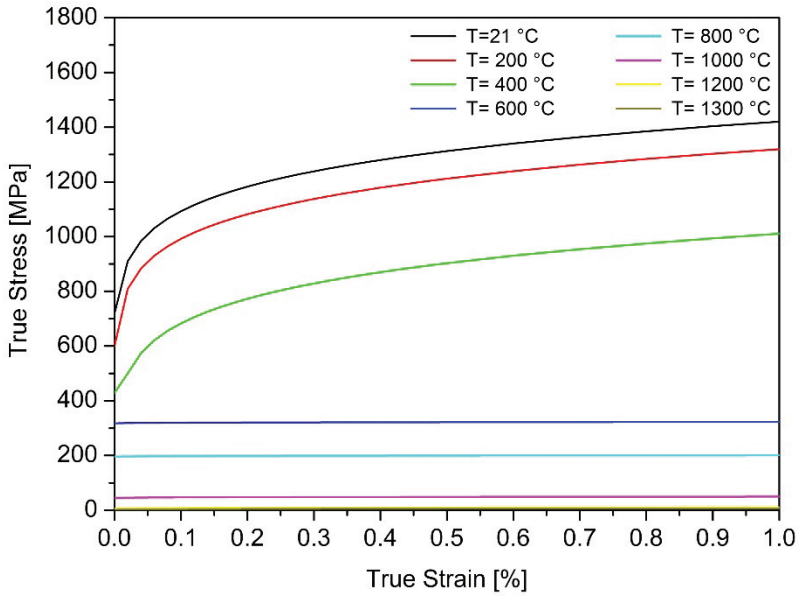

Appendix A-1: Temperature dependent stress-strain curves for 1.4057 (AISI 431) stainless steel used for FEM simulation models of chapter 3, 4 and 6.

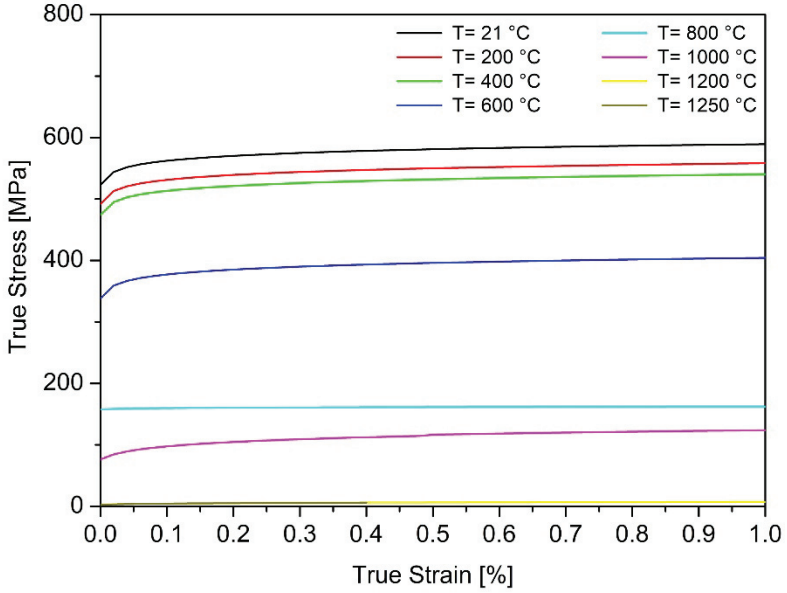

Appendix A-2: Temperature dependent stress-strain curves for 1.4511 (AISI 430 Nb) stainless steel used for FEM simulation models of chapter 3, 4 and 6.

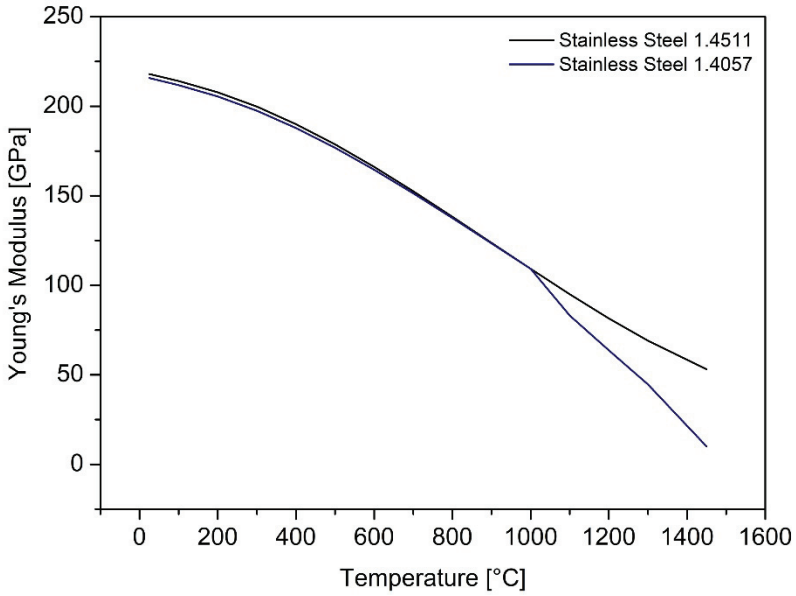

Appendix A-3: Temperature dependent Young's Modulus for 1.4511 (AISI 430 Nb) stainless steel and 1.4057 (AISI 431) stainless steel used for FEM simulation models of chapter 3, 4 and 6.

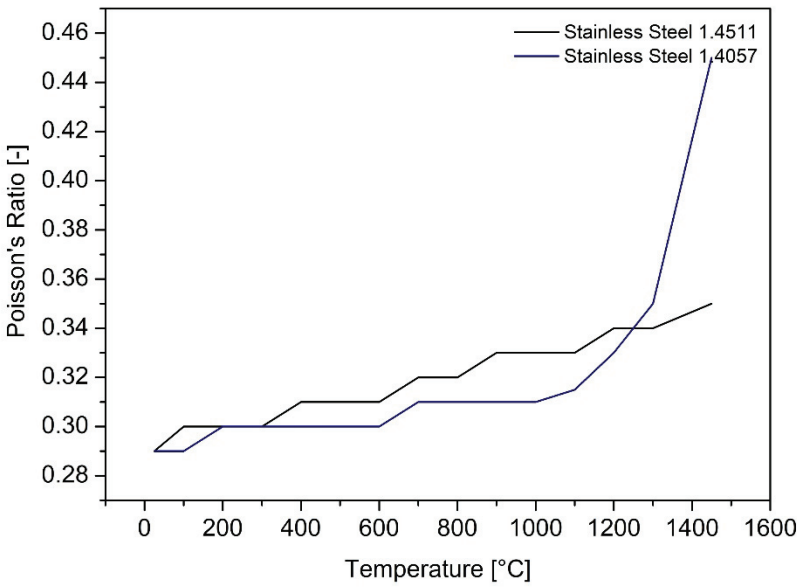

Appendix A-4: Temperature dependent Poisson's ratio for 1.4511 (AISI 430 Nb) stainless steel and 1.4057 (AISI 431) stainless steel used for FEM simulation models of chapter 3, 4 and 6.

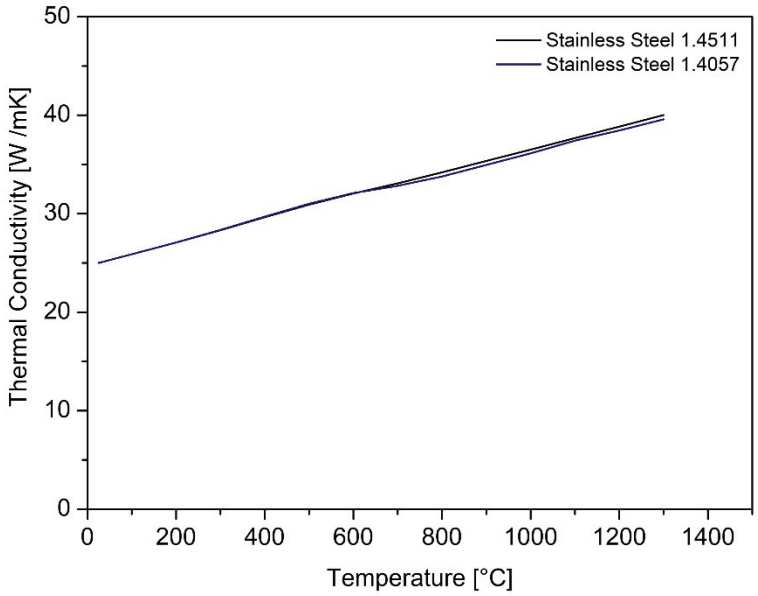

Appendix A-5: Temperature dependent thermal conductivity for 1.4511 (AISI 430 Nb) stainless steel and 1.4057 (AISI 431) stainless steel used for FEM simulation models of chapter 3, 4 and 6.

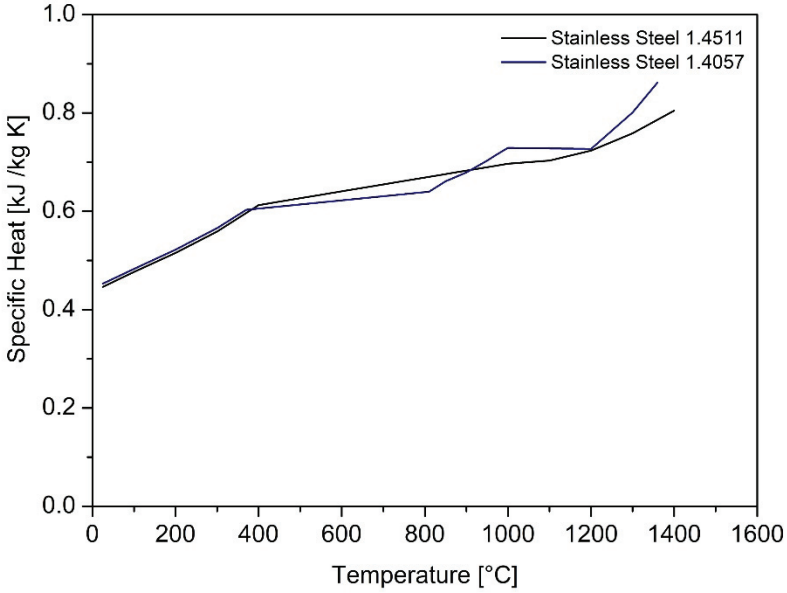

Appendix A-6: Temperature dependent specific heat for 1.4511 (AISI 430 Nb) stainless steel and 1.4057 (AISI 431) stainless steel used for FEM simulation models of chapter 3, 4 and 6.

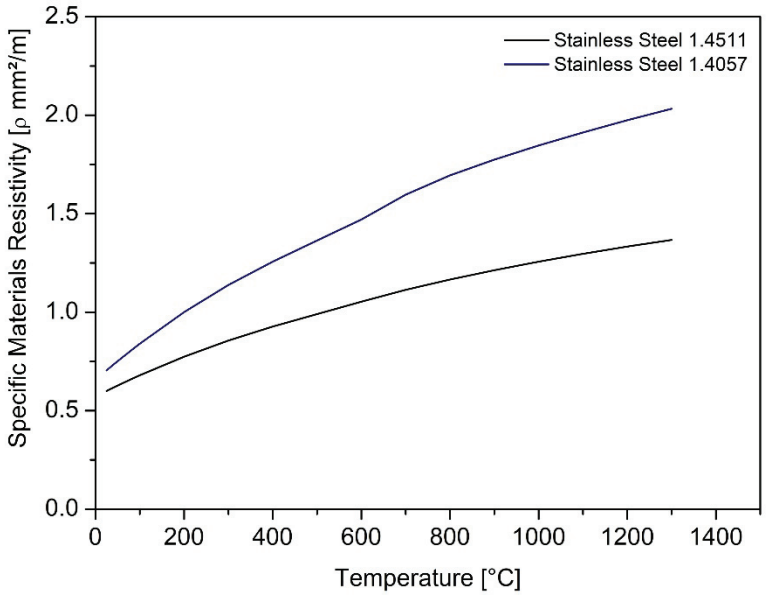

Appendix A-7: Temperature dependent electrical resistivity for 1.4511 (AISI 430 Nb) stainless steel and 1.4057 (AISI 431) stainless steel used for FEM simulation models of chapter 3, 4 and 6.

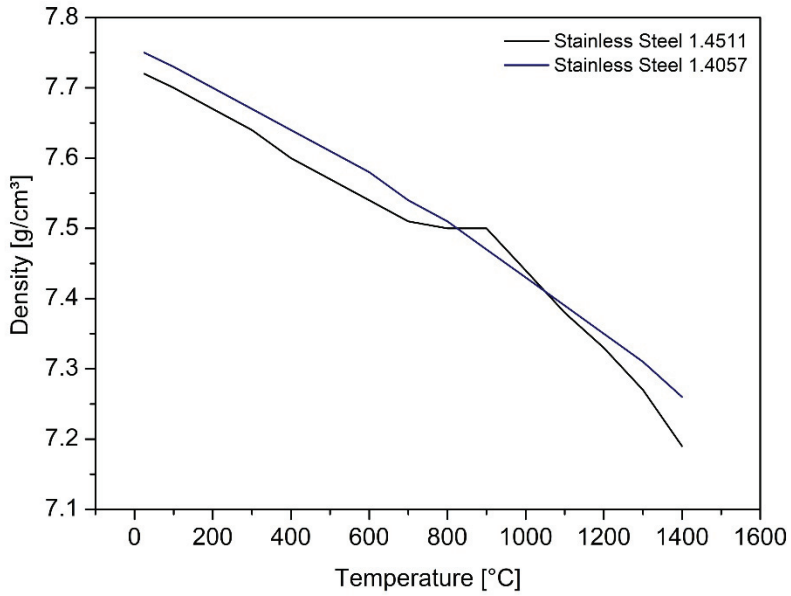

Appendix A-8: Temperature dependent density for 1.4511 (AISI 430 Nb) stainless steel and 1.4057 (AISI 431) stainless steel used for FEM simulation models of chapter 3, 4 and 6.

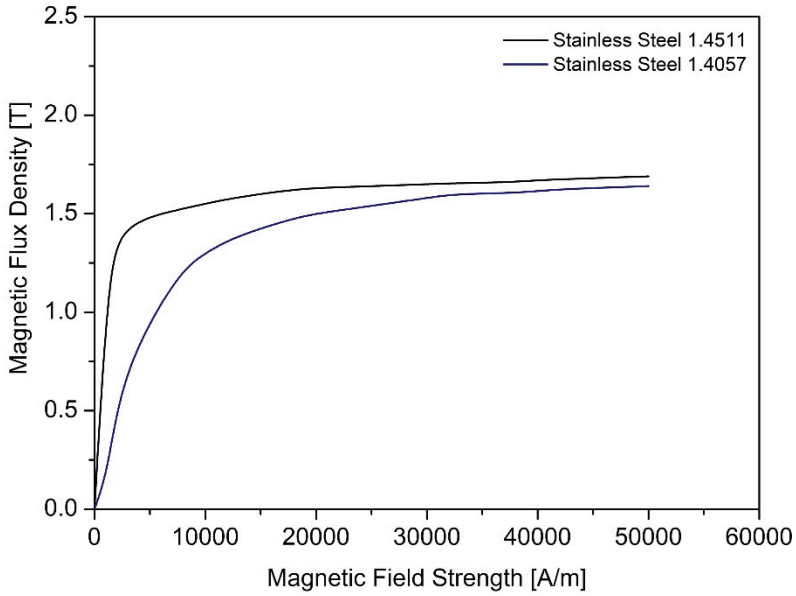

Appendix A-9: Magnetic flux density *B* as a function of magnetic field strength *H* for 1.4511 (AISI 430 Nb) stainless steel and 1.4057 (AISI 431) stainless steel used for FEM simulation models of chapter 3, 4 and 6.

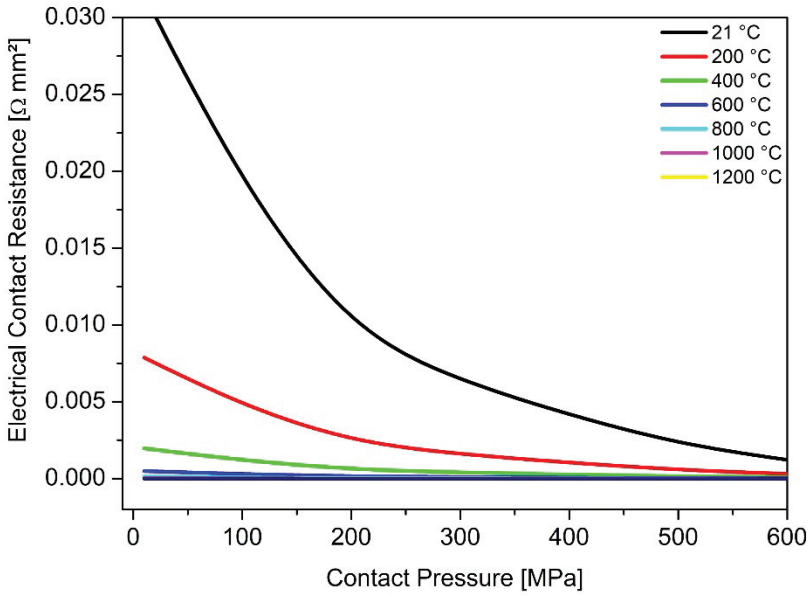

Appendix A-10: Pressure dependency of $R_{cont,el}$ for the combination of 1.4511 (AISI 430 Nb) and 1.4057 (AISI 431) stainless steel measured in chapter 3 at room temperature and extrapolated for high temperatures using the observations of Rogeon et al. [87].

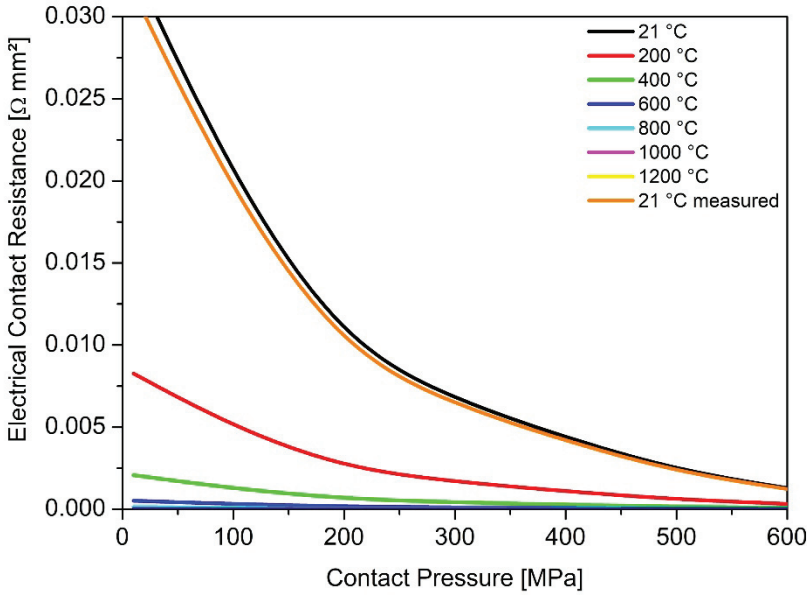

Appendix A-11: Modified pressure dependency of $R_{cont,el}$ for the combination of 1.4511 (AISI 430 Nb) and 1.4057 (AISI 431) stainless steel measured in chapter 3 at room temperature and extrapolated for high temperatures using the observations of Rogeon et al. [87]. Modification was made according to the upper error bar of the measurement.

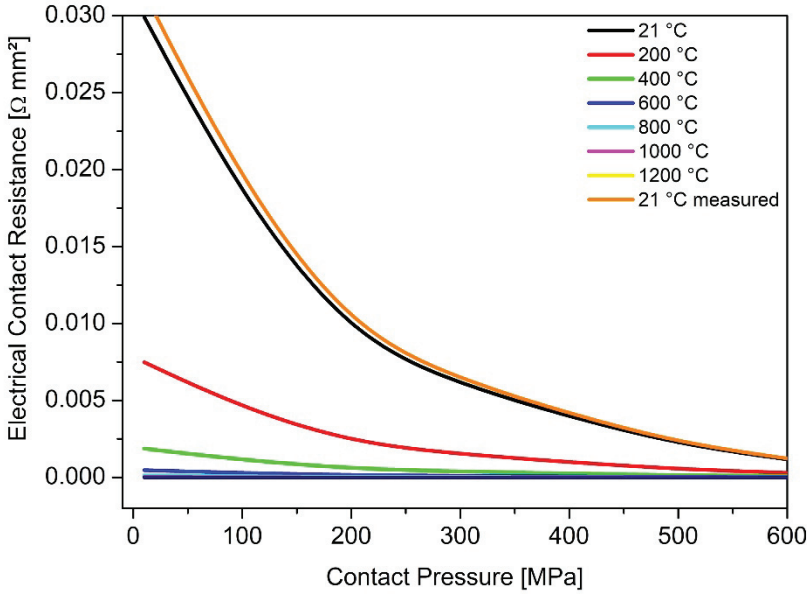

Appendix A-12: Modified pressure dependency of $R_{cont,el}$ for the combination of 1.4511 (AISI 430Nb) and 1.4057 (AISI 431) stainless steel measured in chapter 3 at room temperature and extrapolated for high temperatures using the observations of Rogeon et al. [87]. Modification was made according to the lower error bar of the measurement.

Appendix B: Error estimation

Electrical contact resistance measurements of chapter 3

Table B-1 shows the manufacturing tolerances as well as the real measured tolerances of the samples used for $R_{cont,el}$ determination.

Table B-1: Overview of the sample dimensions used for the experimental determination of $R_{cont,el}$.

Nominal values specified in the technical drawings			
	Inner diameter [mm]	Outer diameter [mm]	Contact area [mm²]
Small area	8.20 +/- 0.1	10.00 +/– 0.1	25.7 +/- 0.3
Large area	6.00 +/- 0.1	10.00 +/– 0.1	50.3 +/- 0.6
Measured values and standard deviation			
	Inner diameter [mm]	Outer diameter [mm]	Contact area [mm²]
AISI 430Nb Small area	8.21 +/- 0.01	10.04 +/- 0.01	26.23 +/- 0.02
AISI 430Nb Large area	6.01 +/- 0.01	10.05 +/- 0.01	50.87 +/- 0.06
AISI 431 Small area	8.21 +/- 0.01	10.05 +/- 0.01	26.41 +/- 0.03
AISI 431 Large area	6.01 +/- 0.02	10.05 +/- 0.01	50.94 +/- 0.06

In general the samples were manufactured more precisely than given by the tolerances in the technical drawing which enabled an even more precise determination of $R_{cont,\ el}$.

Error of apparent contact pressure

The resulting error of the apparent contact pressure, including the error of force due to the tolerances of the load cell (+/- 0.05% of the measured value [160]), was calculated for the relevant force regime between 2 kN and 50 kN. An error of +/- 12 MPa results for the apparent contact for the $R_{cont,el}$ measurements.

Error of base materials reference measurements

For R_{mat} the positioning tolerance of the measurement tips as well as the error of the measurement device (Burster 2316; +/- 0.03% of the measured value +/- 1µΩ) are considered. In the measured range of resistivities the measurement error is +/-1.01 µΩ

at maximum. For the determination of R_{mat} (see ch. 3, fig. 3-13) the root mean square of 10 values per force level was calculated. The standard deviations of these values were in the range between 0.3 µΩ and 0.9 µΩ.

For the positioning tolerance a value of +/- 0.07 mm is assumed since the marks of the measurement positions were placed using a height gauge with 2 digit accuracy (Mitutoyo series 570) and precision measurement tips (Hirschmann PRUEF 1610 FT Au) with high tip angle were used. Based on equation 3-3 the error due to positioning is < 0.1 µΩ and can be neglected. Hence, the accuracy of the total measurement is assumed to be +/- 2 µΩ, as the sum of measurement accuracy of the ohmmeter and standard deviation of the series. Figure B-2 shows the values of figure 3-13 including the error bars.

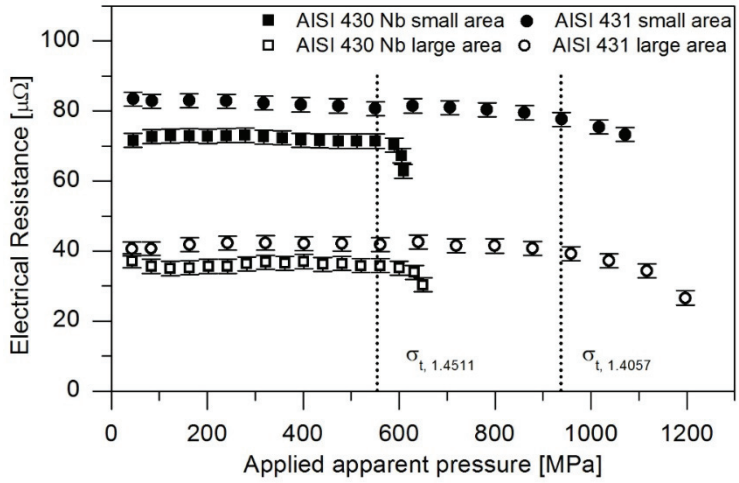

Figure B-2: Reference measurements of R_{mat} with included error bars.

Error of the electrical and thermal contact resistance values

Finally, the total error of the $R_{cont,el}$ measurements is given below (see fig. B-3). The error for the thermal contact resistances were calculated based on the error of the electrical contact resistances. These values were transformed into thermal contact resistance errors via the Wiedemann- Franz law (see fig. B-4).

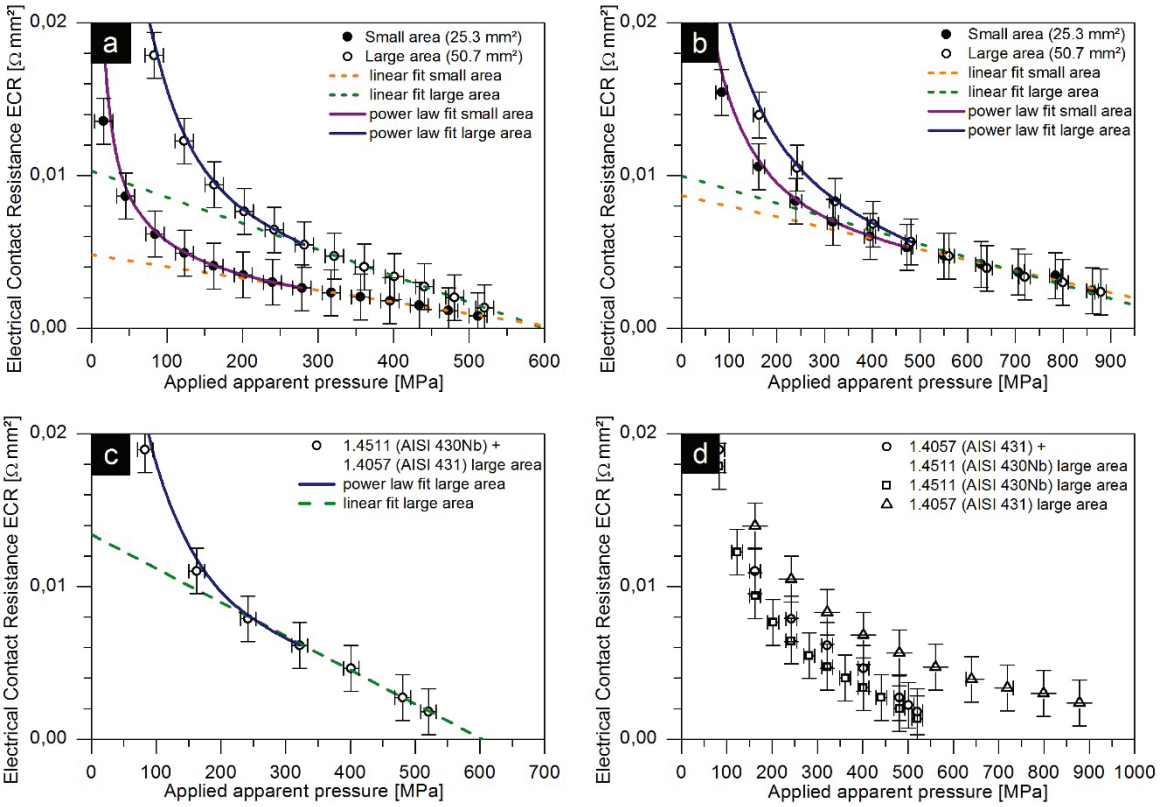

Figure B-3: Dependency of $R_{cont,el}$ for 1.4511 (AISI 431 Nb) on pressure (a), for 1.4057 (AISI 430) on pressure (b) and for the combination of both materials on pressure (c). For comparison, the measurement results for each material and combination are plotted against pressure (d). Error bars were included according to the errors estimated as described above.

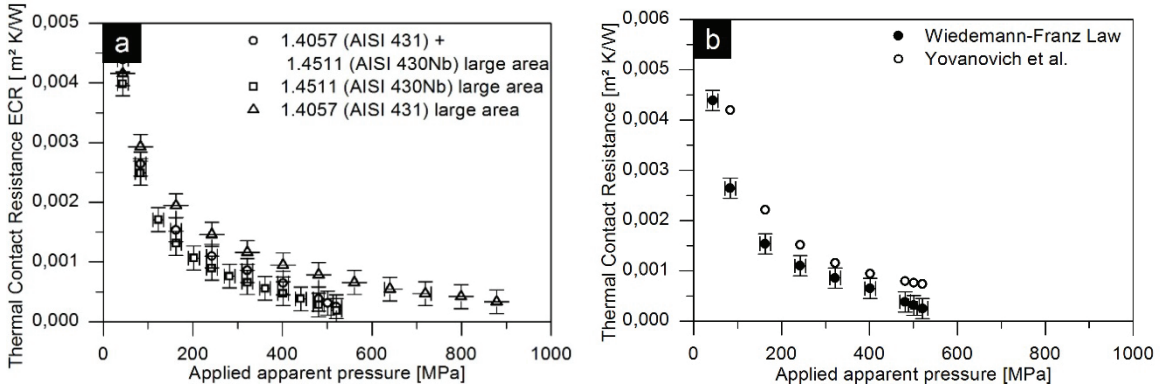

Figure B-4: Pressure dependency of the thermal contact resistance according to the *Wiedemann- Franz- Law* for 1.4057 (AISI431) and 1.4511 (AISI430Nb) stainless steel as well as for their combination, including error bars (a). Comparison of the results obtained by the calculations with Wiedemann-Franz-Law and the correlation given by *Yovanovich* et al. [102] exemplarily for the combination of 1.4511 (AISI430Nb) and 1.4057 (AISI431) stainless steel. To clarify the match with the law of *Yovanovich et al.* the error bars were also inserted into (b).

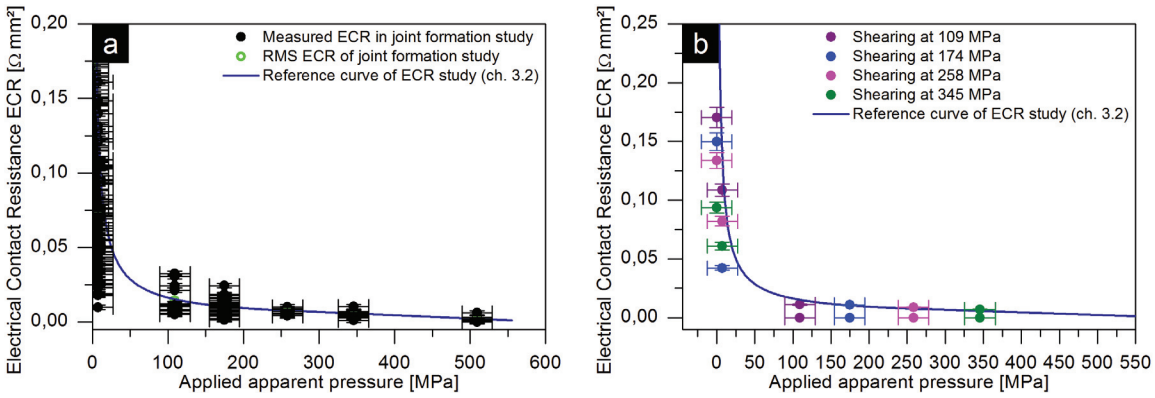

Appendix B-5: Error bars for the pressure dependent $R_{cont,el}$ values during the joint formation experiments and comparison with the results of the $R_{cont,el}$ study of chapter 3.2 (a). Influence of interfacial shearing on the $R_{cont,el}$ (b). The $R_{cont,el}$ drops suddenly when shearing is applied. This observation is repeatable for different contact pressures.

Appendix C: Definition of surface roughness parameters

The root mean square height of roughness R_q / waviness W_q is defined as

$$R_q, W_q = \sqrt{\frac{1}{l_m}\int_0^{l_m} Z^2(x)\,dx} \qquad \text{(C-1)}$$

where l_m is the measurement length and *Z(x)* is the local height in *x* with respect to the mean center line of the profile [161, 162]. An example is given below (see fig. C-1). The R_q is sensitive to large deviations from the mean center line of the profile [162]. It was therefore chosen to judge the similarity of the examined interfaces.

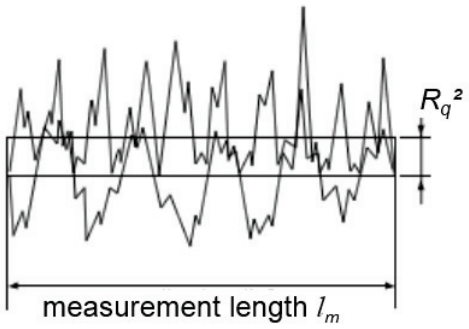

Figure C-1: Illustration of the root mean square height of roughness taken from [156]

The maximum height of roughness R_z/ waviness W_z parameter is the sum of the deepest valley R_v/ W_v and the highest peak R_p/ W_p of the profile within the measurement length. It thus is defined as

$$R_z, W_z = min\big(Z(x)\big) + max\big(Z(x)\big)\ . \qquad \text{(C-2)}$$

An illustration of the parameters is given in figure C-2.

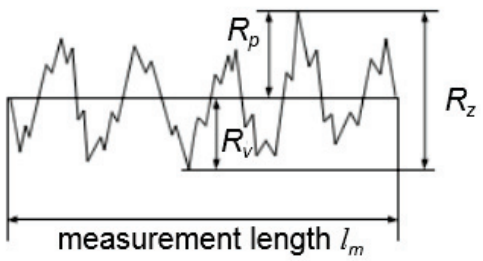

Figure C-2: Illustration of the maximum height of roughness taken from [156].

This value identifies odd peaks or valleys [162] and is sensitive to sudden imperfections of the surface. It was therefore chosen to quantify irregularities of the contact surfaces when compared to each other.

Appendix D: Theoretical derivation of the linear relation between electrical contact resistance an contact pressure

Considering the cylindrical geometry where a spherical pore is included at the interface between two completely even surfaces (see fig. D-1), the contact resistance $R_{cont,el}$ only depends on the ratio between the radius r_i of the spherical inclusion and outer radius of the cylinder R, as well as on the materials specific resistivity ρ_{el}.

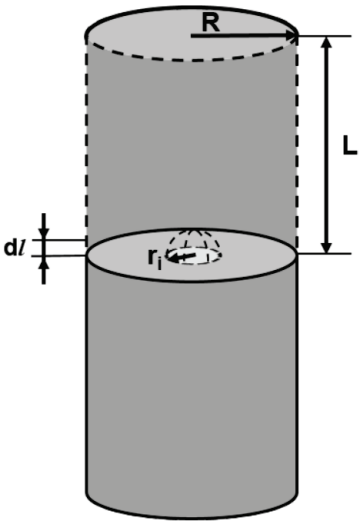

Figure D-1: Considered model geometry with pore at the interface between two solid cylindrical bodies.

The spherical pore disturbs the current flux in all a 3D volume around the sphere. However, at a given cross section at height l, the area remaining for the current to pass the interface is defined by

$$a = \pi \cdot R^2 - \pi \cdot r_i(l)^2 \tag{D-1}$$

Integration over the whole volume of the bodies starting from the interface results in the total surplus resistance caused by the spherical pore. Obviously, the volumes' materials resistance R_{mat}, needs to be subtracted from the integrated total resistance of the cylinders. Thus, the expression of the contact resistance is

$$R_{cont,el} = 2 \cdot \int_0^L \frac{\rho_{el} dl}{\pi \cdot \left(R^2 - r^2(l)\right)} - \frac{2 \cdot L \cdot \rho_{el}}{\pi \cdot R^2} \tag{D-2}$$

A spherical approach with $r^2(\omega) = r_i^2 - l^2$ gives the following expression

$$R_{cont,el} = 2 \cdot \int_0^L \frac{\rho_{el} dl}{\pi \cdot \left(R^2 - r_i^2 + l^2\right)} - \frac{2 \cdot L \cdot \rho_{el}}{\pi \cdot R^2} \tag{D-3}$$

$$= 2 \cdot \int_0^{r_i} \frac{\rho_{el} dl}{\pi \cdot \left(R^2 - r_i^2 + l^2\right)} - \frac{2 \cdot r_i \cdot \rho_{el}}{\pi \cdot R^2}$$

$$= \frac{2 \cdot \rho_{el}}{\pi} \cdot \int_0^{r_i} \frac{dl}{R^2 - r_i^2 + l^2} - \frac{2 \cdot r_i \cdot \rho_{el}}{\pi \cdot R^2}$$

$$= \frac{2 \cdot \rho_{el}}{\pi} \cdot \left[\frac{1}{\sqrt{R^2 - r_i^2}} \cdot arctan\left(\frac{r_i}{\sqrt{R^2 - r_i^2}} \right) \right] - \frac{2\rho_{el}}{\pi} \cdot \frac{r_i^2}{R^2}$$

$$\approx \frac{2 \cdot \rho_{el}}{\pi} \cdot \left[\frac{1}{R^2 - r_i^2} - \frac{r_i}{R^2} \right] - \frac{2\rho_{el}}{\pi} \cdot \frac{r_i^2}{R^2}$$

$$= \frac{2 \cdot \rho_{el}}{\pi} \cdot \left[\frac{r_i}{R^2 - r_i^2} - \frac{r_i}{R^2} \right]$$

$$= \frac{2 \cdot \rho_{el}}{\pi} \cdot \left[\frac{r_i \cdot R^2 - r_i \cdot R^2 + r_i^3}{\left(R^2 - r_i^2\right) \cdot R^2} \right] = \frac{2 \cdot \rho_{el}}{\pi} \cdot \frac{r_i^3}{\left(R^2 - r_i^2\right) \cdot R^2} \tag{D-4}$$

$$R_{cont,el} = \frac{2 \cdot \rho_{el}}{\pi} \cdot \frac{r_i^3}{R^4} \qquad \left[R_{cont,el}\right] = \Omega \tag{D-5}$$

For multiple, equally sized and homogeneously distributed spherical pores at the interface, the total electrical contact resistance is

$$\frac{1}{R_{cont,el}^{tot}} = N \cdot \frac{1}{R_{cont,el}} \tag{D-6}$$

in which the number *N* is related to the distance 2 *R*

$$N = \frac{A}{\pi \cdot R^2} \tag{D-7}$$

Thus the final expression is

$$R_{cont,el} = \frac{2 \cdot \rho_{el} \cdot r_i^3}{A \cdot R^2}. \tag{D-8}$$